OUKA
Osaka University Knowledge Archive

Title	Enhancement of dilepton production rates and associated transport coefficients due to phase transitions in dense QCD
Author(s)	西村, 透
Citation	大阪大学, 2024, 博士論文
Version Type	VoR
URL	https://doi.org/10.18910/96387
rights	
Note	

Osaka University Knowledge Archive : OUKA

https://ir.library.osaka-u.ac.jp/

Osaka University

OSAKA UNIVERSITY

DOCTORAL THESIS

Enhancement of dilepton production rates and associated transport coefficients due to phase transitions in dense QCD

Author:
Toru NISHIMURA

Supervisor:
Professor Masayuki ASAKAWA

A thesis submitted in fulfillment of the requirements for the degree of Doctor of Philosophy

in the

Nuclear Theory Group
Department of Physics

February 29, 2024

OSAKA UNIVERSITY

Abstract

School of Science
Department of Physics

Doctor of Philosophy

Enhancement of dilepton production rates and associated transport coefficients due to phase transitions in dense QCD

by Toru NISHIMURA

Revealing the rich phase structure and developing a condensed matter physics of Quantum Chromodynamics in the high-density region is one of the main subjects in current nuclear physics, and great efforts have been made both theoretically and experimentally. In the high-density region, the first-order chiral transition line(s) with the QCD critical point(s) (QCD-CP) is expected to exist based on theoretical works. Moreover, in the more dense region, the color superconducting (CSC) phase realized by the Cooper instability of quarks has also been predicted. One of the main purposes of the beam-energy scan program in the relativistic heavy-ion collisions (HIC) at RHIC, HADES, and NA61/SHINE is the search for these phase transitions. Further studies with higher statistics will be pursued in future experiments planned at GSI-FAIR, NICA-MPD, and J-PARC-HI. In this current experimental context, it is of great value to consider theoretically how to observe such phase structures in HIC.

To discuss the observability of the CSC phase and the QCD-CP in HIC, we investigate how the soft modes due to the phase transitions to the CSC (CSC-PT) and the QCD-CP affect the dilepton production rate (DPR) based on the two-flavor NJL model. The soft modes are low-energy collective excitation modes formed by amplitude fluctuations of the order parameter, which are known to develop significantly near the phase transition to 2-flavor CSC (2SC-PT) and the QCD-CP. The medium effect on the DPR is dictated by that of the photon self-energy. The effects of the soft modes on the self-energy are taken into account by the Aslamazov-Larkin (AL), Maki-Thompson (MT), and density of states (DOS) terms. Since the set of these terms satisfies the Ward identity of the photon self-energy, we can respect the charge conservation law in our formalism.

Our numerical results show that the DPR is significantly enhanced at low invariant-mass region $m_{ll} \lesssim 200$MeV near the 2SC-PT and QCD-CP, reflecting the critical enhancement of the respective soft modes. We argue that an experimental exploration of the possible enhancement of the DPR in the ultra-low-mass region is quite worthwhile to do because these enhancements of DPR could be signals to confirm the existence of the 2SC phase and QCD-CP. Furthermore, we calculate the associated transport coefficients, electric conductivity and relaxation time, which are related to the low energy/momentum behavior of DPR. We show that the coefficients diverge at the 2SC-PT and QCD-CP by the respective soft modes and that their critical exponents are different at the respective phase transitions owing to the difference in properties of the 2SC-PT and QCD-CP soft modes.

Acknowledgements

First of all, I wish to sincerely express my gratitude to my supervisor Professor Masayuki Asakawa. His advice, comments, and support have been invaluable to me during my Ph.D. study. I am deeply grateful to Professor Masakiyo Kitazawa for his enthusiastic guidance and persistent help throughout my Ph.D. course. I also would like to thank Professor Teiji Kunihiro for his collaboration and a lot of his beneficial discussions. I further express my gratitude to Professor Yasushi Nara and Professor Jan Steinheimer for their kind hospitality, helpful discussions and collaboration at the Frankfurt Institute for Advanced Studies and the Akita International University.

The members of the Nuclear Theory Group in Osaka University have supported my research throughout my Ph.D. course. I would like to thank Professor Yukinao Akamatsu for fruitful discussions and his constructive comments. I also thank all my colleagues in the Nuclear Theory Group for their friendships and fruitful communications. I would also like to thank the members of the Nuclear Theory Group in Kyoto University for their help and support during most of the second half of my Ph.D. studies.

Finally, I would like to express my deepest gratitude to my family and friends for their continuous support during my whole life. Without their encouragement, I could not have completed my Ph.D. course.

Contents

Abstract iii

Acknowledgements v

1 Introduction 1
- 1.1 Quantum chromodynamics . . . 1
- 1.2 Phase structure in QCD . . . 3
- 1.3 Investigations of dense QCD in heavy-ion collision experiments . . . 6
  - 1.3.1 Dilepton productions in HIC . . . 6
  - 1.3.2 Experimental data of DPR . . . 7
  - 1.3.3 Theoretical aspects of Dilepton production rates . . . 9
    - Dilepton production rates . . . 9
    - Associated transport coefficients . . . 10
- 1.4 Purpose and Organization . . . 11

2 Phenomenology of Critical Fluctuations 13
- 2.1 Ginzburg-Landau theory . . . 13
  - 2.1.1 Homogeneous system . . . 13
  - 2.1.2 Inhomogeneous system . . . 15
- 2.2 Time-dependent Ginzburg-Landau equation . . . 16
- 2.3 Fluctuations near the QCD-CP . . . 17

3 Finite temperature and density quantum field theory 21
- 3.1 Imaginary-time formalism . . . 21
- 3.2 Linear response theory . . . 23

4 Nambu–Jona–Lasinio model 27
- 4.1 Thermodynamic potential in the MFA . . . 27
- 4.2 Phase diagram . . . 31

5 Soft modes 33
- 5.1 Random-phase approximation . . . 34
- 5.2 Thouless criterion . . . 37
- 5.3 Effective theory of the soft modes . . . 39
  - 5.3.1 2SC-PT soft mode . . . 39
  - 5.3.2 QCD-CP soft mode . . . 42

6 Modifications of photon self-energy due to the soft modes 45
- 6.1 Contribution of free quark gases . . . 45
- 6.2 Case of 2SC-PT soft mode . . . 46
  - 6.2.1 Construction scheme . . . 46
  - 6.2.2 Approximation to vertices . . . 48
  - 6.2.3 Explicit form of AL term . . . 50
- 6.3 Case of QCD-CP soft mode . . . 51
  - 6.3.1 Construction scheme . . . 51

6.3.2 Approximation to vertices . . . 53
6.3.3 Explicit form of AL term . . . 54

7 Transport coefficients **57**
7.1 Analytical results . . . 58
7.2 Numerical results . . . 60

8 Dilepton production rate (DPR) **65**
8.1 Explicit form of $g_{\mu\nu}\Pi^{R\mu\nu}(k)$ . . . 65
8.1.1 Contribution from the soft modes . . . 65
8.1.2 Contribution of free quark gases . . . 67
8.2 Energy spectra . . . 67
8.3 Invariant-mass spectra . . . 70

9 Summary **73**

A Three-momentum cutoff scheme **75**

B Expansion coefficients of soft modes **79**
B.1 Coefficients of the 2SC-PT soft mode . . . 79
B.1.1 LE approximation . . . 79
B.1.2 TDGL approximation . . . 80
B.2 Coefficients of the QCD-CP soft mode . . . 82
B.2.1 LE approximation . . . 82
B.2.2 TDGL approximation . . . 83

C Derivatives of the spectral densities **85**
C.1 Exponents as for the 2SC-PT . . . 87
C.2 Case of the QCD-CP . . . 87

D Dilepton yields along the isentropic lines **89**

Chapter 1

Introduction

In these decades, the study of high temperature and density matter in the quantum chromodynamic (QCD) has been stimulated by advances in theory, experiment, and numerical simulation. It has been predicted that the strongly interacting many-body system has a rich phase structure. At extremely hot and/or dense matter, quarks are expected to be liberated from hadrons and the system undergoes the phase transition to the quark-gluon plasma (QGP) phase. The search for such an ultimate state has been carried out in heavy-ion collision experiments, and these experiments have ensured the existence of QGP.

Theoretical studies have predicted the existence of first-order phase transitions and their endpoint, the QCD critical point, triggered by the chiral symmetry in the high-density region, and the color superconducting phases at higher densities. On the other hand, recent advances in experimental techniques and vigorous efforts by experimentalists are making it possible to conduct heavy-ion collision (HIC) experiments that can search for such a high-density QCD matter. In this sense, the study of high-density QCD phase structures is one of the main subjects in current nuclear physics [1, 2].

1.1 Quantum chromodynamics

The quantum chromodynamics (QCD) is the fundamental theory that describes the dynamics of strong interaction between quarks and gluons. Quarks are spin-1/2 fermions with fractional electric charges, and have the flavor degree of freedom: up (u), down (d), strange (s), charm (c), bottom (b), and top (t). They carry the baryon number $Q_B = +1/3$ and form hadrons such as the proton, neutron, and pion. Moreover, to make up hadrons without violating the Pauli exclusion principle, the quarks have a new quantum number called 'color': red (R), blue (B), and green (G). On the other hand, the gluons mediating the strong interactions between quarks are massless spin-1 gauge bosons. They also carry a color charge and interact with themselves, which is a remarkable feature that the quantum electrodynamics (QED) does not have. Table 1.1 shows the quantum numbers carried by quarks and gluons. The study of QCD plays a significant role in understanding the nature of quarks, gluons, and hadrons.

QCD is described by a non-Abelian gauge theory with the symmetry group SU(3). The Lagrangian density of QCD is given by

$$\mathcal{L}_{\mathrm{QCD}} = \bar{\psi}(i\gamma^\mu D_\mu - m)\psi - \frac{1}{4}F^a_{\mu\nu}F^{\mu\nu}_a. \tag{1.1}$$

where ψ ($\bar{\psi} = \psi^\dagger\gamma^0$) represents the quark (anti-quark) Dirac field with the current quark mass m. In this Thesis, γ^μ denotes the gamma matrix that satisfies the anticommutation relation $\{\gamma^\mu, \gamma^\nu\} = 2g^{\mu\nu}$. Also, we employ the metric $g^{\mu\nu} = (+,-,-,-)$.

The quark field ψ belongs to the fundamental representation of $SU_c(3)$ and forms the color triplet. In Eq. (1.1), the covariant derivative $D_\mu = \partial_\mu + igt_aA^a_\mu$ with the gauge field A^a_μ acts on the quark field, where g is the coupling constant of strong interaction, t_a is the fundamental representation of $SU_c(3)$ Lie algebra satisfying the commutation relations $[t_a, t_b] = if_{abc}t_c$ with the structure

	Symbol	Charge	J^P
up	u	$+2/3$	$(1/2)^+$
down	d	$-1/3$	$(1/2)^+$
charm	c	$+2/3$	$(1/2)^+$
strange	s	$-1/3$	$(1/2)^+$
top	t	$+2/3$	$(1/2)^+$
bottom	b	$-1/3$	$(1/2)^+$
gluon	g	0	1^-

TABLE 1.1: Electric charge, spin, and parity of quarks and gluon

constants f^{abc}. The subscript $a = 1, 2, \cdots, 8$ denotes color octet in the adjoint representation of the $SU_c(3)$. The field strength of the gauge field is given by $F_a^{\mu\nu} = \partial^\mu A_a^\nu - \partial^\nu A_a^\mu - g f_a{}^{bc} A_b^\mu A_c^\nu$, whose last term leads to the gluon self-interaction.

Asymptotic freedom and Confinement

There are some curious and notable features in QCD. One of them is asymptotic freedom [3, 4], which is confirmed experimentally through the electron-proton deep inelastic scattering [5]. The asymptotic freedom is the phenomenon that the coupling constant $\alpha_s(Q^2)$ with the renormalization scale Q becomes small at short distances or large Q. This running coupling is given by the renormalization group equation up to the one-loop order of gluon self-energy as follows

$$\alpha_s(Q^2) = \frac{g(Q^2)}{4\pi} = \frac{1}{4\pi b_0 \log(Q^2/\Lambda^2_{\rm QCD})}, \tag{1.2}$$

where $b_0 = (11N_c - 2N_f)/48\pi^2$. Since the number of colors and flavors are $N_c = 3$ and $N_f = 6$, respectively, b_0 is positive in QCD. The renormalization point $\Lambda_{\rm QCD} \simeq$ 200–300MeV is determined experimentally, which is the typical energy scale of QCD. From Eq. (1.2), it is found that $\alpha_s(Q^2) \to 0$ as $Q^2 \to \infty$, which implies that the interaction between quarks and gluons becomes weaker at high energies or short distances. This is why QCD is said to have asymptotic degrees of freedom.

Another important feature of QCD is the color confinement [6]. From Eq. (1.2), it is also found that $\alpha_s(Q^2) \to \infty$ as $Q^2 \to 0$, which implies that the interaction between quarks and gluons becomes stronger at low energies or long distances. Thereby, quarks and gluons are bound in color-singlet hadrons, and they cannot be observed as a one-particle state. In fact, no experiments have observed color-charged particles or fractional charges as shown in Table 1.1.

Chiral symmetry

Owing to the asymptotic freedom of QCD, the perturbative treatment is justified when physical processes with large momentum transfers are considered. In other words, phenomena at low energy become non-perturbative. The spontaneous chiral symmetry breaking in QCD is one of the non-perturbative phenomena.

Now, we consider the left- and right-handed quarks

$$\psi_L = \frac{1-\gamma_5}{2}\psi, \quad \psi_R = \frac{1+\gamma_5}{2}\psi, \tag{1.3}$$

with $\gamma_5 = i\gamma^0\gamma^1\gamma^2\gamma^3$. In the chiral limit $m = 0$, the QCD Lagrangian has the chiral symmetry under the global $SU(N_f)_L \times SU(N_f)_R$ transformation

$$\psi_L \to e^{-\theta_L^a t_a}\psi_L, \quad \psi_R \to e^{-\theta_R^a t_a}\psi_R, \tag{1.4}$$

where θ_L^a and θ_R^a are space-time independent parameter. Nevertheless, in the QCD vacuum, this symmetry is spontaneously broken as follows

$$SU(N_f)_L \times SU(N_f)_R \to SU(N_f)_V. \tag{1.5}$$

This symmetry breaking was proposed by Nambu and Jona-Lasinio [7, 8]. This origin is the finite chiral condensate $\sigma = \langle\bar{\psi}\psi\rangle$, which corresponds to the Copper pair in superconductivity. The chiral condensate is an order parameter of the chiral symmetry in the QCD. When a symmetry is broken spontaneously, there is a massless mode called Nambu-Goldstone (NG) bosons, such as pions, which are the pseudoscalar mesons.

On the other hand, in the real world, the chiral symmetry is explicitly broken since quarks have nonzero masses. However, the masses of u and d quarks are quite smaller than $\Lambda_{\rm QCD}$, and then it can be regarded that the chiral symmetry is approximately satisfied. This small explicit breaking leads to the massive NG bosons. For example, the pion mass in the real world is much lighter than other mesons.

1.2 Phase structure in QCD

The asymptotic freedom implies that the release of quarks and gluons from hadrons occurs with increasing temperature T and/or baryon number density n_B [9, 10]. The plasma state of deconfined quarks and gluons is referred to as the quark-gluon plasma (QGP). The temperature of the phase transition to QGP is expected to be on the same order as the QCD scale, approximately $T_c \simeq \Lambda_{\rm QCD} \simeq 10^{12}$ K. Recent calculations in lattice QCD Monte Carlo simulation, a first-principle non-perturbative approach to QCD, indicate that the transition temperature (pseudo-critical temperature) is $T_c \simeq 157$ MeV when the baryon chemical potential μ_B is zero, e.g. the Wuppertal-Budapest Collabollration [11] and the HotQCD Collaboration [12].

On the other hand, for the finite μ_B region, validated numerical lattice QCD methods have not yet been established and the reliable results have not been obtained. Therefore, nobody accurately understands the QCD phase diagram in dense regions. However, analysis with the effective model of QCD has pointed out the possibility of rich phase structure. For example, it has been predicted that the crossover transition to QGP at $\mu_B = 0$ turns into a first-order phase transition in the high-density region [13, 14, 15, 16, 17]. Its critical density may exist around $n_B \simeq (1/\Lambda_{\rm QCD})^3 \simeq 1$ fm^{-3}, which is several times greater than the density of normal nuclear matter $n_0 \simeq 0.16$ fm^{-3}. In the real world, such extreme states can be encountered at the centers of compact stars. In the following, we describe other interesting possibilities: the QCD critical point and color superconductivity.

QCD critical point

As described above, lattice QCD calculations have revealed that the phase transition to the deconfined phase is a smooth crossover at $\mu_B = 0$, while calculations by various effective models have predicted that the first-order phase transition associated with the chiral symmetry breaking exists at finite μ_B. Then, if the first-order phase transition exists in the high-density region, this transition line possesses at least one endpoint and connects to the crossover transition line at the point. This endpoint is called the QCD critical point (QCD-CP) and the order of its phase transition is second order.

When a system is close to a second-order phase transition, critical phenomena often occur there, such as the divergence of fluctuations in the order parameter field. It is originated from the softening of the hydrodynamic slow variables whose excitation energies vanish in the long wavelength limit since effective potential becomes near the transition. The thermodynamic singularities are characterized by the static universality class. Even if systems are completely different, the systems that belong to the same universality class show similar singular behavior. It is known that the classification of the universality class is determined only by the spatial dimension of the system, the symmetry of order parameter, and the range of the interaction [18]. For instance, in the case of massless two-flavor QCD, the chiral symmetric and broken phases are divided by first-order and second-order phase transition lines because of the exact chiral symmetry, $O(4) \sim SU(2) \times SU(2)$. In this case, the chiral condensate is the exact order parameter and therefore its fluctuation diverges near the second-order phase transition. This second-order phase transition belongs to the same universality class as the $O(4)$ ferromagnetic model [19]. The point at which the order of the phase transition changes from first to second is called the tri-critical point.

On the other hand, in the case of the massive two-flavor QCD, the critical point is the QCD-CP, which belongs to the same universality class as the three-dimensional Z_2 Ising model [19]. Near the QCD-CP, it is known that a mixing between the chiral condensate σ and the net-baryon number density n_B is allowed owing to the finite quark masses [20, 21, 22]. As a result, the linear coupling between the fluctuations of σ and n_B is only a hydrodynamic slow variable and its fluctuation diverges at the QCD-CP. In this Thesis, the collective mode formed by the fluctuation is called the "QCD-CP soft mode". The enhancement of the soft mode near the QCD-CP causes singularities of transport coefficients, e.g. coherence length, relaxation time, and so on. Such dynamical critical phenomena are characterized by the dynamical universality class. In general, the dynamical universality depends on the set of slow variables. Because of the coupling of σ and n_B, it is known that the dynamical universality class of the QCD-CP is the same as that of in the liquid gas phase transition, which belongs to the model H [23].

If the dense matter created by HIC approaches the QCD-CP, such critical phenomena could affect significantly the observables in the experiments. Many proposals have been made for observational identification of the QCD CP in the HIC experiments, such as the event-by-event fluctuations of conserved charges and especially their non-Gaussianity, large fluctuations of the low-momentum particle distributions, anomalous fluid dynamical phenomena with diverging transport coefficients and so on [24, 25, 26, 27, 28, 29, 30]. As described in the next section, active experimental analyses of the dense matter are ongoing at the beam-energy scan program at RHIC, NA61/SHINE, and HADES. Moreover, the future experiments at FAIR and J-PARC-HI will further pursue them. In this Thesis, we will reconsider the experimental observability of the QCD-CP by investigating the effect of the soft mode on observables in HIC.

Color superconductivity

At low temperature and the higher density region, the existence of color superconductivity (CSC) has been predicted [31]. As explained earlier, the quark matter at high density can be approximately treated as the system of free fermions because of the asymptotic freedom . At sufficiently low temperatures, the attractive force between quarks necessarily gives rise to the Cooper instability, which leads to phase transitions to the superconducting phases. At asymptotically high densities, the one-gluon exchange (OGE) interaction can be employed. With a simple algebra, it is found that the color antitriplet channel of the OGE interaction is attractive. Therefore, the attraction in this channel causes the Cooper instability. At moderate density where the interaction is not weak enough to employ the OGE, it is also believed that the color antitriplet channel gives rise to the instability because several attempts to determine the coupling constants of the quark-quark interaction give the strong attraction in the antitriplet channel again [32, 33].

The studies of the CSC phase started around 1980. Nevertheless, less attention has been paid to this physics until about 2000, because the predicted gap energy in Ref. [34] was discouragingly

small. Properties of the CSC are reconsidered by several authors with the low energy effective model of QCD, and it was found that the diquark gap can become about 50–100 MeV at moderate quark chemical potential $\mu \simeq 400$ MeV [35, 36, 37]. The analysis in the weak coupling regime was also reexamined with the dynamically screened color-magnetic interaction [38]. It was found that the long-range nature of the magnetic interaction leads to a nonstandard gauge coupling G dependence of the gap $\Delta \sim exp(-3\pi^2/G)$, which also brings a larger Δ at low density. These works have stimulated intensive studies of the CSC, which in turn reveals the rich physics of the CSC.

There are various patterns of symmetry breaking in the CSC. The two-flavor superconductor (2SC) is one of the possible pairing patterns, which has been considered in the classical work Ref. [34]. In this pattern, the color and flavor structure of the condensate is

$$\Delta_{ij}^{\alpha\beta} = \langle (\psi^T)_i^\alpha C i\gamma_5 \psi_j^\beta \rangle \sim \epsilon_{ij}\epsilon^{\alpha\beta 3} \tag{1.6}$$

with α, β (i, j) being the color (flavor) indices. The pairing is induced by the color antitriplet channel, and then the flavor matrix becomes also antisymmetric because of the Pauli principle. In the 2SC phase, the $SU(3)_c$ color gauge symmetry is broken down to the $SU(2)_c$. The 2SC pairing is expected to be realized in the lower density region where the strange quark degrees of freedom can be neglected. On the other hand, at a sufficiently high density that the strange quark mass cannot be neglected, the ground state becomes the color-flavor locking (CFL) phase, whose pairing pattern is

$$\Delta_{ij}^{\alpha\beta} = \langle (\psi^T)_i^\alpha C i\gamma_5 \psi_j^\beta \rangle \sim \sum_{I=1,2,3} \epsilon_{ijI}\epsilon^{\alpha\beta I}. \tag{1.7}$$

In this pairing, the color and flavor indices are again antisymmetric, while the symmetry breaking pattern is quite different from the 2SC. In the CFL phase, the condensate remains invariant under the simultaneous flavor and color transformations. The color-flavor orientations of the condensates are locked to each other, and the color-flavor symmetry $SU(3)_c \times SU(3)_L \times SU(3)_R$ is broken down to $SU(3)_{c+L+R}$.

As described later, HIC experiments to explore the phase structure in the dense QCD are ongoing and future experiments are designed so as to enable more detailed analyses. Then, it would be interesting to search for the possible existence of the CSC phases in these experiments. The exploration of the CSC in the HIC, however, is quite a challenge because the temperatures achieved in the HIC can become as high as 100 MeV at the highest baryon density [39], which may be much higher than the critical temperature T_c of the CSC. It is therefore unlikely that the CSC phase will be observed in the HIC.

Nevertheless, the matter created in the HIC may be within the critical region of the 2SC above its critical temperature T_c where the diquark-pair fluctuations are significant, and thus precursory phenomena of the 2SC [40, 41, 42] do manifest themselves through appropriate observables by the HIC. In metallic superconductivity, it is known that fluctuations of Cooper pairs of electrons cause an anomalous enhancement of the electric conductivity above the critical temperature [43, 44, 45]. Since the quark matter in the relevant density region is a strongly coupled system [46], the CSC can have a wider critical region where the precursory phenomena are pronounced. In fact, it has been already shown that the diquark fluctuations develop a well-defined collective mode near but above the phase transition to the 2SC (2SC-PT), and its collectivity and the softening nature affect various observables including the appearance of the region in a rather wide range of temperatures [40, 41, 42, 47, 48]. In this Thesis, this collective mode developing owing the 2SC-PT is called the "2SC-PT soft mode". We will investigate the effect of the 2SC-PT soft mode on the observables in HIC as well as the QCD-CP.

1.3 Investigations of dense QCD in heavy-ion collision experiments

The ultra-relativistic heavy-ion collision (HIC) is one of the ways to explore the rich phase structure of QCD described in the previous section, where two heavy nuclei such as gold or lead are accelerated by ring-type accelerators and collided with each other. The ultra-relativistic HIC experiment is a unique method to produce matter under extreme conditions in temperature and density on the Earth [49]. The experiments for such a matter using HIC began in the 1980s and have been conducted with increasing collision energies to the present day at accelerator facilities around the world, such as the Large Hadron Collider (LHC) at CERN, the Relativistic Heavy Ion Collider (RHIC) at BNL, and the Schwer-Ionen-Synchrotron (SIS) at GSI. Also, future experiments are planned at the Facility for Antiproton and Ion Research (FAIR), the Nuclotron-based Ion Collider fAcility (NICA), the High Intensity heavy ion Accelerator Facility (HIAF), and the heavy-ion program at the Japan Proton Accelerator Complex (J-PARC).

However, an extreme matter created by such experiments has a very short lifetime of order $10\text{fm}/c$ and it soon cools down to a hadronic medium. Therefore, direct observation of the properties of the quark matter or phase transitions is impossible, and multilateral analyses are required to investigate them. Nevertheless, in RHIC, through measurements of various observables, such as the collective flow, the J/Ψ suppression, and so on, the generation of QGP was concluded as a consistent interpretation of these phenomena [50, 51].

An important feature of these experiments is that the temperature and density of the produced matter can be controlled to some extent by changing the incident energy $\sqrt{s_{NN}}$ and the species of colliding ion. The physical mechanism of this variation is understood as follows. Firstly, in high-energy collisions, quarks inside the incident nucleons almost pass through the collision point since the nucleon-nucleon interactions are small and there is not enough velocity reduction or baryon stopping due to collisions. The energy density generated by the collision is left near the collision point, which thermally equilibrates to create high-temperature matter, while the quark number density of matter itself is small there because quarks and anti-quarks are created by pair production. In addition, as $\sqrt{s_{NN}}$ increases, the energy density near the collision point increases and the initial temperature also rises. On the other hand, in low-energy collisions, nucleon-nucleon interactions increase and the initial kinetic energy of the colliding nucleons is also lower so that nucleons in the incident nucleus tend to stop near the collision point. This leads to the increase of the quark number density of the produced matter. Of course, if $\sqrt{s_{NN}}$ is reduced too much, either the incident nuclei will not make contact, or if they do, they will not be compressed sufficiently so that a significant density increase can not be expected.

Looking back at the history of heavy ion collision experiments, the highest collision energies continued to be updated until the LHC came into operation in 2009. On the other hand, recent theoretical studies have indicated that relatively low-energy collision experiments may reveal rich physical properties of the QCD matter and phase structures. Such challenging investigations have been conducted in the RHIC-BES-II, GSI-HADES, and LHC-NA61/SHINE in the past. Furthermore, high-precision experiments with collision frequencies several orders of magnitude higher than before are planned for future experiments such as the GSI-FAIR, JINR-NICA, and J-PARC-HI as shown in Fig. 1.1 [52]. These experiments may provide us with precise information on the high-density QCD phase diagram and deepen the understanding of their phase structure.

1.3.1 Dilepton productions in HIC

In HIC experiments, particles that can be observed by detectors are hadrons, leptons, and photons. The last two are called the electromagnetic (EM) probes. The hadronic and EM signals have qualitatively different characters. Hadrons are strongly interacting particles, and thus they are frequently scattered in the hot strongly interacting medium, whereas its size is the order of 10 fm. In contrast, leptons and photons hardly interact in the medium owing to their colorless natures. Although the

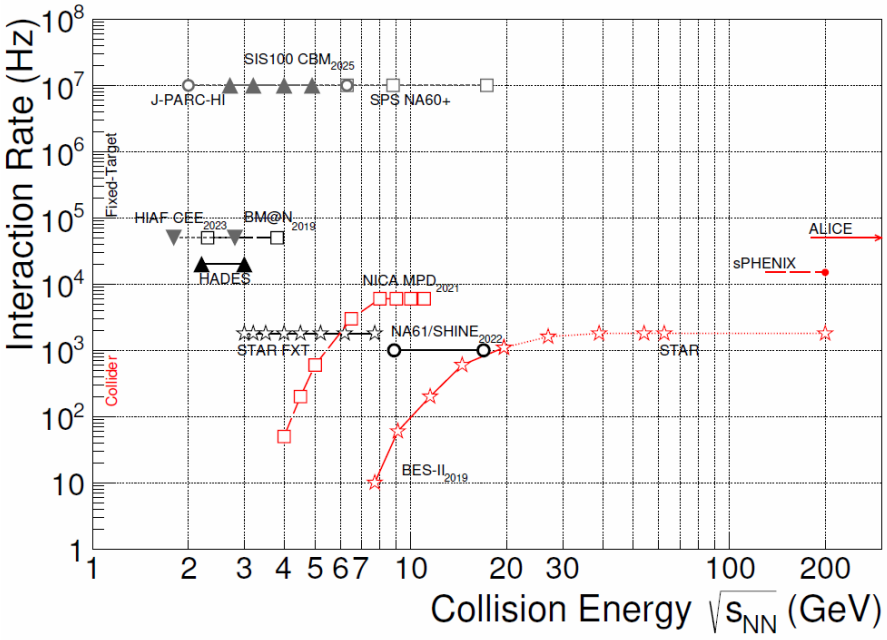

FIGURE 1.1: Heavy ion collision experiments around the world and future plans. [52]

constituents of the hot medium include particles with electric charges, a mean free path of EM interaction is of order 100 fm/c, which is quite longer than the typical size of the hot medium. Therefore, once leptons and photons are produced, they penetrate the hot medium with little scattering, carrying information on their production point and eventually reaching detectors. In this sense, these EM probes are beneficial to study the properties of the hot and dense medium created in the HIC [53]. This is one of the most characteristic features of EM signals observed in HIC experiments.

Another important feature is that they are produced at all stages of the collision process. In principle, EM probes can thus be used to obtain information on all phases of the fireball evolution such as the initial hard scattering processes, the pre-equilibrium phase, the deconfined phase, and the hadron-gas phase. As described earlier, the relatively low-energy experiments that can explore the phase structure of dense QCD are being conducted and planned. If the system created by the collisions undergoes and/or approaches the first-order phase transition, the QCD-CP, or the CSC phase, we may obtain information on their phase structure in dense QCD [54]. However, the information is convoluted with the space-time evolution of the medium. This fact makes it difficult to extract information on specific phases such as thermally equilibrated QGPs and hadronic gas phases. In other words, photons and leptons are observed as a sum over various sources with space-time evolution of collisions. EM probes are good observables to investigate hot and dense matter, while extracting their properties is not an easy task.

In this Thesis, we consider leptons as the EM probe. Real photons are on-shell states, while the virtual photons are off-shell states. Produced virtual photons are finally converted to a lepton and an anti-lepton pair. The invariant mass of the lepton pair is the same as the one of the virtual photon. The lepton pair is called 'dileptons'. Dilepton production rates and their invariant mass spectra are the observables that are directly related to the kinematics of the EM spectral function in the time-like region.

1.3.2 Experimental data of DPR

As described above, dileptons are produced from various processes at all stages of the space-time evolution as well as real photons. Hence, a theoretical understanding of the underlying production mechanism of EM probes within the various stages is imperative for a robust interpretation of their production spectra. In the initial states, nucleons begin to create hot matter by collisions,

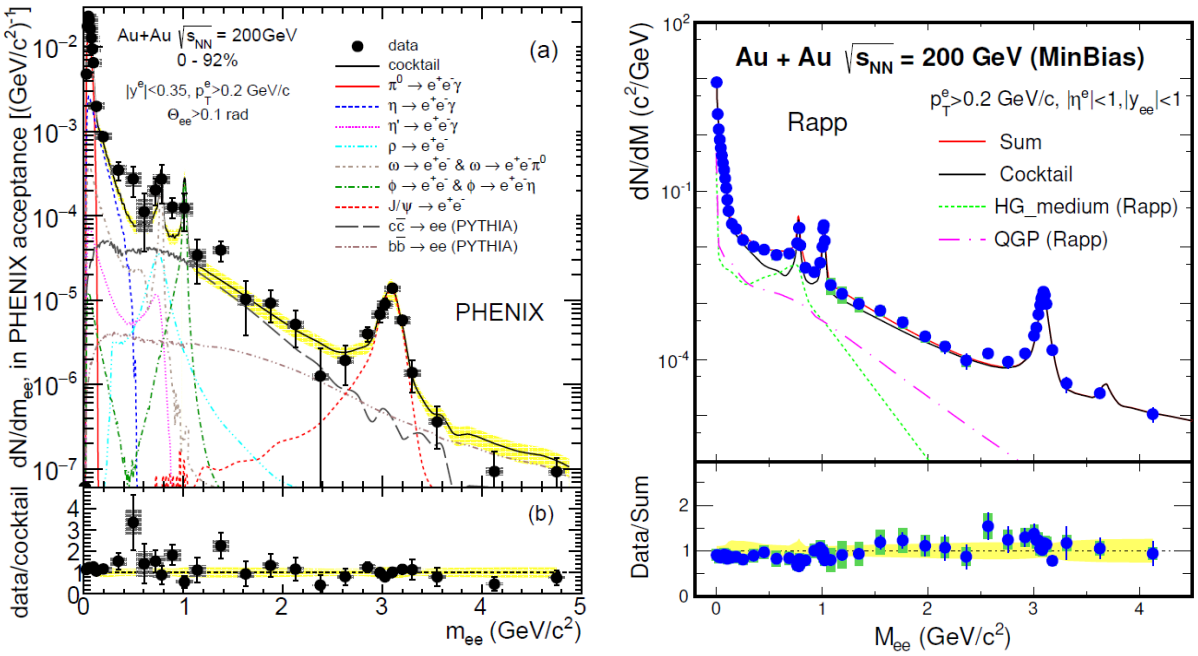

FIGURE 1.2: Invariant mass spectra of dileptons measured in RHIC. **Left panel**: measured by PHENIX collaboration [55] in Au+Au collisions at $\sqrt{s_{NN}} = 200$ GeV, where results are compared to cocktail sources originating from the decay of light mesons (π_0, η, η'), the decay of vector mesons (ρ, ω, ϕ, J/ψ), the decay of correlated charm($c\bar{c}$) and bottom ($b\bar{b}$). **Right panel**: measured by PHENIX collaboration [56] in Au+Au collisions at $\sqrt{s_{NN}} = 200$ GeV, where results are compared to known cocktail sources.

where hadrons involved in the reaction interact with each other and are unable to move out of the matter, while EM probes, by their very nature, can escape unharmed from the medium. The dominant mechanisms behind EM radiation of the HIC change from nucleon-nucleon bremsstrahlung at low energies to parton-parton interactions such as Drell-Yan and heavy-flavor production at ultra-relativistic processes. In the HIC, these sources dominate the dilepton production at higher invariant mass ranges. The high energy densities reached in the initial stages of the collisions set the next stage for the formation of a partonic system that will rapidly expand and locally equilibrate. From this stage, many EM probes are created through the thermal processes with invariant masses in the intermediate range, i.e. between the masses of ρ and J/Ψ mesons.

The collision system continues to expand and the energy density and temperatures drop, the color degrees of freedom are confined again to color-singlet states. Within such a hot and dense hadron gas, inelastic collisions can still take place and change the individual particle species. Eventually, the temperature decreases to a point where inelastic interactions no longer occur and the particle ratios are fixed. This is called the chemical freeze-out as it fixes the chemical composition of the system. The hot hadron gas will continue to expand and interact until the average interaction length between the hadrons becomes comparable to the size of the system. At this stage, the hadrons decouple and the system undergoes a kinetic freeze-out. EM radiations not only include the thermal photons but also contributions from hadron decays. In particular, the dileptons from the decay of light hadrons, such as π_0 and η (the Dalitz decay), overwhelmingly dominate at low energies, while EM radiations from vector mesons are visible at higher energies near their respective masses.

Here, let us see the experimental results of the dilepton production rates. Figure 1.2 shows the results of dilepton (dielectron) production yields in Au+Au collisions at $\sqrt{s_{NN}} = 200$ GeV [55, 56]. These production yields were observed by the two collaborations at RHIC: PHENIX and STAR. The data is compared with the 'hadronic cocktail'. The physical sources of the cocktail originate in a

range of the decay of light mesons to leptons ($\pi_0 \to \gamma e^+e^-$, $\eta \to \gamma e^+e^-$, $\eta' \to \gamma e^+e^-$, $\rho \to e^+e^-$, $\omega \to \pi_0 e^+e^-$ or $\to \eta e^+e^-$ at the low invariant mass, $\phi \to e^+e^-$, $\phi \to \eta e^+e^-$, $J/\psi \to e^+e^-$ at the intermediate mass).

In the case of collision systems where the sources of the hadronic cocktail are well-established, measured yields and momentum spectra can be analyzed in Monte-Carlo simulations, which will utilize the known dilepton branching ratios [57] to generate the dilepton continuum considering the detector's unique features such as acceptance and momentum resolution. On the other hand, in the case that there is no such reference data, yield interpolations combined with Tsallis Blast-Wave fits based on other particles can be used [58]. Moreover, the Dalitz decays are dealt with differently from direct decays which follow narrow Breit-Wigner mass distributions. This distribution follows a Kroll-Wada distribution [59, 60].

The hadronic cocktail consists of all known physical sources that contribute to the dilepton continuum as described above. The analyses for pp collisions often include the contribution of ρ meson in this cocktail. On the other hand, the analyses for A + A collisions do not necessarily involve it, where the behavior of the ρ meson can be modified by the medium effect. There are theoretical approaches to describe vector (ρ) meson spectral functions in a thermal medium such as the vector meson dominance [61], low-density expansions and chiral mixing [62, 63], the lattice QCD [64], chiral and QCD sum rules [65], and the massive Yang-Mills approach [66].

1.3.3 Theoretical aspects of Dilepton production rates

Dilepton production rates

The dilepton can be utilized in a variety of ways to investigate the characteristics of the hot and dense matter created by HIC as well as the photon. In particular, the dilepton production rate (DPR) and its invariant mass spectrum are the observables that can access directly the EM spectral functions and their energy/momentum dependence.

The DPR can be calculated by the thermal field theory [67, 68, 69]. At the leading order of EM interaction, the photon self-energy is given by the EM current-current correlation function in the imaginary-time formalism

$$\tilde{\Pi}^{\mu\nu}(k) = \int d^4x e^{ik\cdot x} \tilde{\Pi}^{\mu\nu}(x), \tag{1.8}$$

$$\tilde{\Pi}^{\mu\nu}(x) = -i\langle T_\tau[J^\mu(x), J^\nu(0)]\rangle, \tag{1.9}$$

where $\langle\cdot\rangle$ and T_τ denote the ensemble average and the imaginary-time ordered operator. Also, $J^\mu(x) = (\boldsymbol{j}(x), n(x))$ and $k = (\boldsymbol{k}, i\nu_l)$ are the electromagnetic current and the four-momentum of the virtual photons. The retarded self-energy is obtained by the analytic continuation $i\nu_l \to \omega + i\eta$ with the positive infinitesimal number η. Then, the thermal production rate of dileptons is given in terms of the retarded photon self-energy by

$$\frac{d^4\Gamma}{d^4k}(\boldsymbol{k}, \omega) = -\frac{\alpha_{EM}}{12\pi^4} \frac{1}{\omega^2 - \boldsymbol{k}^2} \frac{1}{e^{\omega/T} - 1} g_{\mu\nu} \mathrm{Im}\Pi^{R\mu\nu}(\boldsymbol{k}, \omega) \tag{1.10}$$

with the fine structure constant $\alpha_{EM} = 1/137$ and the Minkowski metric $g_{\mu\nu}$. Eq. (1.10) represents the process that a virtual photon with the four-momentum k decays to the dilepton with the same momentum k. Accordingly, medium effects are incorporated through the photon self-energy. From Eq. (1.10), analyses of thermal rates are converted to the problem of how to evaluate the photon self-energy. If there are dilepton production processes to be taken into account, one only needs to calculate the corresponding self-energy.

Theoretical studies of the current-current correlation function (1.8) in the framework of thermal field theory have a long history. At weak coupling and large temperatures, the perturbative QCD calculations are possible [70, 71, 72]. At $\mu_B = 0$, the lattice QCD simulations have been conducted for the non-perturbative region [73, 74, 75], which require numerically ill-defined analytic

continuations to obtain real-time quantities of experimental relevance since they accommodate the Euclidean times. Also, the DPR can be calculated on the basis of the microscopic framework of relativistic kinetic theory, e.g. [76].

Associated transport coefficients

It is known that the low energy and momentum behavior of the DPR encodes directly the transport coefficients appearing in the relativistic fluid dynamics through the photons self-energy (1.8). The relation between the production rate, transport coefficients, and self-energy has been given by [77].

To see the relation, let us start with the EM charge conservation law

$$\nabla_\mu J^\mu(x) = 0. \tag{1.11}$$

In fluid dynamics, the space-time evolution of the EM current is described by the electric charge conservation law together with a constitutive equation, which is given in terms of a derivative expansion of $J^\mu(x)$. Let the constitutive equation take the following form

$$J^\mu(x) + \tau_\sigma \Delta^\mu{}_\nu u^\alpha \nabla_\alpha J^\nu(x) = n(x)u^\mu + \sigma \Delta^{\mu\alpha} E_\alpha(x) - D\Delta^{\mu\beta}\nabla_\beta n(x) \tag{1.12}$$

where u^μ is the fluid velocity with normalization $u^\mu u_\mu = 1$ and $\Delta^{\mu\nu} = g^{\mu\nu} + u^\mu u^\nu$ is the projector orthogonal to the velocity. The expansion coefficients are the electric conductivity σ, relaxation time τ_σ, and diffusion constant D, which are the transport coefficients, while the electric field is denoted by $E^\mu(x) = \Delta^{\mu\nu}u^\rho F_{\nu\rho}(x)$ with the electric field strength tensor $F_{\mu\nu}(x) = \nabla_\mu A_\nu(x) - \nabla_\nu A_\mu(x)$. In Eq. (1.12), the second term on the left-hand side is introduced to ensure relativistic causality with the relaxation time τ_σ, which gives the time scale that the current $J^\mu(x)$ relaxes towards the local form that Ohm's and Fick's law are satisfied. Eqs. (1.11) and (1.12) give equations of motions for all components of $J^\mu(x)$. Then, using $J^\mu(x)$ constructed in this way, we can obtain the current-current correlation function (1.9). It is noted that the conservation law $\nabla_\mu \tilde{\Pi}^{\mu\nu}(x) = 0$ is satisfied, which leads to the Ward identity for the photon self-energy $k_\mu \tilde{\Pi}^{\mu\nu}(k) = 0$.

In the analysis of the DPR (1.10), we have to calculate the trace of the retarded photon self-energy. In this Thesis, we call its imaginary part the spectral density of the self-energy

$$\rho(\boldsymbol{k}, \omega) = g_{\mu\nu}\mathrm{Im}\Pi^{R\mu\nu}(\boldsymbol{k}, \omega). \tag{1.13}$$

Accordingly to Ref. [78], the spectral density (1.13) in the rest frame $u = (\boldsymbol{u}, u_0) = (0, 0, 0, 1)$ at low energy/momentum can be related to the transport coefficients as follows

$$\begin{aligned}\rho(\boldsymbol{k}, \omega) &= g_{\mu\nu}\mathrm{Im}\Pi^{R\mu\nu}(\boldsymbol{k}, \omega) \\ &= \frac{\sigma\omega(\omega^2 - \boldsymbol{k}^2)}{(\tau_\sigma\omega^2 - D\boldsymbol{k}^2)^2 + \omega^2} + \frac{2\sigma\omega}{\tau_\sigma^2\omega^2 + 1},\end{aligned} \tag{1.14}$$

where the first and second terms correspond to the longitudinal and transverse components of the photon self-energy. From this, one can read off the values of σ, τ_σ, and D by considering the derivative of $\rho(\boldsymbol{k}, \omega)$ and taking the $(\boldsymbol{k}, \omega) \to (\boldsymbol{0}, 0)$ limit as follows

$$\sigma = \frac{1}{3}\frac{\partial\rho(\boldsymbol{0}, \omega)}{\partial\omega}\bigg|_{\omega=0}, \quad \tau_\sigma^2 = -\frac{1}{18\sigma}\frac{\partial^3\rho(\boldsymbol{0}, \omega)}{\partial^3\omega}\bigg|_{\omega=0}, \quad D = \frac{1}{2\sigma\tau_\sigma}\frac{\partial}{\partial\omega}\left(\frac{\partial\rho(\boldsymbol{k}, \omega)}{\partial\boldsymbol{k}^2}\bigg|_{\boldsymbol{k}=\boldsymbol{0}}\right)\bigg|_{\omega=0}. \tag{1.15}$$

In this way, we can obtain the expression of σ, τ_σ, and D described by the spectral density $\rho(\boldsymbol{k}, \omega)$. One can also find the transport coefficients are related to the low energy/momentum behavior of the DPR (1.10) through the photon self-energy. We note that the photon self-energy has to satisfy the Ward identity when Eq. (1.15) is used because of Eq. (1.11).

There are various theoretical studies to determine the electric conductivity σ of QGP. The lattice QCD calculations lead to the range of value $0.003 < \sigma/T < 0.018$ [79], where a fit to a specific

ansatz for the spectral function is used to obtain it from the Euclidean correlation functions on the lattice. In the high-temperature limit, σ can be computed to leading log approximation within the effective kinetic theory [80, 81]. In these works, quarks and leptons are considered, while excluding the leptons leads to the range $0.19 < \sigma/T < 2.00$.

While such theoretical efforts have been made on electrical conductivity, the experimental observations of σ are still very challenging because the transport coefficients are related to the ultra low energy/momentum limit of the DPR. However, the direct experimental analysis in the HIC has been proposed recently, e.g. [82].

1.4 Purpose and Organization

In this Thesis, we explore how the soft modes due to the 2SC-PT and QCD-CP affect the DPR in order to discuss the observability of the 2SC phase and QCD-CP in the HIC experiments. As described in Sec. 1.2, the 2SC-PT and QCD-CP soft modes are low-energy collective excitation modes that are formed by amplitude fluctuations of the diquark condensate and chiral condensate, respectively. Since their modes develop significantly around the respective phase transition, they can cause various critical phenomena and affect observables in HIC if a system created by HIC approaches the 2SC-PT and QCD-CP. For the analysis of the DPR, we construct the photon self-energy that involves the soft modes so as to satisfy the Ward identity and calculate it on the basis of the two-flavor Nambu-Jona-Lasinio (NJL) model. Furthermore, we investigate the effect of the soft modes on the transport coefficients, electric conductivity and relaxation time. As described in Sec. 1.3, the low energy/momentum limit of the DPR is related to the transport coefficients appearing in the relativistic fluid dynamics through the photons self-energy. Through this analysis, we reveal the difference in the effect of the 2SC-PT and QCD-CP soft modes on the DPR.

The outline of this paper is as follows. In the Chapter 2, we make a review of the phenomenology of the fluctuation due to the second-order phase transition, which is useful for understanding the critical properties of the CSC-PT and QCD-CP soft modes. In particular, it is described that the critical exponents of the susceptibility, coherence length, and relaxation time of the fluctuations depend on the way to approach the critical point. In Chapter 3, the finite temperature and density quantum field theory is reviewed since we evaluate the soft modes and the photon self-energy based on this theory to analyse them microscopically in the system with finite T and μ_B. We also describe the linear response theory in the finite T and μ_B system.

Next, we describe our formalism for studying the effect of the soft modes on the DPR and associated transport coefficients. In Chapter 4, we introduce the two-flavor NJL model to evaluate the 2SC-PT and QCD-CP. We firstly evaluate the thermodynamic potential by the mean-field approximation (MFA) explicitly, and then show the phase diagram calculated by using the potential. In Chapter 5, we calculate the 2SC-PT and QCD-CP soft modes by the random phase approximation. By evaluating both soft modes parallelly, we show the differences between the respective modes. The critical behavior of the soft modes is described by noting the Thouless criterion. Moreover, we approximate the soft modes on the basis of the Ginzburg-Landau theory, where the two types of the approximation method introduced: the low-energy (LE) approximation and the time-dependent Ginzburg-Landau (TDGL) approximation. In Section 6, we construct the photon self-energy including the respective soft mode so as to satisfy the Ward identity, where the Aslamazov-Larkin (AL), Maki-Thompson (MT), and density of states (DOS) terms are considered as such a photon self-energy, which are well known in the condensed matter theory. This self-energy possesses the three-momentum integral, and its calculation is quite difficult. Then, we approximate the vertex functions appearing the self-energy based on both LE and TDGL approximation. These treatments also satisfy the Ward identity for the self-energy.

Finally, we show the results obtained by using the photon self-energy that is constructed in Chapter 6. First of all, in Chapter 7, the results of the transport coefficients are shown to describe the critical effects of the soft modes on the DPR, where the divergence of the coefficients and their different critical exponents due to the soft modes are described analytically and numerically. This

study is based on Ref. [83]. After that, we show the numerical results of the DPR in Chapter 8. In this chapter, the production rates per unit energy and momentum and the invariant-mass spectra are shown in Sec 8.2 and Sec. 8.3, respectively. These results tell us that the DPR is significantly enhanced owing to the 2SC-PT and QCD-PT soft modes that develop near the respective phase transitions. This study is based on Refs. [84, 85].

In this Thesis, we use the natural unit where $\hbar = c = k_B = 1$ with $\hbar$, c, k_B being the Planck constant, the speed of light, and the Boltzmann constant, respectively.

Chapter 2

Phenomenology of Critical Fluctuations

It is well known that various quantities diverge near a second-order phase transition, for instance, fluctuations of order parameters or/and conserved charges. To understand such critical phenomena, mean-field theories have been utilized, where the idea of the order parameter Φ is introduced. In this Chapter, we review critical fluctuation and their phenomena due to a second-order phase transition. First of all, the Ginzburg-Landau theory is reviewed to understand the origin of the critical phenomena in Sec. 2.1. In Sec. 2.2, we expand discussions to time-dependent systems and introduce the time-dependent Ginzburg-Landau equation. Finally, in Sec. 2.3 we discuss fluctuations near the QCD-CP by applying the knowledge of the previous sections.

2.1 Ginzburg-Landau theory

The Ginzburg-Landau (GL) theory is a theoretical framework that provides a phenomenological description of second-order phase transitions. It was developed by Landau and Ginzburg. This theory is particularly useful for understanding the behavior of systems near critical points where phase transitions occur.

2.1.1 Homogeneous system

Let us start from the Landau theory, where a system is assumed homogeneous. For simplicity, let an order parameter Φ be a real constant. The free energy density is given by

$$f(\Phi) = \frac{1}{2}A(t)\Phi^2 + \frac{1}{4}B\Phi^4 - h\Phi, \tag{2.1}$$

where A and B are functions of temperature T, while h is an external field. In Eq. (2.1), we assume $A(t) = A_0 t$ with a positive constant A_0 and the reduced temperature $t = (T - T_c)/T_c$, where T_c is a critical temperature, while B are positive constants. The physical state is taken at the minimum point of $f(\Phi)$, whose stationary condition (2.10) is

$$\frac{\partial f(\Phi_0)}{\partial \Phi_0} = A(t)\Phi_0 + B\Phi_0^3 - h = 0, \tag{2.2}$$

where Φ_0 denotes the physical value of Φ.

When $h = 0$, the free energy density $f(\Phi)$ is invariant for the transformation $\Phi \to -\Phi$, which is a global symmetry called the discrete Z_2 symmetry. From the stationary condition (2.2), we find

$$\Phi_0(t, h = 0) = \begin{cases} 0 & \text{for} \quad t \geq 0, \\ \pm(-A(t)/B)^{1/2} = \Phi_{0\pm} & \text{for} \quad t < 0. \end{cases} \tag{2.3}$$

At $t < 0$, the free energy density itself has the Z_2 symmetry, while $\Phi_0(t, h)$ is chosen to either Φ_{0+} or Φ_{0-}, which is the spontaneous symmetry breaking. In this sense, the point $(t, h) = (0, 0)$ is the second-order phase transition and its point is called the critical point. On the other hand, when

$h \neq 0$, the Z_2 symmetry is explicitly broken. When $t \geq 0$, since $f(\Phi)$ has only one minimum, the value of $\Phi_0(t,h)$ varies smoothly, and its sign changes at $h = 0$. Such a change is often called the crossover transition. When $t < 0$, the free energy density $f(\Phi)$ has two minima near the line of $h = 0$ and the value of $\Phi_0(t,h)$ jumps there, which is the first-order phase transition.

To see the critical behavior described by $f(\Phi_0)$, we investigate the susceptibility of Φ

$$\chi(t,h) = \frac{\partial \Phi_0(t,h)}{\partial h} = \frac{1}{A(t) + 3B\Phi_0^2(t,h)}. \tag{2.4}$$

Using Eq. (2.3), the behavior of $\Phi(t,h)$ at $h = 0$ is

$$\chi(t,h=0) = \begin{cases} A^{-1}(t) & \text{for} \quad t \geq 0 \quad \text{(along crossover)}, \\ -2A^{-1}(t) & \text{for} \quad t < 0 \quad \text{(along 1st-PT)}. \end{cases} \tag{2.5}$$

From this, it is found that $\chi(t,h)$ diverges as $|t| \to 0$ at $h = 0$ and its magnitude depends on the direction in which the system approaches the critical point.

Moreover, we consider other ways of approaching the critical point. Since Eq. (2.2) is a cubic equation, we can obtain three exact solutions by using the Cardano's formula and find the behavior of $\Phi_0(t,h)$ near the critical point $(t,h) = (0,0)$ as follows [1]

$$\Phi_0(t,h) \sim \begin{cases} |t|^{1/2} & \text{for} \quad |A(t)/3B|^3 \geq |h/2B|^2, \\ |h|^{1/3} & \text{for} \quad |A(t)/3B|^3 < |h/2B|^2. \end{cases} \tag{2.6}$$

Then, one can find that the critical exponent of $\chi(t,h)$ is dependent on the approaching way to the critical point as follows

$$\chi(t,h) \sim \begin{cases} |t|^{-1} & \text{for} \quad |A(t)/3B|^3 \geq |h/2B|^2, \\ |h|^{-2/3} & \text{for} \quad |A(t)/3B|^3 < |h/2B|^2. \end{cases} \tag{2.7}$$

In particular, when $(t,h) \to (0,0)$ linearly, the exponent $-1/2$ occurs only when approaching along the line of $h = 0$.

Finally, let us discuss the origin of the divergence in Eqs. (2.5) and (2.7). One can find that the curvature of the free energy density at the bottom is consistent with the inverse of the susceptibility (2.4)

$$\frac{\partial^2 f(\Phi_0)}{\partial^2 \Phi_0} = A(t) + 3B\Phi_0^2(t,h) = \chi^{-1}(t,h). \tag{2.8}$$

Since the curvature is zero at second-order phase transitions, the susceptibility diverges there. This is the nature of the critical phenomena due to the second-order phase transition. Other critical phenomena can also be understood through this discussion of the curvature.

[1] Rewriting Eq. (2.2) as $\Phi_0^3 + p\Phi_0 - q = 0$ with $p = 3A(t)/B = 3A_0 t/B$ and $q = 2h/B$, its solutions are

$$\Phi_k(t,h) = \omega^k \left[q^2 + \sqrt{q^2+p^3}\right]^{1/3} + \omega^{3-k}\left[q^2 - \sqrt{q^2+p^3}\right]^{1/3} \quad \text{for} \quad k = 1,2,3$$

with $\omega = e^{3/\pi}$. Out of $k = 1,2,3$, at least one is a real solution (the number of real solutions is counted by the discriminant $D = -(q^2+p^3)$). The physical state is chosen to a real solution $\Phi_k(t,h)$ that $f(\Phi_k(t,h))$ is minimal among them. As one finds, when $(t,h) \to (0,0)$ within $|p|^3 > |q|^2$, $\Phi_k(t,h) \sim |p|^{1/2}$ since $p = 3A_0 t/B$, $q = 2h/B$, and $|p|^3$ decrease more rapidly than $|q|^2$, while when $|p|^3 < |q|^2$, $\Phi_k(t,h) \sim |q|^{2/3}$.

2.1.2 Inhomogeneous system

Next, we consider the inhomogeneous system, where the order parameter has the spatial dependence $\Phi(\boldsymbol{x})$. In this case, the Landau free energy is given by

$$F[\Phi(\boldsymbol{x})] = \int d^3x \left[\frac{1}{2}A(t)\Phi^2(\boldsymbol{x}) + \frac{1}{4}B\Phi^4(\boldsymbol{x}) + \frac{1}{2}\kappa\big(\nabla\Phi(\boldsymbol{x})\big)^2 - h(\boldsymbol{x})\Phi(\boldsymbol{x}) \right], \tag{2.9}$$

where $A = A_0 t$ with a positive constant A_0, while B and κ are positive constants. The physical state is is taken at the minimum point of $F[\Phi(\boldsymbol{x})]$ and its stationary conditions is given by

$$\frac{\delta F[\Phi_0(\boldsymbol{x})]}{\delta\Phi_0(\boldsymbol{x})} = \left[A(t) + B\Phi_0^2(\boldsymbol{x}) - \kappa\nabla^2\right]\Phi_0(\boldsymbol{x}) - h(\boldsymbol{x}) = 0, \tag{2.10}$$

where $\Phi_0(\boldsymbol{x})$ is the physical configuration. Eq. (2.10) is called the GL equation. Assuming deviations of $h(\boldsymbol{x})$ and $\Phi_0(\boldsymbol{x})$ from homogeneous solutions are small, $h(\boldsymbol{x}) = h + \delta h(\boldsymbol{x})$ and $\Phi_0(\boldsymbol{x}) = \Phi_0 + \delta\Phi_0(\boldsymbol{x})$, and considering up to the first order of deviations, we obtain the linearized equation

$$\delta h(\boldsymbol{x}) = \left[A(t) + 3B\Phi_0^2 - \kappa\nabla^2\right]\delta\Phi_0(\boldsymbol{x}). \tag{2.11}$$

This solution can be written by using the Green's function as

$$\delta\Phi_0(\boldsymbol{x}) = \int d^3x' G(\boldsymbol{x}-\boldsymbol{x}')\delta h(\boldsymbol{x}), \tag{2.12}$$

$$\delta(\boldsymbol{x}-\boldsymbol{x}') = \left[A(t) + 3B\Phi_0^2 - \kappa\nabla^2\right]G(\boldsymbol{x}-\boldsymbol{x}'). \tag{2.13}$$

Through the Fourier transformation, we obtain the Green's function

$$G(\boldsymbol{x}-\boldsymbol{x}') = \int \frac{d^3q}{(2\pi)^3} e^{i\boldsymbol{q}\cdot(\boldsymbol{x}-\boldsymbol{x}')} G(\boldsymbol{q}), \tag{2.14}$$

$$G(\boldsymbol{q}) = \frac{1}{A(t) + 3\Phi_0^2 + \kappa\boldsymbol{q}^2} = \frac{1}{\kappa}\frac{1}{\xi_{GL}^{-2} + \boldsymbol{q}^2}, \tag{2.15}$$

where the coherence length is defined as

$$\xi_{GL} = \sqrt{\frac{\kappa}{A(t) + 3\Phi_0^2(t,h)}}\,. \tag{2.16}$$

The coherence length is a characteristic scale of length for spatial variations of the order parameter, which is confirmed as follows: Firstly, let us consider the meaning of the Green's function. By considering Eq. (2.11) in the Fourier space, one finds $G(\boldsymbol{q}) = \delta\Phi_0(\boldsymbol{q})/\delta h(\boldsymbol{q})$. Moreover, taking the limit $\boldsymbol{q} \to \boldsymbol{0}$, it is consistent with the definition of the susceptibility (2.4), which means that the Green's function is the correlation function of the order parameter. Next, we calculate Eq. (2.14) using Eq. (2.15),

$$\begin{aligned}
G(\boldsymbol{x}-\boldsymbol{x}') &= \frac{1}{\kappa}\int \frac{d^3k}{(2\pi)^3}\frac{e^{i\boldsymbol{k}\cdot(\boldsymbol{x}-\boldsymbol{x}')}}{\xi_{GL}^{-2} + \boldsymbol{q}^2} \\
&= \frac{1}{\kappa}\int \frac{d^3k}{(2\pi)^3}\int_0^\infty dt \exp[i\boldsymbol{k}\cdot(\boldsymbol{x}-\boldsymbol{x}') - t(\xi_{GL}^{-2} + \boldsymbol{q}^2)] \\
&= \frac{1}{\kappa}\int_0^\infty dt \frac{1}{(4\pi t)^{3/2}} \exp\left[-\frac{(\boldsymbol{x}-\boldsymbol{x}')^2}{4t} - \frac{t}{\xi_{GL}^2} \right] \\
&= \frac{|\boldsymbol{x}-\boldsymbol{x}'|}{\kappa}\int_0^\infty dz \frac{1}{(4\pi|\boldsymbol{x}-\boldsymbol{x}'|z)^{3/2}} \exp\left(-|\boldsymbol{x}-\boldsymbol{x}'|\left[\frac{1}{4z} + \frac{z}{\xi_{GL}^2}\right] \right),
\end{aligned} \tag{2.17}$$

where in the second equality, the integrand is deformed in the form of an exponential function with an auxiliary variable t, and in the last equality, $z = t/|\boldsymbol{x} - \boldsymbol{x}'|$ is introduced. When $|\boldsymbol{x} - \boldsymbol{x}'|$ is sufficiently large, the far left-hand side is estimated by the saddle-point method. In this case, the saddle point is $z = \xi_{GL}/2$, we obtain the asymptotic form of $G(\boldsymbol{x} - \boldsymbol{x}')$

$$G(\boldsymbol{x} - \boldsymbol{x}') = \frac{e^{-|\boldsymbol{x}-\boldsymbol{x}'|/\xi_{GL}}}{4\pi\kappa|\boldsymbol{x} - \boldsymbol{x}'|} \quad \text{for} \quad |\boldsymbol{x} - \boldsymbol{x}'| \gg \xi_{GL}, \tag{2.18}$$

which is known as the Ornstein-Zernike formula. From this, the coherence length gives a typical scale for spatial variations of the order parameter. Finally, we mention the critical exponent of ξ_{GL}. Using Eqs. (2.6) and (2.4), one finds

$$\xi_{GL} \sim \begin{cases} |t|^{-1/2} & \text{for} \quad |A(t)/3B|^3 \geq |h/2B|^2, \\ |h|^{-1/3} & \text{for} \quad |A(t)/3B|^3 < |h/2B|^2, \end{cases} \tag{2.19}$$

which can be checked by the fact of $\xi_{GL}^2 = \kappa\chi$ and Eq. (2.7).

2.2 Time-dependent Ginzburg-Landau equation

To treat the time dependence of the order parameter, we introduce the Time-dependent Ginzburg-Landau (TDGL) equation. A simple extension of the GL equation (2.10) is

$$\gamma_{\mathrm{GL}} \frac{\partial \Phi(\boldsymbol{x}, t)}{\partial t} = -\frac{\delta F(\Phi(\boldsymbol{x}, t)}{\delta \Phi(\boldsymbol{x}, t)} + \zeta(\boldsymbol{x}, t), \tag{2.20}$$

where $\zeta(\boldsymbol{x}, t)$ is the Langevin force. The correlation of $\zeta(\boldsymbol{x}, t)$ is local in spacetime and its magnitude is determined by the fluctuation-dissipation relation as

$$\langle \zeta(\boldsymbol{x}, t) \rangle = 0, \quad \langle \zeta(\boldsymbol{x}_1, t_1)\zeta(\boldsymbol{x}_2, t_2) \rangle = \frac{2T}{\gamma_{GL}} \delta(\boldsymbol{x_1} - \boldsymbol{x_2})\delta(t_1 - t_2). \tag{2.21}$$

This equation describes the behavior that the non-equilibrium state ($\partial\Phi/\partial t \neq 0$) is relaxing to the equilibrium state ($\partial\Phi/\partial t = 0$). Eq. (2.20) is called the time-dependent Ginzburg-Landau (TDGL) equation. Substituting Eq. (2.9) into Eq. (2.20), we obtain

$$\left[\gamma_{\mathrm{GL}} \frac{\partial}{\partial t} + A(t) + B\Phi^2(\boldsymbol{x}, t) - \kappa\nabla^2\right] \Phi(\boldsymbol{x}, t) = \zeta(\boldsymbol{x}, t), \tag{2.22}$$

where the external field $h(\boldsymbol{x}, \boldsymbol{t})$ is neglected for simplicity.

As in Eqs. (2.12) and (2.13), assuming that the deviations of $\zeta(\boldsymbol{x}, \boldsymbol{t})$ and $\Phi_0(\boldsymbol{x}, \boldsymbol{t})$ are small and linearizing Eq. (2.22), we can obtain the time-dependent correlation function

$$G(\boldsymbol{x}, t) = \int \frac{d^3q d\omega}{(2\pi)^4} e^{i\omega t - i\boldsymbol{q}\cdot\boldsymbol{x}} G(\boldsymbol{q}, \omega), \tag{2.23}$$

$$G(\boldsymbol{q}, \omega) = \frac{1}{A(t) + B\Phi_0^2 + \kappa\boldsymbol{q}^2 + i\gamma_{GL}\omega}. \tag{2.24}$$

Let us consider the dynamics described by the TDGL equation. Neglecting the nonlinear term $B\Phi_0^2(\boldsymbol{x}, t)$ for simplicity and carrying out the Fourier transformation for the spatial coordinate, we obtain the following result

$$\Phi(\boldsymbol{q}, t) = \Phi(\boldsymbol{q}, 0)\, e^{-t/\tau_{GL}(q)} \tag{2.25}$$

with

$$\tau_{GL}(\boldsymbol{q}) = \frac{\gamma_{GL}}{A(t) + \kappa \boldsymbol{q}^2}, \tag{2.26}$$

where $\tau_{GL}(\boldsymbol{q})$ is the relaxation time. From this, it is found that $\tau_{GL}(\boldsymbol{q})$ gives the typical time scale of the relaxation of Φ. One finds that $\tau_{GL}(\boldsymbol{0})$ is divergent at the critical point because $A(0) = 0$, which means that the fluctuation of the order parameter takes an infinite time to relax to an equilibrium state in the low momentum limit.

It is known that the TDGL equation (2.20) can be derived from the microscopic theory in the normal phase above T_c. As T approaches T_c, the correlation function (2.24) becomes divergent in the low energy/momentum limit. As described in Sec. 5.3.1, the dynamics of fluctuation of the diquark condensate obey the TDGL equation.

2.3 Fluctuations near the QCD-CP

In this section, we discuss the fluctuation of the QCD-CP based on the GL theory [20, 21]. We start from the following free energy

$$\Omega(T, \mu, h; \sigma) = \int d^3x f(T, \mu, h; \sigma) = V f(T, \mu, h; \sigma), \tag{2.27}$$

$$f(T, \mu, h; \sigma) = A\sigma^2 + B\sigma^4 + C\sigma^6 - h\sigma, \tag{2.28}$$

where σ is the chiral condensate. The coefficients A, B, and C are functions of temperature T and chemical potential μ_B, where $C > 0$ is assumed for stability. In Eq. (2.28), the pseudoscalar density is ignored. In the following, we study phase transitions and critical points of a system.

Firstly, we consider the case of $h = 0$. If $B < 0$, the energy density $f(\sigma)$ can be minimized either at $\sigma = 0$ or $\sigma_\pm = \pm\sqrt{-B/2C}$. When $A = B^2/4C$, a symmetric phase ($\sigma = 0$) and a spontaneous symmetry breaking phase ($\sigma_\pm$) coexist. Then, in the T-μ_B plane, the points that satisfies $A(T, \mu_B) = B^2(T, \mu_B)/4C(T, \mu_B)$ give the first-order phase transition line. In this case, $f(\sigma)$ has three minimum points. On the other hand, when $A = B = 0$ at certain T and μ_B, it is found that one minimum point is at $\sigma = 0$. Hence, the set of T and μ_B that satisfies $A = B = 0$ is a second-order phase transition, whose point is called the tri-critical point (TCP). The TCP is the endpoint of the first-order phase transition line. Furthermore, in the case of the line with $A = 0$ and $B > 0$, $f(\sigma)$ is minimized at $\sigma = 0$ and the curvature of $f(\sigma)$ is zero there. Then, this line also represents a second-order phase transition line. Such critical lines are called $O(4)$ critical lines.

When $h \neq 0$, the energy density $f(\sigma)$ has two minimum points on the first-phase transition line. A critical point appears at the end of the transition line. This critical point belongs to the Z_2 universality class as the three-dimensional Ising model. For that, this point is called the Z_2 critical point (Z_2-CP). As described in Sec. 1.2, the QCD-CP is corresponding to the Z_2-CP.

Now, we investigate the susceptibility near the Z_2-CP in order to understand the critical behavior of the QCD-CP. As in Sec. 2.1, the stationary condition for the physical value σ_0 is

$$\left.\frac{\partial f(\sigma)}{\partial \sigma}\right|_{\sigma=\sigma_0} = 2A\sigma_0 + 4B\sigma_0^3 + 6C\sigma_0^5 - h = 0, \tag{2.29}$$

and the chiral susceptibility χ_h is

$$\chi_h = \frac{\partial \sigma_0}{\partial h} = \frac{1}{2A + 12B\sigma_0^2 + 30C\sigma_0^4}. \tag{2.30}$$

One can find that the susceptibility is also given by $\chi_h = -\partial^2 f(\sigma_0)/\partial^2 h$. The free energy $f(\sigma)$ includes the parameters T and μ_B in addition to h, and the second derivatives of $f(\sigma_0)$ with respect

to T and μ_B give the heat capacity and baryon number susceptibility, respectively. Here, instead of them, we examine the susceptibility for h, A, and B. All susceptibilities for h, A, and B are given in terms of χ_h as follows

$$\chi_{ij} = -\frac{\partial^2 f(\sigma_0)}{\partial X_i \partial X_j} = \chi_h \begin{pmatrix} 1 & 2\sigma_0 & 4\sigma_0^3 \\ 2\sigma_0 & 4\sigma_0^2 & 8\sigma_0^4 \\ 4\sigma_0^3 & 8\sigma_0^4 & 16\sigma_0^6 \end{pmatrix} \quad \text{for} \quad X_i = (h, a, b). \tag{2.31}$$

In the derivation of Eq. (2.31), it would be useful to utilize

$$\frac{\partial \sigma_0}{\partial A} = -2\sigma_0 \chi_h, \quad \frac{\partial \sigma_0}{\partial B} = -4\sigma_0^3 \chi_h,$$

which are obtained from Eq. (2.29). In the following, we compare the critical behavior of the susceptibility (2.31) in the case of $h = 0$ and $h \neq 0$.

Firstly, we consider the case of $h = 0$. When approaching from the symmetric phase ($A > 0$) to the $O(4)$ critical line, the non-zero susceptibility is only the chiral susceptibility $\chi_{11} = \chi_h = 1/2A$ owing to $\sigma = 0$. Moreover, χ_{11} diverges just above the critical line because $A \to 0$. Next, examine the case of approaching from the broken phase ($A < 0$) to the critical line. Since A is small near the critical line, it is found from Eq. (2.29) to be

$$\sigma_0^2 = \sqrt{\frac{B^2}{9C^2} - \frac{A}{3C}} - \frac{B}{3C} \sim -\frac{A}{2B}. \tag{2.32}$$

Accordingly, $\chi_{11} = -1/4A$ diverges at the critical line. In contrast to the case of approaching from the symmetric phase, other susceptibilities become finite besides χ_{11}. In particular, $\chi_{22} = 1/3B$ is finite on the $O(4)$ critical line and it diverges on the TCP becauee of $B = 0$. Thereby, not only the chiral susceptibility but also the susceptibility of the quantity conjugate to A diverges at the TCP.

Now, we discuss the divergence of the susceptibility $\chi_{22} = -\partial^2 f(\sigma_0)/\partial^2 A$. Using the entropy density $s = -\partial f(\sigma_0)/\partial T$ and baryon number density $n_B = -\partial f(\sigma_0)/\partial \mu_B$, we find

$$-\frac{\partial f(\sigma_0)}{\partial A} = \frac{\partial T}{\partial A} s + \frac{\partial \mu_B}{\partial A} n_B. \tag{2.33}$$

Since it is known that the entropy density can be written as a linear combination of the energy density and baryon number density, the quantity conjugated to A can be interpreted as a linear combination of conserved quantity densities such as energy density and baryon number density. Fluctuations of such densities are often called hydrodynamic modes. The result that χ_{22} is divergent indicates that hydrodynamic modes develop around the TCP.

Next, let us consider the behavior of the susceptibility near the Z_2-CP, which corresponds the case of $h \neq 0$. Since $(\chi/\chi_h)_{ij}$ is a symmetric matrix, it can be diagonalized by using an orthogonal matrix P as follows

$$\frac{\tilde{\chi}}{\chi_h} = {}^t P \, \frac{\chi}{\chi_h} P, \tag{2.34}$$

where $\tilde{\chi}_{ij} = -\partial^2 f(\sigma)/\partial Y_i \partial Y_j$ and $Y = P^{-1} X = {}^t P X$. With a simple calculation, we obtain the matrix P as follows

$$P = (v_1, v_2, v_3) \quad \text{with} \quad v_1 = \begin{pmatrix} -4\sigma_c^3 \\ -8\sigma_c^4 \\ 1 + 4\sigma_c^2 \end{pmatrix}, \quad v_2 = \begin{pmatrix} -2\sigma_c \\ 1 \\ 0 \end{pmatrix}, \quad v_3 = \begin{pmatrix} 1 \\ 2\sigma_c \\ 4\sigma_c^3 \end{pmatrix}, \tag{2.35}$$

where σ_c is the value of σ_0 near the Z_2 CP. From Eq. (2.34), the diagonalized matrix $\tilde{\chi}$ is

$$\tilde{\chi} = \begin{pmatrix} 0 & 0 & 0 \\ 0 & 0 & 0 \\ 0 & 0 & (1+4\sigma_c^2+16\sigma_c^6)\chi_h \end{pmatrix}. \tag{2.36}$$

Hence, it is found that only the susceptibility conjugate to Y_3 is divergent at the Z_2-CP. Letting σ_c be small and neglecting the second order of σ_c, $X = PY$ is

$$X = \begin{pmatrix} h \\ A \\ B \end{pmatrix} \sim \begin{pmatrix} -2\sigma_c Y_2 + Y_3 \\ Y_2 + 2\sigma_c Y_3 \\ Y_1 \end{pmatrix}. \tag{2.37}$$

Here, let φ be the conjugate field for A and φ_0 be the value that φ takes at $\sigma = \sigma_0$. We can find that the fields conjugate to Y_3 are linearly coupled to σ and φ as follows

$$-\frac{\partial f(\sigma_0)}{\partial Y_3} = -\frac{\partial h}{\partial Y_3}\frac{\partial f(\sigma_0)}{\partial h} - \frac{\partial A}{\partial Y_3}\frac{\partial f(\sigma_0)}{\partial A} - \frac{\partial B}{\partial Y_3}\frac{\partial f(\sigma_0)}{\partial B} \sim \sigma_0 + 2\sigma_c\varphi_0, \tag{2.38}$$

which means that the physical quantity that diverges at the Z_2-CP is the linearly coupled field of the order parameter σ and the conserved quantity density φ owing to the finite σ_c. In other words,

Finally, let us construct a model that takes into account the contribution of the hydrodynamic mode. A simple extension could be as follows

$$f(\sigma,\varphi) = A_0\sigma^2 + B_0\sigma^4 + C\sigma^6 - h\sigma + \gamma\sigma^2\varphi + \frac{1}{2}\varphi^2 - h\sigma - j\varphi, \tag{2.39}$$

where the term $\gamma\sigma^2\varphi$ represents the coupling between σ and φ, and j is the external field for φ. We note that Eq. (2.39) returns to Eq. (2.28) by using the extreme value condition $\partial f(\sigma,\varphi)/\partial\varphi$ to eliminate φ and setting $A = A_0 + \gamma j$ and $B = B_0 - \gamma^2/2$.

Analysis of dynamic properties at Z_2-CP

Let us discuss the dynamics of fluctuations at the Z_2-CP through the TDGL-like analysis. For that, in order to consider the inhomogeneous system, we add the term $\kappa(\nabla\sigma)^2/2$ to Eq. (2.39) as in the previous section. Moreover, we assume a simple equation of motion for σ and φ as follows

$$L_\sigma(\partial_t)\sigma = -\frac{\delta\Omega}{\delta\sigma}, \tag{2.40}$$

$$L_\sigma(\partial_t)\varphi = -\frac{\delta\Omega}{\delta\varphi}, \tag{2.41}$$

where $L_\sigma(\partial_t)$ and $L_\varphi(\partial_t)$ are time-differential operators. Although the forms of $L_\sigma(\partial_t)$ and $L_\varphi(\partial_t)$ are unknown, a phenomenological restriction can be imposed for the form of the latter. Since φ is the field corresponding to the linear combination of conserved quantity densities, the dispersion relation of its fluctuations should possess zero energy in the long wavelength limit. From this, we will use the form $L_\sigma(\partial_\varphi)\varphi = -\partial_t/\lambda\boldsymbol{q}^2$ with a positive λ, which describes the diffusion property. On the other hand, for the former, we take the form of $L_\sigma(\partial_t) = \partial_t^2/\Gamma$ with a positive Γ, taking into account the dispersion relation of modes such as sigma mesons.

Assuming that the deviations of σ and φ are small, i.e. $\sigma = \sigma_0 + \delta\sigma$ and $\sigma = \varphi_0 + \delta\varphi$ with small $\delta\sigma$ and $\delta\varphi$, and linearizing Eqs. (2.40) and (2.41), we obtain the linearized equation

$$\begin{pmatrix} L_\sigma(\partial_t) + \Omega_{\sigma\sigma} & \Omega_{\sigma\varphi} \\ \Omega_{\varphi\sigma} & L_\varphi(\partial_t) + \Omega_{\varphi\varphi} \end{pmatrix} \begin{pmatrix} \delta\sigma \\ \delta\varphi \end{pmatrix} = 0. \tag{2.42}$$

where $\Omega_{\sigma\sigma} = \delta^2\Omega/\delta\sigma\delta\sigma|_{\sigma_0}$ and so on. The dispersion relation for the collective modes near Z_2-CP can be obtained by the Fourier transforming of Eq. (2.42) as follows

$$\det \begin{pmatrix} -\omega^2 + \Gamma(\chi_h^{-1} + 4\gamma^2\sigma_0^2 + \kappa\boldsymbol{q}^2) & 2\gamma\sigma_0\sqrt{\Gamma\lambda\boldsymbol{q}^2} \\ 2\gamma\sigma_0\sqrt{\Gamma\lambda\boldsymbol{q}^2} & -i\omega + \lambda\boldsymbol{q}^2 \end{pmatrix} = 0. \tag{2.43}$$

In the long wavelength limit $\boldsymbol{q} \to \boldsymbol{0}$, we obtain the following solutions

$$\omega_d(\boldsymbol{0}) = 0, \quad \omega_o(\boldsymbol{0}) = \pm\sqrt{\Gamma(\chi_h^{-1} + 4\gamma^2\sigma_0^2)}. \tag{2.44}$$

The former solution ω_d has the diffusion-like hydrodynamic character, while the latter ω_o possesses the oscillating character.

Next, we consider the dispersion relation $\omega_d(\boldsymbol{q})$ and $\omega_0(\boldsymbol{q})$ with small $|\boldsymbol{q}|$. When $\omega \simeq 0$, since Eq. (2.43) can be approximated as

$$\det \begin{pmatrix} \Gamma(\chi_h^{-1} + 4\gamma^2\sigma_0^2) & 2\gamma\sigma_0\sqrt{\Gamma\lambda\boldsymbol{q}^2} \\ 2\gamma\sigma_0\sqrt{\Gamma\lambda\boldsymbol{q}^2} & -i\omega + \lambda\boldsymbol{q}^2 \end{pmatrix} = 0, \tag{2.45}$$

we obtain the solution

$$\omega_d(\boldsymbol{q}) = -\frac{i\lambda\boldsymbol{q}^2\chi_h^{-1}}{\chi_h^{-1} + 4\gamma^2\sigma_0^2}. \tag{2.46}$$

On the other hand, when $\omega \simeq \pm\sqrt{\Gamma(\chi_h^{-1} + 4\gamma^2\sigma_0^2)}$, Eq. (2.43) is approximated as follows

$$\det \begin{pmatrix} -\omega^2 + \Gamma(\chi_h^{-1} + 4\gamma^2\sigma_0^2 + \kappa\boldsymbol{q}^2) & 2\gamma\sigma_0\sqrt{\Gamma\lambda\boldsymbol{q}^2} \\ 2\gamma\sigma_0\sqrt{\Gamma\lambda\boldsymbol{q}^2} & \mp i\sqrt{\Gamma(\chi_h^{-1} + 4\gamma^2\sigma_0^2)} \end{pmatrix} = 0, \tag{2.47}$$

and then, the solution is obtained as

$$\omega_{o\pm}(\boldsymbol{q}) = \pm\sqrt{\Gamma(\chi_h^{-1} + 4\gamma^2\sigma_0^2) + \left(\kappa \mp i\frac{4\gamma^2\sigma_0^2}{\sqrt{\Gamma(\chi_h^{-1} + 4\gamma^2\sigma_0^2)}}\right)\boldsymbol{q}^2}. \tag{2.48}$$

From these analyses, we finally find that the hydrodynamic mode is the soft mode of the Z_2-CP or the QCD-CP, while the sigma mode is not. This can be understood as follows. Since $\sigma \neq 0$ but $\chi_h^{-1} \to 0$ as approaching the QCD-CP, ω_d in Eq. (2.46) goes to zero, while ω_o in Eq. (2.48) remains finite. Therefore, the hydrodynamic mode can soften, whereas the sigma mode cannot.

Chapter 3

Finite temperature and density quantum field theory

In this chapter, the finite temperature and density quantum field theory is reviewed on the basis of Refs. [86, 87]. In particular, we describe the imaginary-time formalism and linear response theory.

In this thesis, the grand canonical ensemble is used since particles and antiparticles can be created and destroyed in relativistic quantum systems. Consider the system specified with temperature T and chemical potential μ under this ensemble. Letting the Hamiltonian and number operator be $\hat{H}$ and $\hat{N}$, the statistical density operator of the system is given by

$$\hat{\rho} = \frac{e^{-\hat{K}/T}}{Z}, \tag{3.1}$$

where $\hat{K}$ and Z are the grand canonical Hamiltonian and the partition function

$$\hat{K} = \hat{H} - \mu\hat{N}, \qquad Z = \mathrm{Tr}\,\hat{\rho}. \tag{3.2}$$

The 'hat' symbol denotes an operator and Tr means the trace operation. Using the density matrix $\hat{\rho}$, the ensemble average of an observable represented by the operator $\hat{X}$ is computed by

$$\langle\hat{X}\rangle = \mathrm{Tr}\,\hat{\rho}\hat{X}. \tag{3.3}$$

Throughout this Thesis, the symbol $\langle\cdot\rangle$ is the ensemble average for the given Hamiltonian. Also, the thermodynamic potential is given with the partition function by

$$\Omega = -T\log Z, \tag{3.4}$$

which allows us to calculate the macroscopic equilibrium thermodynamics. For instance, the pressure, particle number, entropy, and energy are written in terms of the potential Ω as

$$P = -\frac{\partial\Omega}{\partial V}, \quad S = -\frac{\partial\Omega}{\partial T}, \quad N = -\frac{\partial\Omega}{\partial\mu}, \quad E = -PV + TS + \mu N, \tag{3.5}$$

where V is the volume of the system.

3.1 Imaginary-time formalism

In this section, we review the imaginary-time formalism, where the imaginary time is introduced as $\tau = it$. Let us consider a system specified with temperature T and chemical potential μ. In this formalism, the field operators are written respectively in the Heisenberg picture by

$$\hat{\psi}_H(\boldsymbol{x},\tau) = e^{+\hat{K}\tau}\hat{\psi}_H(\boldsymbol{x},0)e^{-\hat{K}\tau}, \tag{3.6}$$

where it is noted that the time evolution is given by the grand canonical Hamiltonian $\hat{K}$. The field operator satisfies the following relations

$$[\hat{\psi}_H(\boldsymbol{x},\tau),\hat{\psi}_H^\dagger(\boldsymbol{x}',\tau')]_\mp = \delta(\boldsymbol{x}-\boldsymbol{x}')\delta(\tau-\tau'), \tag{3.7}$$
$$[\hat{\psi}_H(\boldsymbol{x},\tau),\hat{\psi}_H(\boldsymbol{x}',\tau')]_\mp = [\hat{\psi}_H^\dagger(\boldsymbol{x},\tau),\hat{\psi}_H^\dagger(\boldsymbol{x}',\tau')]_\mp = 0, \tag{3.8}$$

where the upper and lower signs denote the commutation and anticommutation relations for bosons and fermions, respectively. Also, the spin degrees of freedom are omitted for simplicity. Then, the single-particle Green's function in this formalism is defined as

$$\mathcal{G}(\boldsymbol{x},\tau;\,\boldsymbol{x}',\tau') = \pm\mathrm{Tr}\,\hat{\rho}T_\tau\big[\hat{\psi}_H(\boldsymbol{x},\tau)\,\hat{\psi}_H^\dagger(\boldsymbol{x}',\tau')\big], \tag{3.9}$$

where T_τ is the imaginary-time ordering operator. In this section, the upper and lower signs such as Eq. (3.8) refer to bosons and fermions, respectively.

Next, we shall show the periodic property of the Green's function. We let $\tau = 0$ for simplicity and assert the condition $0 < \tau' < \beta$ for τ', where $\beta = 1/T$. Then, we can find

$$\begin{aligned}
\mathcal{G}(\boldsymbol{x},0;\,\boldsymbol{x}',\tau') &= \pm\,\mathrm{Tr}\,T_\tau\big[\,\hat{\rho}\,\hat{\psi}_H(\boldsymbol{x},0)\,\hat{\psi}_H^\dagger(\boldsymbol{x}',\tau')\big] \\
&= \pm\,Z^{-1}\,\mathrm{Tr}\,\big[e^{-\beta\hat{K}}\,\hat{\psi}_H^\dagger(\boldsymbol{x}',\tau')\,\hat{\psi}_H(\boldsymbol{x},0)\big] \\
&= \mp\,Z^{-1}\,\mathrm{Tr}\,\big[\hat{\psi}_H(\boldsymbol{x},0)\,e^{-\beta\hat{K}}\,\hat{\psi}_H^\dagger(\boldsymbol{x}',\tau')\big] \\
&= \mp\,Z^{-1}\,\mathrm{Tr}\,\big[e^{-\beta\hat{K}}\,\hat{\psi}_H(\boldsymbol{x},\beta)\,\hat{\psi}_H^\dagger(\boldsymbol{x}',\tau')\big] \\
&= \pm\,\mathcal{G}(\boldsymbol{x},\beta;\,\boldsymbol{x}',\tau'),
\end{aligned} \tag{3.10}$$

where Eq. (3.8) is used in the first equality and the cyclic property of the trace is used in the second equality. Eq. (3.10) means that the Green's function of bosons and fermions are periodic and antiperiodic for τ, respectively, whose period is β. The periodicity and antiperiodicity of $\mathcal{G}(\boldsymbol{x},\tau;\,\boldsymbol{x}',\tau')$ discretize the frequencies of bosons and fermions. For simplicity, we assume the translational system along τ, where the Green's function depends only on $\bar{\tau} = \tau - \tau'$ as follows

$$\mathcal{G}(\boldsymbol{x},\tau;\,\boldsymbol{x}',\tau') = \mathcal{G}(\boldsymbol{x},\boldsymbol{x}',\bar{\tau}). \tag{3.11}$$

Since $\mathcal{G}(\boldsymbol{x},\boldsymbol{x}',\bar{\tau})$ of both statistics is periodic over 2β, it can be expanded in the Fourier series

$$\mathcal{G}(\boldsymbol{x},\boldsymbol{x}',\bar{\tau}) = \frac{1}{\beta}\sum_n e^{-i\omega_n\bar{\tau}}\mathcal{G}(\boldsymbol{x},\boldsymbol{x}',i\omega_n), \tag{3.12}$$
$$\mathcal{G}(\boldsymbol{x},\boldsymbol{x}',i\omega_n) = \frac{1}{2}\int_{-\beta}^{+\beta} d\bar{\tau}\; e^{-i\omega_n\bar{\tau}}\mathcal{G}(\boldsymbol{x},\boldsymbol{x}',\bar{\tau}), \tag{3.13}$$

where $\omega_n = n\pi/\beta$ with integer n. From this, it is confirmed that the frequencies are discretized by the periodicity or antiperiodicity. The Fourier coefficient $\mathcal{G}(\boldsymbol{x},\boldsymbol{x}',i\omega_n)$ can be deformed as follows

$$\mathcal{G}(\boldsymbol{x},\boldsymbol{x}',i\omega_n) = \frac{1\pm e^{-i\omega_n\beta}}{2}\int_0^\beta d\bar{\tau}\; e^{-i\omega_n\bar{\tau}}\mathcal{G}(\boldsymbol{x},\boldsymbol{x}',\bar{\tau}), \tag{3.14}$$

Since $e^{-i\omega_n\beta} = (-1)^n$, the factor $(1\pm e^{-i\omega_n\beta})/2$ in Eq. (3.14) is

$$\begin{aligned}
\frac{1+e^{-i\omega_n\beta}}{2} &= \begin{cases} 1 & n \text{ is even} \\ 0 & n \text{ is odd} \end{cases} \quad \text{for boson,} \\
\frac{1-e^{-i\omega_n\beta}}{2} &= \begin{cases} 0 & n \text{ is even} \\ 1 & n \text{ is odd} \end{cases} \quad \text{for fermion,}
\end{aligned} \tag{3.15}$$

and therefore, $\mathcal{G}(\boldsymbol{x}, \boldsymbol{x}', i\omega_m)$ is

$$\mathcal{G}(\boldsymbol{x}, \boldsymbol{x}', i\omega_m) = \int_0^\beta d\bar{\tau}\, e^{-i\omega_m \bar{\tau}} \mathcal{G}(\boldsymbol{x}, \boldsymbol{x}', \bar{\tau}), \tag{3.16}$$

$$\omega_m = \begin{cases} 2m\pi T & \text{for boson,} \\ 2(m+1)\pi T & \text{for fermion,} \end{cases} \tag{3.17}$$

where m is an integer. The difference between the discretized frequency of bosons and fermions is given by Eq. (3.17), and ω_m is often referred to as the Matsubara frequency.

It is worthwhile to note the relation between the imaginary-time formalism and real-time formalism. In the real-time formalism, the Green's function is defined as

$$G(\boldsymbol{x}, t;\ \boldsymbol{x}', t') = -i\ \mathrm{Tr}\ \hat{\rho} T\big[\hat{\psi}_H(\boldsymbol{x}, t)\ \hat{\psi}_H^\dagger(\boldsymbol{x}', t')\big], \tag{3.18}$$

where it is noted that the symbol T is the 'time' ordering operator. Also, the retarded and advanced Green's functions are given by

$$G^R(\boldsymbol{x}, t;\ \boldsymbol{x}', t') = -i\ \mathrm{Tr}\ \hat{\rho}\big[\hat{\psi}_H(\boldsymbol{x}, t),\ \hat{\psi}_H^\dagger(\boldsymbol{x}', t')\big]_\mp\, \theta(t - t'), \tag{3.19}$$

$$G^A(\boldsymbol{x}, t;\ \boldsymbol{x}', t') = +i\ \mathrm{Tr}\ \hat{\rho}\big[\hat{\psi}_H(\boldsymbol{x}, t),\ \hat{\psi}_H^\dagger(\boldsymbol{x}', t')\big]_\mp\, \theta(t - t'). \tag{3.20}$$

Considering the homogeneous system and assuming the Green's functions depend on $\boldsymbol{x} - \boldsymbol{x}'$ and $t - t'$, in the Fourier space, G^R and G^A are connected to $\mathcal{G}$ through the analytic continuation

$$G^R(\boldsymbol{k}, \omega) = \mathcal{G}(\boldsymbol{k}, i\omega_m \to \omega + i\eta), \tag{3.21}$$

$$G^A(\boldsymbol{k}, \omega) = \mathcal{G}(\boldsymbol{k}, i\omega_m \to \omega - i\eta), \tag{3.22}$$

where ω is a real number (energy) and η is a positive infinitesimal real number. This fact can be checked explicitly by the analysis of the Lehmann representation. Thereby, we can calculate the retarded Green's function as well as the advanced one through the use of the imaginary-time formalism and the proper analytic continuation.

Before this section is closed, we give the useful techniques for the summation of the Matsubara frequency as the summation often occurs in the calculations within the imaginary time formalism. Here, let the Matsubara frequencies for the bosons and fermions be denoted by $\omega_m = 2\pi m T$ and $\nu_m = 2\pi(m+1)T$, respectively, to distinguish them. These notations ω_m and ν_m are also employed in the next chapters. Consider the summations of $f(i\omega_m)$ and $g(i\nu_m)$ for m, where $f(p_0)$ and $g(p_0)$ are functions of a complex number p_0. It is assumed that $f(p_0)$ and $g(p_0)$ go to zero as $|p_0| \to \infty$. Noting that the poles of $\coth(p_0/2T)$ and $\tanh(p_0/2T)$ are existing at $\omega_m = 2i\pi m T$ and $\nu_m = 2i\pi(m+1)T$, respectively, the summations can be rewritten by the residue integrals as follows

$$T \sum_{m=-\infty}^{\infty} f(i\omega_m) = \frac{1}{2\pi i} \oint_C dp_0\, f(p_0)\, \frac{\coth(p_0/2T)}{2}, \tag{3.23}$$

$$T \sum_{m=-\infty}^{\infty} g(i\nu_m) = \frac{1}{2\pi i} \oint_C dp_0\, g(p_0)\, \frac{\tanh(p_0/2T)}{2}, \tag{3.24}$$

where the contour C can be taken as desired to simplify the calculation, as long as it encloses all the residues of the integrand function (when $f(p_0)$ or $g(p_0)$ have branch cuts, C has to avoid the cuts).

3.2 Linear response theory

In this section, we consider a system in which a weak external field is applied and calculate the change in the ensemble average of any operator caused by the external field. The goal of this section is to derive the formula of the response function that we utilize in the thesis.

First of all, let the grand canonical Hamiltonian of such a system in the Schrödinger picture be

$$\hat{K}_{\mathrm{tot},S} = \hat{H}_{0,S} + \hat{H}_{\mathrm{ex},S} - \mu\hat{N}, \tag{3.25}$$

where $\hat{H}_{0,S}$ and $\hat{H}_{\mathrm{ex},S}$ are the unperturbed Hamiltonian and the external field that couple to the system, respectively, which are assumed to be Hermitian for simplicity. To suppose the system had achieved equilibrium in the past, we assume that $\hat{H}_{\mathrm{ex},S}$ vanishes when $t < t_0$. When $t > t_0$, the equation of motion for the eigenstate $|j(\boldsymbol{x},t)\rangle_S$ is

$$i\frac{d}{dt}|j(\boldsymbol{x},t)\rangle_S = \hat{K}_{\mathrm{tot},S}|j(\boldsymbol{x},t)\rangle_S. \tag{3.26}$$

The subscript of 'S' denotes the Schrödinger picture, and an operator $\hat{O}_S(\boldsymbol{x})$ is time-independent.

Here, let us introduce the interaction picture for Eq. (3.25) in order to solve Eq. (3.26) perturbatively for $\hat{H}_{\mathrm{ex}}$. The subscript of 'I' denotes the interaction picture. In this picture, a state and an operator that correspond to $|j(\boldsymbol{x},t)\rangle_S$ and $\hat{O}_S(\boldsymbol{x})$ are, respectively,

$$|j(\boldsymbol{x},t)\rangle_I = e^{i\hat{K}_{0,S}t}|j(\boldsymbol{x},t)\rangle_S, \tag{3.27}$$

$$\hat{O}_I(\boldsymbol{x},t) = e^{+i\hat{K}_{0,S}t}\hat{O}_S e^{-i\hat{K}_{0,S}t}, \tag{3.28}$$

where $\hat{K}_{0,S} = \hat{H}_{0,S} - \mu\hat{N}$, and their time evolution is given by

$$i\frac{\partial}{dt}|j(\boldsymbol{x},t)\rangle_I = \hat{H}_{\mathrm{ex},I}(t)|j(\boldsymbol{x},t)\rangle_I \tag{3.29}$$

$$i\frac{\partial}{dt}\hat{O}_I(\boldsymbol{x},t) = [\hat{O}_I(\boldsymbol{x},t), \hat{H}_{0,S}] \tag{3.30}$$

with $\hat{H}_{\mathrm{ex},I}(t) = e^{i\hat{H}_{0,S}t}\hat{H}_{\mathrm{ex},S}e^{-i\hat{H}_{0,S}t}$. From Eq. (3.29), $|j(\boldsymbol{x},t)\rangle_I$ is represented in terms of $|j(\boldsymbol{x},t_0)\rangle_I$ as

$$|j(\boldsymbol{x},t)\rangle_I = U(t,t_0)|j(\boldsymbol{x},t_0)\rangle_I, \tag{3.31}$$

$$U(t,t_0) = e^{i\hat{K}_{0,S}t}e^{-i\hat{H}_{\mathrm{tot},S}(t-t_0)}e^{-i\hat{K}_{0,S}t}. \tag{3.32}$$

Since Eq. (3.32) is not useful for computation, we give the following formula

$$\hat{U}(t,t_0) = 1 + \frac{1}{i}\int_{t_0}^{t} dt'\hat{H}_{\mathrm{ex},I}(t') + \frac{1}{i^2}\int_{t_0}^{t}\int_{t_0}^{t'} dt'dt''\hat{H}_{\mathrm{ex},I}(t')\hat{H}_{\mathrm{ex},I}(t'') + \cdots. \tag{3.33}$$

This formula is obtained by solving the following differential equation iteratively

$$i\frac{d}{dt}U(t,t_0) = \hat{H}_{\mathrm{ex},I}(t)U(t,t_0), \tag{3.34}$$

which is derived from Eqs. (3.30) and (3.31).

Next, we calculate the expectation value ${}_S\langle j(\boldsymbol{x},t)|\hat{O}_S(\boldsymbol{x})|j(\boldsymbol{x},t)\rangle_S$ and its change by the external field. From Eq. (3.27) and (3.31),

$$\begin{aligned}{}_S\langle j(\boldsymbol{x},t)|\hat{O}_S(\boldsymbol{x})|j(\boldsymbol{x},t)\rangle_S &= {}_I\langle j(\boldsymbol{x},t_0)|U^\dagger(t,t_0)e^{i\hat{K}_{0,S}t}\hat{O}_S(\boldsymbol{x})e^{-i\hat{K}_{0,S}t}U(t,t_0)|j(\boldsymbol{x},t_0)\rangle_I \\ &= {}_I\langle j(\boldsymbol{x},t_0)|U^\dagger(t,t_0)\hat{O}_I(\boldsymbol{x},t)U(t,t_0)|j(\boldsymbol{x},t_0)\rangle_I.\end{aligned} \tag{3.35}$$

Substituting Eq. (3.33) to Eq. (3.35) and considering up to the first order of $\hat{H}_{\mathrm{ex},I}(t)$, we obtain

$$\begin{aligned}\delta\langle j(\boldsymbol{x},t)|\hat{O}|j(\boldsymbol{x},t)\rangle &= {}_S\langle j(\boldsymbol{x},t)|\hat{O}_S(\boldsymbol{x})|j(\boldsymbol{x},t)\rangle_S - {}_I\langle j(\boldsymbol{x},t_0)|\hat{O}_I(\boldsymbol{x},t)|j(\boldsymbol{x},t_0)\rangle_I \\ &= -i\int_{t_0}^{t} dt'\,{}_I\langle j(\boldsymbol{x},t_0)|[\hat{O}_I(\boldsymbol{x},t), \hat{H}_{\mathrm{ex},I}(t')]|j(\boldsymbol{x},t_0)\rangle_I.\end{aligned} \tag{3.36}$$

Then, the change of the ensemble average caused by the external field is

$$\delta\langle\hat{O}(\boldsymbol{x},t)\rangle = \frac{\sum_j e^{-K_j/T}\delta\langle j(\boldsymbol{x},t)|\hat{O}|j(\boldsymbol{x},t)\rangle}{\sum_j e^{-K_j/T}} = -i\int_{t_0}^{t} dt'\ \mathrm{Tr}\ \hat{\rho}[\hat{O}_I(\boldsymbol{x},t),\hat{H}_{\mathrm{ex},I}(t')], \tag{3.37}$$

where K_j is the eigenvalue of $K_{0,S}$ for $|j(\boldsymbol{x},t_0)\rangle_S$. This formula is valid as long as the external field $\hat{H}_{\mathrm{ex,S}}$ is enough weak, which is why it is called the linear response theory. Finally, we derive the formula of the response function. Let the external field in the interaction picture be given by

$$\hat{H}_{\mathrm{ex},I}(t') = \int d^3x' J(\boldsymbol{x}',t')\hat{O}_I(\boldsymbol{x}',t'). \tag{3.38}$$

Substituting Eq. (3.38) into Eq. (3.39), the change is

$$\begin{aligned}\delta\langle\hat{O}(\boldsymbol{x},t)\rangle &= -i\int_{t_0}^{t} dt' \int d^3x' J(\boldsymbol{x}',t')\ \mathrm{Tr}\ \hat{\rho}[\hat{O}_I(\boldsymbol{x},t),\hat{O}_I(\boldsymbol{x}',t')] \\ &= -i\int_{t_0}^{t} dt' \int d^3x J(\boldsymbol{x}',t')\ \mathrm{Tr}\ \hat{\rho}[\hat{O}_I(\boldsymbol{x},t),\hat{O}_I(\boldsymbol{x}',t')]\theta(t-t').\end{aligned} \tag{3.39}$$

Here, introducing the following quantities would be useful

- the retarded Green's function :

$$D^R(\boldsymbol{x},t;\boldsymbol{x}',t') = -\,i\ \mathrm{Tr}\ \hat{\rho}\ [\hat{O}_I(\boldsymbol{x},t),\hat{O}_I(\boldsymbol{x}',t')]\theta(t-t') \tag{3.40}$$

- the advanced Green's function :

$$D^A(\boldsymbol{x},t;\boldsymbol{x}',t') = +\,i\ \mathrm{Tr}\ \hat{\rho}\ [\hat{O}_I(\boldsymbol{x},t),\hat{O}_I(\boldsymbol{x}',t')]\theta(t'-t) \tag{3.41}$$

- the time-ordered propagator (imaginary-time Green's functions) :

$$\mathcal{D}(\boldsymbol{x},\tau;\boldsymbol{x}',\tau') = -i\ \mathrm{Tr}\ \hat{\rho}\ T_\tau\big(\hat{O}_I(\boldsymbol{x},\tau)\hat{O}_I(\boldsymbol{x}',\tau')\big) \tag{3.42}$$

where it is noted that the retarded and advanced Green's functions are defined in the real time, while the time-ordered propagator is done in the imaginary time. Using the retarded function (3.40), the change (3.39) is written

$$\delta\langle\hat{O}(\boldsymbol{x},t)\rangle = \int_{-\infty}^{+\infty} dt' \int d^3x J(\boldsymbol{x}',t')D^R(\boldsymbol{x},t;\boldsymbol{x}',t'), \tag{3.43}$$

where we have taken $t_0 \to -\infty$ and $t \to +\infty$ in the upper and lower limits of the integration on account of the retarded function.

Since the unperturbed system is in thermal equilibrium, $D^R(\boldsymbol{x},t;\boldsymbol{x}',t')$ depends only on $\boldsymbol{x}-\boldsymbol{x}'$ and $t-t'$ except for systems of a solid, crystal and so on. Using the Fourier transformations

$$D^R(\boldsymbol{x},t;\boldsymbol{x}',t') = \int \frac{d^3k d\omega}{(2\pi)^4} e^{i\boldsymbol{k}\cdot(\boldsymbol{x}-\boldsymbol{x}')-i\omega(t-t')}D^R(\boldsymbol{k},\omega), \tag{3.44}$$

$$J(\boldsymbol{x}',t') = \int \frac{d^3k d\omega}{(2\pi)^4} e^{i\boldsymbol{k}\cdot\boldsymbol{x}'-i\omega t'}J(\boldsymbol{k},\omega), \tag{3.45}$$

we obtain the Fourier expression of Eq. (3.39) as follows

$$\delta\langle\hat{O}(\boldsymbol{k},\omega)\rangle = J(\boldsymbol{k},\omega)D^R(\boldsymbol{k},\omega). \tag{3.46}$$

This is the general formulation of the linear response theory, which is called the Kubo formula. Since $\delta\langle\hat{O}(\boldsymbol{k},\omega)\rangle$ means the change caused by the external source $J(\boldsymbol{k},\omega)$, the retarded Green's function $D^R(\boldsymbol{k},\omega)$ can be regarded as the response function for the operator $\hat{O}$ in Eq. (3.46).

In Chap. 5.3, we calculate the response function for the diquark condensate and chiral condensate to examine the 2SC-PT and QCD-CP soft modes. In the calculations, it is beneficial to notice the relations between Eqs. (3.40), (3.41), and (3.42) in the Fourier space. Their relations are the following analytic continuation

$$D^R(\boldsymbol{k},\omega) = \mathcal{D}(\boldsymbol{k},i\nu_n)|_{i\nu_n\to\omega+i\eta}, \tag{3.47}$$

$$D^A(\boldsymbol{k},\omega) = \mathcal{D}(\boldsymbol{k},i\nu_n)|_{i\nu_n\to\omega-i\eta}, \tag{3.48}$$

where η is a positive infinitesimal number.

Chapter 4

Nambu–Jona–Lasinio model

To describe the phase transitions in dense quark matter and their effects on the dilepton production and the transport coefficients, we employ the 2-flavor Nambu–Jona–Lasinio (NJL) model [88, 89]

$$\mathcal{L}_{\rm NJL} = \bar{\psi} i(\partial\!\!\!/ - m)\psi + \mathcal{L}_S + \mathcal{L}_D, \tag{4.1}$$

$$\mathcal{L}_S = G_S[(\bar{\psi}\psi)^2 + (\bar{\psi} i\gamma_5 \boldsymbol{\tau}\psi)^2], \tag{4.2}$$

$$\mathcal{L}_D = G_D(\bar{\psi} i\gamma_5\tau_2\lambda_A\psi^C)(\bar{\psi}^C i\gamma_5\tau_2\lambda_A\psi), \tag{4.3}$$

where $\psi = \psi(x)$ and $\bar{\psi} = \psi^\dagger\gamma_0$ are the quark and antiquark fields, respectively, and $\psi^C(x) = i\gamma_2\gamma_0\bar{\psi}^T(x)$. Eqs. (4.2) and (4.3) represent the quark–antiquark and quark–quark interactions, respectively, where $\boldsymbol{\tau} = (\tau_1, \tau_2, \tau_3)$ is the Pauli matrix for the flavor $SU(2)_f$ and λ_A $(A = 2, 5, 7)$ are the antisymmetric components of the Gell-mann matrices for the color $SU(3)_c$. In our work, it is assumed that the up and down quarks take the same value of the current quark mass $m = m_u = m_d$ for simplicity. The scalar coupling constant $G_S = 5.50$ GeV^{-2} and the three-momentum cutoff $\Lambda = 631$ MeV are determined so as to reproduce the pion mass $m_\pi = 138$ MeV and the pion decay constant $f_\pi = 93$ MeV at $m = 5.5$ MeV [88]. The detail of this cutoff scheme is described in Appendix A. Since there are various estimates of the diquark coupling G_D [89], we treat it as a free parameter and vary within the interval $G_D/G_S = 0.6$–0.7.

In this chapter, we first evaluate the ground state of the system by the mean-field approximation (MFA), which is explained in Sec. 4.1. In Sec. 4.2, we will show the phase diagram in the MFA, where the phase transitions to the chiral symmetry breaking (CSB), the QCD-CP and two-flavor color superconducting (2SC) phases manifest themselves.

4.1 Thermodynamic potential in the MFA

In this section, we calculate the thermodynamic potential in the MFA to compute the phase transitions to the CSB and 2SC phases. We assume the nonzero chiral condensate $\langle\bar{\psi}\psi\rangle$ and diquark condensate $\langle\bar{\psi}^C i\gamma_5\tau_2\lambda_A\psi\rangle$. Their values for a given set of the temperature T and quark chemical potential μ are determined by minimizing the thermodynamic potential as described in Chap. 3. The Hamiltonian density $\mathcal{H}$ is given with the Lagrangian density $\mathcal{L}$ as $\mathcal{H} = \bar{\psi} i\gamma_0\partial^0\psi - \mathcal{L}$. In the MFA, the Lagrangian density (4.1) is given by

$$\mathcal{L}_{\rm MFA} = \bar{\psi} i(\partial\!\!\!/ - m)\psi - M_D\bar{\psi}\psi - \frac{1}{2}(\Delta^\dagger\bar{\psi}^C i\gamma_5\tau_2\lambda_2\psi + \text{h.c.}) - \frac{M_D^2}{4G_S} - \frac{|\Delta|^2}{4G_D}, \tag{4.4}$$

where $M_D = -2G_S\langle\bar{\psi}\psi\rangle$ and $\Delta = -2G_D\langle\bar{\psi}^C i\gamma_5\tau_2\lambda_A\psi\rangle$ are the dynamically generated quark mass and the diquark gap. Then, the grand canonical Hamiltonian in the MFA is given by

$$K_{MFA} = -\int d^3x\left[\bar{\psi}(i\boldsymbol{\gamma}\cdot\boldsymbol{\nabla} - M)\psi + \bar{\psi}\mu\gamma_0\psi - \frac{1}{2}(\Delta^\dagger\bar{\psi}^C i\gamma_5\tau_2\lambda_2\psi + \text{h.c.}) - \frac{M_D^2}{4G_S} - \frac{|\Delta|^2}{4G_D}\right], \tag{4.5}$$

where $M = m + M_D$ is the total quark mass.

To calculate Eq. (4.5), we consider the plane wave expansion

$$\psi = \psi(x) = \int \frac{d^3p}{(2\pi)^3}\frac{1}{\sqrt{2E_p}}\sum_{s=\pm}\left[a_M(\boldsymbol{p},s)u_M(\boldsymbol{p},s)e^{-ip\cdot x} + b_M^\dagger(\boldsymbol{p},s)v_M(\boldsymbol{p},s)e^{+ip\cdot x}\right], \tag{4.6}$$

where $p = (\boldsymbol{p}, p_0)$ and $E_p = \sqrt{\boldsymbol{p}^2 + M^2}$. Also, a_M and b_M are the expansion coefficients. In this expansion, the spinors of the particle $u_M(\boldsymbol{p},s)$ and of the antiparticle $v_M(\boldsymbol{p},s)$ are the solutions of the Dirac equation

$$(\not{p} - M)u_M(\boldsymbol{p},s) = 0, \tag{4.7}$$
$$(\not{p} + M)v_M(\boldsymbol{p},s) = 0, \tag{4.8}$$

in which their spinors are taken so as to satisfy the following orthogonality

$$u_M^\dagger(\boldsymbol{p},s)u_M(\boldsymbol{p},t) = v_M^\dagger(\boldsymbol{p},s)v_M(\boldsymbol{p},t) = 2E_p\delta_{st}, \tag{4.9}$$
$$\bar{u}_M(\boldsymbol{p},s)u_M(\boldsymbol{p},t) = \bar{v}_M(\boldsymbol{p},s)v_M(\boldsymbol{p},t) = 2M\delta_{st}, \tag{4.10}$$
$$u_M^\dagger(\boldsymbol{p},s)v_M(\boldsymbol{p},t) = v_M^\dagger(\boldsymbol{p},s)u_M(\boldsymbol{p},t) = 0, \tag{4.11}$$
$$\bar{u}_M(\boldsymbol{p},s)v_M(\boldsymbol{p},t) = \bar{v}_M(\boldsymbol{p},s)u_M(\boldsymbol{p},t) = 0. \tag{4.12}$$

Then, substituting Eq. (4.6) to Eq. (4.5) and using the relations (4.9)–(4.12), the Hamiltonian $K_{\rm MFA}$ is written in terms of a_M and b_M as

$$\begin{aligned}
K_{\rm MFA} = {} & N_fN_c\sum_{s=\pm}\int\frac{d^3p}{(2\pi)^3}E_p\left[a_M^\dagger(\boldsymbol{p},s)a_M(\boldsymbol{p},s) - b_M^\dagger(\boldsymbol{p},s)b_M(\boldsymbol{p},s)\right] \\
& -N_fN_c\sum_{s=\pm}\int\frac{d^3p}{(2\pi)^3}\,\mu\left[a_M^\dagger(\boldsymbol{p},s)a_M(\boldsymbol{p},s) + b_M^\dagger(\boldsymbol{p},s)b_M(\boldsymbol{p},s)\right] \\
& +\frac{1}{2}\sum_{s=\pm}s\int\frac{d^3p}{(2\pi)^3}\Big\{a_M^\dagger(\boldsymbol{p},s)\tilde{\Delta}^\dagger a_M^\dagger(-\boldsymbol{p},-s) - b_M(-\boldsymbol{p},-s)\tilde{\Delta}^\dagger b_M(\boldsymbol{p},s) \\
& \quad +a_M(\boldsymbol{p},s)\tilde{\Delta}a_M(-\boldsymbol{p},-s) - b_M^\dagger(-\boldsymbol{p},-s)\tilde{\Delta}b_M^\dagger(\boldsymbol{p},s)\Big\} + V\left[\frac{M_D^2}{4G_S} + \frac{|\Delta|^2}{4G_D}\right],
\end{aligned} \tag{4.13}$$

where $N_f = 2$ and $N_c = 3$ are the numbers of the flavor and color, respectively, and $V = \int d^3x$ is the volume of the system. At the third term in the bracket of Eq. (4.13), we introduce $\tilde{\Delta} = i\tau_2\lambda_2\Delta$ for later convenience. Moreover, by noting the following deformation

$$\sum_{s=\pm}\int\frac{d^3p}{(2\pi)^3}a_M^\dagger(\boldsymbol{p},s)a_M(\boldsymbol{p},s) = \frac{1}{2}\sum_{s=\pm}\int\frac{d^3p}{(2\pi)^3}\Big(a_M^\dagger(\boldsymbol{p},s)a_M(\boldsymbol{p},s) + a_M^\dagger(-\boldsymbol{p},-s)a_M(-\boldsymbol{p},-s)\Big),$$

Eq. (4.13) can be simplified as follows

$$K_{\rm MFA} = \frac{1}{2}\sum_{s=\pm}\int\frac{d^3p}{(2\pi)^3}\left[A_M^TO_-A_M + B_M^TO_+B_M\right] + V\left[\frac{M_D^2}{4G_S} + \frac{|\Delta|^2}{4G_D}\right], \tag{4.14}$$

$$A_M = \begin{pmatrix} a_M^\dagger(\boldsymbol{p},s) \\ a_M(-\boldsymbol{p},-s)\end{pmatrix},\quad O_- = \begin{pmatrix} +\xi_-I & -\tilde{\Delta}^\dagger \\ -\tilde{\Delta} & -\xi_-I\end{pmatrix}, \tag{4.15}$$

$$B_M = \begin{pmatrix} b_M^\dagger(\boldsymbol{p},s) \\ b_M(-\boldsymbol{p},-s)\end{pmatrix},\quad O_+ = \begin{pmatrix} +\xi_+I & +\tilde{\Delta}^\dagger \\ +\tilde{\Delta} & -\xi_+I\end{pmatrix}, \tag{4.16}$$

where $\xi_\mp = E_p \mp \mu$, and I is the identity matrix of the $SU(2)_f \times SU(3)_c$. In fact, since a_M and b_M have six components due to $N_f \times N_c$, the matrices $O_\mp$ in Eqs. (4.15) and (4.16) have 12×12

components and their explicit forms are

$$O_{\mp} = \begin{pmatrix} +\xi_{\mp}\delta_{ij}\delta_{\alpha\beta} & \mp\tilde{\Delta}^{\dagger}_{i\alpha,j\beta} \\ \mp\tilde{\Delta}_{i\alpha,j\beta} & -\xi_{\mp}\delta_{ij}\delta_{\alpha\beta} \end{pmatrix}, \tag{4.17}$$

where $\tilde{\Delta}_{i\alpha,j\beta} = i(\tau_2)_{ij}(\lambda_2)_{\alpha\beta}\Delta = -i\epsilon_{ij}\epsilon_{\alpha\beta 3}\Delta$ ($i,\ j = 1,2$ and $\alpha,\ \beta = 1,2$) with the completely antisymmetric tensor ϵ. These matrices are diagonalizable and their twelve eigenvalues are

$$+\xi_-(\times 2),\ -\xi_-(\times 2),\ +\epsilon_-(\times 4),\ -\epsilon_-(\times 4) \quad \text{for} \quad O_-\,, \tag{4.18}$$
$$+\xi_+(\times 2),\ -\xi_+(\times 2),\ +\epsilon_+(\times 4),\ -\epsilon_+(\times 4) \quad \text{for} \quad O_+\,, \tag{4.19}$$

where $\epsilon_{\pm} = \sqrt{\xi_{\pm}^2 + |\Delta|^2}$. In the 2SC phase, out of the three colors, the two components form the Cooper pair. The number of the eigenvalues in Eqs. (4.18) and (4.19) reflect this fact. The diagonalization of the matrices (4.17) is the same as the Bogoliubov transformation, which has been introduced in the BCS theory. We note that the transformation is manipulated for the $SU(2)_c$ due to the two colors that form the pair. Defining the coefficients derived by the Bogoliubov transformation as $\alpha(\boldsymbol{p},s)$ and $\beta(\boldsymbol{p},s)$, $K_{\rm MFA}$ is rewritten as

$$\begin{aligned} K_{\rm MFA} &= 2\sum_{s=\pm}\int\frac{d^3p}{(2\pi)^3}\Big[\xi_- a_M^{\dagger}(\boldsymbol{p},s)a_M(\boldsymbol{p},s) - \xi_+ b_M(\boldsymbol{p},s)b_M^{\dagger}(\boldsymbol{p},s) \\ &\quad + \begin{pmatrix}\alpha^{\dagger}(\boldsymbol{p},s) & \alpha(-\boldsymbol{p},-s)\end{pmatrix}\begin{pmatrix}+\epsilon_- & 0\\ 0 & -\epsilon_-\end{pmatrix}\begin{pmatrix}\alpha^{\dagger}(\boldsymbol{p},s)\\ \alpha(-\boldsymbol{p},-s)\end{pmatrix} \\ &\quad + \begin{pmatrix}\beta^{\dagger}(\boldsymbol{p},s) & \beta(-\boldsymbol{p},-s)\end{pmatrix}\begin{pmatrix}+\epsilon_+ & 0\\ 0 & -\epsilon_+\end{pmatrix}\begin{pmatrix}\beta^{\dagger}(\boldsymbol{p},s)\\ \beta(-\boldsymbol{p},-s)\end{pmatrix}\Big] + V\left[\frac{M_D^2}{4G_S} + \frac{|\Delta|^2}{4G_D}\right] \qquad (4.20) \\ &= 2\sum_{s=\pm}\int\frac{d^3p}{(2\pi)^3}\Big[\xi_- a_M^{\dagger}(\boldsymbol{p},s)a_M(\boldsymbol{p},s) - \xi_+ b_M(\boldsymbol{p},s)b_M^{\dagger}(\boldsymbol{p},s) \\ &\quad + \epsilon_-\Big(\alpha^{\dagger}(\boldsymbol{p},s)\alpha(-\boldsymbol{p},-s) - \alpha(\boldsymbol{p},s)\alpha^{\dagger}(-\boldsymbol{p},-s)\Big) \\ &\quad + \epsilon_-\Big(\beta^{\dagger}(\boldsymbol{p},s)\beta(-\boldsymbol{p},-s) - \beta(\boldsymbol{p},s)\beta^{\dagger}(-\boldsymbol{p},-s)\Big)\Big] + V\left[\frac{M_D^2}{4G_S} + \frac{|\Delta|^2}{4G_D}\right]. \qquad (4.21) \end{aligned}$$

where the second and third lines correspond to the quasi-particles forming the Cooper pair, while the first line is the unpaired one. One finds that ξ_- (ξ_+) is the energy of the particle (antiparticle) and $\epsilon_{\pm}$ is the energy of the quasi-particles.

Next, we quantize $K_{\rm MFA}$ to calculate the thermodynamic potential. We promote the expansion coefficients $a_M(\boldsymbol{p},s)$ and $b_M^{\dagger}(\boldsymbol{p},s)$ to the annihilation operator of the particle $\hat{a}_M(\boldsymbol{p},s)$ and the creation operator of the antiparticle $\hat{b}_M^{\dagger}(\boldsymbol{p},s)$. Since the Dirac particle is the Fermi particle, these operators satisfy the canonical anticommutation relations

$$\{\hat{a}_M(\boldsymbol{p},s),\hat{a}_M^{\dagger}(\boldsymbol{q},t)\} = \{\hat{b}_M(\boldsymbol{p},s),\hat{b}_M^{\dagger}(\boldsymbol{q},t)\} = \delta(\boldsymbol{p}-\boldsymbol{q})\delta_{st}, \tag{4.22}$$
$$\{\hat{a}_M(\boldsymbol{p},s),\hat{a}_M(\boldsymbol{q},t)\} = \{\hat{b}_M(\boldsymbol{p},s),\hat{b}_M(\boldsymbol{q},t)\} = 0, \tag{4.23}$$
$$\{\hat{a}_M(\boldsymbol{p},s),\hat{b}_M(\boldsymbol{q},t)\} = \{\hat{a}_M^{\dagger}(\boldsymbol{p},s),\hat{b}_M^{\dagger}(\boldsymbol{q},t)\} = 0, \tag{4.24}$$

These lead to ψ (c number) $\to \hat{\psi}$ (operator), and their field operator satisfies the following relations

$$\{\hat{\psi}_a(x),\hat{\psi}_b^{\dagger}(y)\} = \delta(x-y)\delta_{ab}, \tag{4.25}$$
$$\{\hat{\psi}_a(x),\hat{\psi}_b(y)\} = \{\hat{\psi}_a^{\dagger}(x),\hat{\psi}_b^{\dagger}(y)\} = 0, \tag{4.26}$$

Moreover, the operators $\hat{\alpha}_M$ and $\hat{\beta}$ that have been introduced by the Bogoliubov transformation also satisfy the canonical anticommutation relations

$$\{\hat{\alpha}(\boldsymbol{p},s),\hat{\alpha}^\dagger(\boldsymbol{q},t)\} = \{\hat{\beta}(\boldsymbol{p},s),\hat{\beta}^\dagger(\boldsymbol{q},t)\} = \delta(\boldsymbol{p}-\boldsymbol{q})\delta_{st}, \tag{4.27}$$

$$\{\hat{\alpha}(\boldsymbol{p},s),\hat{\alpha}(\boldsymbol{q},t)\} = \{\hat{\beta}(\boldsymbol{p},s),\hat{\beta}(\boldsymbol{q},t)\} = 0, \tag{4.28}$$

$$\{\hat{\alpha}(\boldsymbol{p},s),\hat{\beta}(\boldsymbol{q},t)\} = \{\hat{\alpha}^\dagger(\boldsymbol{p},s),\hat{\beta}^\dagger(\boldsymbol{q},t)\} = 0, \tag{4.29}$$

which means that the quasi-particles obtained by the Bogoliubov transformation are also the Fermi particles. Eq. (4.21) can be regarded as the free fermion's Hamiltonian. Their expectation values thus can be represented by those of the free fermion's number operator

$$\langle c^\dagger c\rangle = \frac{1}{1+e^{(E-\mu)/T}} = n(E), \tag{4.30}$$

where c and E are the annihilation operator of the fermion and its energy, respectively, and $n(E)$ is the Fermi-Dirac distribution function. Adopting Eq. (4.30) for the fermion bilinears in Eq. (4.21), we obtain the explicit form of the thermodynamic potential per volume in the MFA

$$\begin{aligned}\omega_{\rm MFA} = \frac{(M_D)^2}{4G_S} + \frac{|\Delta|^2}{4G_D} - 4\int\frac{d^3p}{(2\pi)^3}\Big\{E_{\boldsymbol{p}} + T\log\big(1+e^{-\xi_+/T}\big)\big(1+e^{-\xi_-/T}\big)\\ + \epsilon_+ + {\rm sgn}(\xi_-)\epsilon_- + 2T\log\big(1+e^{-\epsilon_+/T}\big)\big(1+e^{-{\rm sgn}(\xi_-)\epsilon_-/T}\big)\Big\}.\end{aligned} \tag{4.31}$$

$$M = m + M_D, \quad E_{\boldsymbol{p}} = \sqrt{\boldsymbol{p}^2+M^2}, \quad \xi_\pm = E_{\boldsymbol{p}} \pm \mu, \quad \epsilon_\pm = \sqrt{\xi_\pm^2+|\Delta|^2}. \tag{4.32}$$

As discussed already, the physical state is determined by the minimal point of $\omega_{\rm MFA} = \omega_{\rm MFA}(M_D,\Delta)$ at given (T,μ). Therefore, they satisfy the stationary conditions

$$\frac{\partial\omega_{\rm MFA}(M_D,\Delta)}{\partial M_D} = 0 \tag{4.33}$$

$$\frac{\partial\omega_{\rm MFA}(M_D,\Delta)}{\partial \Delta} = 0 \tag{4.34}$$

whose calculations lead to the gap equations for M_D and Δ, respectively,

$$M_D = 8G_S M\int\frac{d^3p}{(2\pi)^3}\frac{1}{E_{\boldsymbol{p}}}\left\{1-n(\xi_+)-n(\xi_-)+\frac{\xi_+}{\epsilon_+}\tanh\frac{\epsilon_+}{2T}+\frac{\xi_-}{\epsilon_-}\tanh\frac{\epsilon_-}{2T}\right\}, \tag{4.35}$$

$$\Delta = 8G_D\Delta\int\frac{d^3p}{(2\pi)^3}\left\{\frac{1}{\epsilon_+}\tanh\frac{\epsilon_+}{2T}+\frac{1}{\epsilon_-}\tanh\frac{\epsilon_-}{2T}\right\}. \tag{4.36}$$

We note that Eqs. (4.33) and (4.34) or Eqs. (4.35) and (4.36) are not sufficient conditions for the determination of M_D and Δ since $\omega_{\rm MFA}$ can possess some local minima and maxima. Thereby, to search for the true minimal point, we have to compute it numerically.

Finally, we calculate the curvature of $\Omega_{\rm MFA}$ around the physical value of (M_D,Δ) at a given (T,μ). In Sec. 2, we have confirmed that the curvature of free energy density or effective potential vanishes at second-order phase transitions, which causes critical phenomena. The QCD-CP and the phase transition to the 2SC (2SC-PT) calculated by the MFA in the NJL model are second-order phase transitions. In fact, the following conditions

$$\frac{\partial^2\omega_{\rm MFA}(M_D,\Delta)}{\partial^2 M_D} = 0, \tag{4.37}$$

$$\frac{\partial^2\omega_{\rm MFA}(M_D,\Delta)}{\partial^2 \Delta} = 0 \tag{4.38}$$

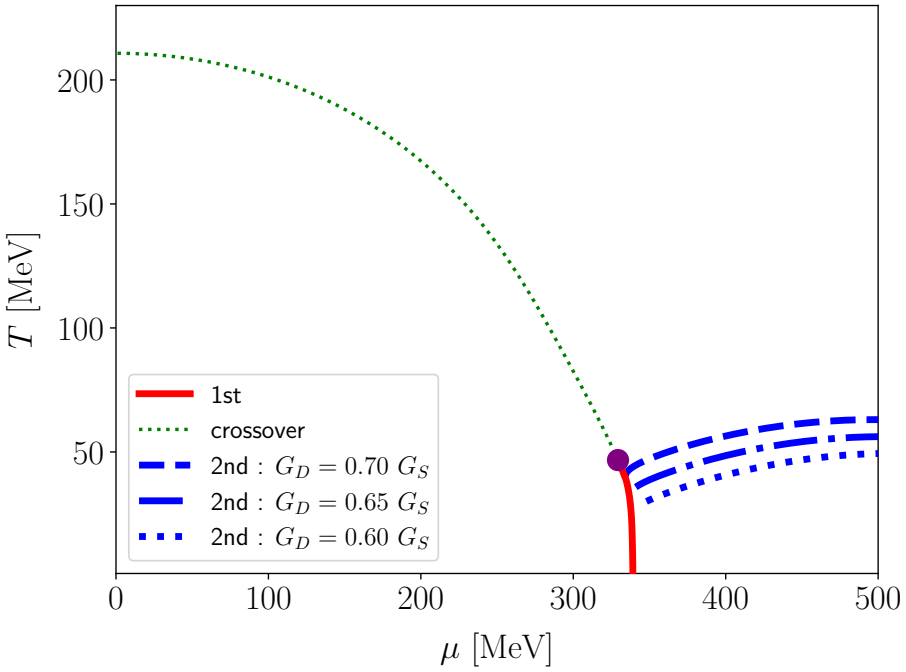

FIGURE 4.1: Phase diagram calculated by the mean-field approximation in the 2-flavor NJL model (4.1). The solid line shows the first-order phase transition, which is calculated with $G_D = 0.70 G_S$. The dashed, dash-dotted, and dotted lines are the second-order 2SC-PT for $G_D/G_S = 0.70$, 0.65, and 0.60, respectively. The QCD CP is represented by the circle marker, which is located at $(T_{\rm CP}, \mu_{\rm CP}) \simeq (46.712, 329.34)$ MeV.

are satisfied at the QCD-CP and the 2SC-PT, respectively. Eqs. (4.37) and (4.38) are easily calculated with the aid of the gap equations (4.35) and (4.36) as follows

$$G_S^{-1} = 2N_f N_c \sum_{s=\pm} \int \frac{d^3p}{(2\pi)^3} \frac{M}{E_p} \frac{\partial}{\partial E_p} \left[\frac{M}{E_p} \tanh \frac{E_p - s\mu}{2T} \right], \tag{4.39}$$

$$G_D^{-1} = 2N_f (N_c - 1) \int \frac{d^3p}{(2\pi)^3} \left\{ \frac{1}{\epsilon_+} \tanh \frac{\epsilon_+}{2T} + \frac{1}{\epsilon_-} \tanh \frac{\epsilon_-}{2T} \right\}. \tag{4.40}$$

These results will be utilized again in Chap. 5.

4.2 Phase diagram

Figure 4.1 shows the phase diagram obtained by the MFA. In the figure, the solid line represents the first-order phase transition triggered by the dynamical chiral symmetry breaking at the diquark coupling $G_D = 0.70 G_S$, while the dashed, dash-dotted, and dotted lines are the second-order phase transition to the 2SC phase with $G_D = 0.70 G_S$, $0.65 G_S$, and $0.60 G_S$, respectively. The 2SC phase is realized in the dense region at relatively low temperatures. Also, the circle marker at $(T_{\rm CP}, \mu_{\rm CP}) \simeq (46.712, 329.34)$ MeV is the QCD-CP, and the thin-dotted line is the crossover transition line, which is defined by the value that $\partial M_D/\partial T$ takes the maximal value at fixed μ.

In Fig. 4.2, we shows the M_D and Δ as a function of T at fixed μ. One can find differences in the behavior of M_D due to the value of μ in the left panel. At $\mu = 335$ MeV, M_D changes discontinuously at $T \simeq 38$ MeV, which indicates that the phase transition at this point is the first order. On the other hand, at $\mu = 325$ MeV, the change of M_D is smooth, while it changes rapidly around $T \simeq 52$ MeV as in the case of $\mu > \mu_{CP}$, which is the crossover transition.

At $\mu = \mu_{CP}$, M_D changes continuously, whereas $\partial M_D/\partial T$ is divergent at $T = T_{CP} \simeq 46$ MeV. The point (T_{CP}, μ_{CP}) is the QCD-CP, whose order of the phase transition is the second order, where

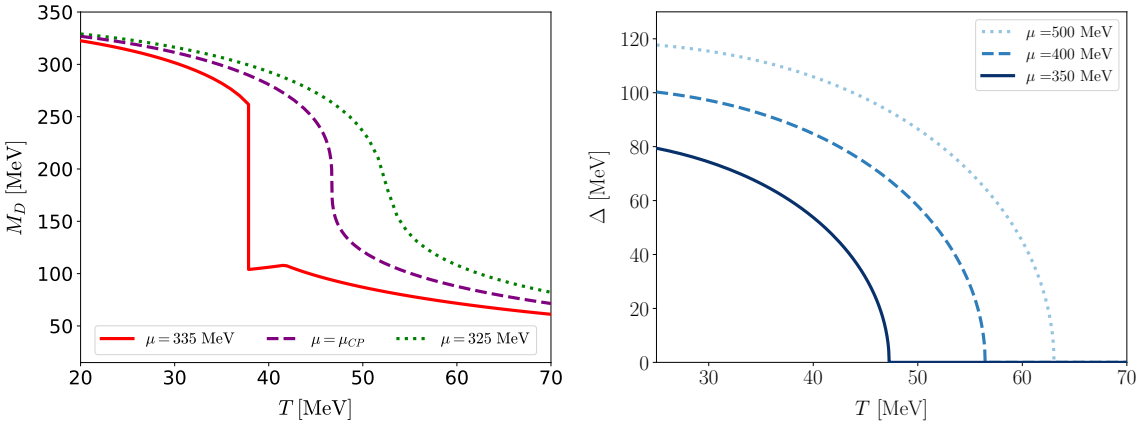

FIGURE 4.2: Temperature dependence of the chiral condensate M_D and diquark condensate Δ. In the left panel, the results of M_D at $\mu = 335$ MeV, μ_{CP}, and 325 MeV are shown in the range 20 MeV $< T <$ 70 MeV, while in the right panel, the results of Δ at $\mu = 350$ MeV, 400 MeV, and 500 MeV are shown in the range 25 MeV $< T <$ 70 MeV.

various susceptibilities are divergent. At this point, the first-order PT and crossover transition lines connect smoothly. While we consider the finite current quark mass, if we take the chiral limit or in the massless case, the crossover transition becomes the second-order phase transition owing to $O(4)$ symmetry breaking, which reflects the change of the universality class in this limit. In this limit, the QCD critical point becomes the tri-critical point.

In the right panel, the T-dependence of Δ is shown for $\mu = 350$ MeV, 400 MeV, and 500MeV. Since all plots of Δ behave continuously, one can confirm that the 2SC phase transition is the second order. The order of the CSC-PT, however, would be modified by the effects beyond the analysis of MFA. The order can become a first order owing to the fluctuations of gluon fields in asymptotically high-density region [90, 91, 92] which are not included in our analysis. Also, it might persist in lower densities [93]. From the view of the symmetry point, it would also be possible that this transition is crossover. However, since the definite conclusion on the order of the 2SC-PT has not been obtained so far to the best of the author's knowledge, we simply assume the second-order transition in the following.

Chapter 5

Soft modes

In this chapter, we examine the collective fluctuations of the diquark $\bar{\psi}^C i\gamma_5\tau_2\lambda_A\psi$ and chiral scalar fields $\bar{\psi}\psi$. Their fluctuations couple to the soft modes of the 2SC-PT and QCD-CP, respectively [42, 20, 21, 84, 85]. Most of this chapter is written based in Refs. [42, 20, 21]. On the other hand, in this chapter, detailed manipulations skipped in those previous papers are described with an emphasis on the common and different properties of the soft modes due to the respective phase transitions.

As described in Sec. 3.2, dynamical properties of the fluctuations of a field operator $\mathcal{O}(\boldsymbol{x},t)$ are encoded in the response function, which is equivalent to the retarded Green's function

$$D^R(\boldsymbol{k},\omega) = \int d^3x dt e^{i\omega t - i\boldsymbol{k}\cdot\boldsymbol{x}} D^R(\boldsymbol{x},t), \tag{5.1}$$

$$D^R(\boldsymbol{x},t) = -i\langle[\mathcal{O}(\boldsymbol{x},t),\mathcal{O}(\boldsymbol{0},0)]\rangle\theta(t), \tag{5.2}$$

for a bosonic operator $\mathcal{O}(\boldsymbol{x},t)$. The pole of $D^R(\boldsymbol{k},\omega)$ at $\omega = \omega(\boldsymbol{k})$, which exists in the lower-half complex-energy plane, represents the collective mode that couples to $\mathcal{O}(\boldsymbol{x},t)$. When the imaginary part of $\omega(\boldsymbol{k})$ is small, the dynamical structure factor defined by

$$S(\boldsymbol{k},\omega) = -\frac{1}{\pi}\frac{1}{e^{\omega/T}-1}\mathrm{Im}D^R(\boldsymbol{k},\omega), \tag{5.3}$$

has a peak around $\omega = \mathrm{Re}\,\omega(\boldsymbol{k})$, which conspicuously shows the existence of the collective modes. The response functions that couple to the soft modes of the 2SC-PT and QCD-CP are given by substituting the diquark and chiral scalar fields

$$\hat{\delta}_A(\boldsymbol{x},t) = \bar{\psi}^C(\boldsymbol{x},t)i\gamma_5\tau_2\lambda_A\psi(\boldsymbol{x},t), \tag{5.4}$$

$$\hat{\sigma}(\boldsymbol{x},t) = \bar{\psi}(\boldsymbol{x},t)\psi(\boldsymbol{x},t), \tag{5.5}$$

into the operator $\mathcal{O}(\boldsymbol{x},t)$ in Eq. (5.2), respectively, which are denoted as $D_D^R(\boldsymbol{k},\omega)$ and $D_S^R(\boldsymbol{k},\omega)$ in what follows.

To calculate $D_D^R(\boldsymbol{k},\omega)$ and $D_S^R(\boldsymbol{k},\omega)$, it is convenient to use the imaginary-time Green's functions corresponding to the respective response functions

$$\mathcal{D}_D(k) = \mathcal{D}_D(\boldsymbol{k},i\nu_n) = \int d^3x dt e^{i\nu_n\tau - i\boldsymbol{k}\cdot\boldsymbol{x}}\langle T_\tau\hat{\delta}_A(\boldsymbol{x},\tau)\hat{\delta}_A^\dagger(\boldsymbol{0},0)\rangle, \tag{5.6}$$

$$\mathcal{D}_S(k) = \mathcal{D}_S(\boldsymbol{k},i\nu_n) = \int d^3x dt e^{i\nu_n\tau - i\boldsymbol{k}\cdot\boldsymbol{x}}\langle T_\tau\hat{\sigma}(\boldsymbol{x},\tau)\hat{\sigma}(\boldsymbol{0},0)\rangle, \tag{5.7}$$

where $k = (\boldsymbol{k},i\nu_n)$ is the four-momentum in imaginary time with $\nu_n = 2\pi n/T$. The response functions are obtained from Eqs. (5.6) and (5.7) by the analytic continuation

$$D_\gamma^R(\boldsymbol{k},\omega) = \mathcal{D}_\gamma(k)|_{i\nu_n\to\omega+i\eta}, \quad \gamma = D \text{ and } S, \tag{5.8}$$

with η being a positive infinitesimal number.

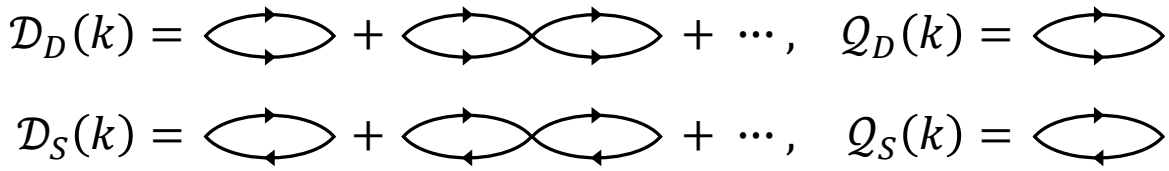

FIGURE 5.1: Diagrammatic representation of the response functions (5.9) in the RPA and the one-loop correlation functions (5.10) and (5.11). The single lines are quarks.

5.1 Random-phase approximation

We calculate Eqs. (5.6) and (5.7) in the random-phase approximation (RPA), where the Green's functions are given by

$$\mathcal{D}_\gamma(k) = \frac{\mathcal{Q}_\gamma(k)}{1 + G_\gamma \mathcal{Q}_\gamma(k)}, \tag{5.9}$$

with the unperturbed correlation functions

$$\begin{aligned}
\mathcal{Q}_D(k) = \mathcal{Q}_D(\boldsymbol{k}, i\nu_n) &= \int d^3x dt e^{i\nu_n\tau - i\boldsymbol{k}\cdot\boldsymbol{x}} \langle T_\tau \hat{\delta}_A(\boldsymbol{x},\tau)\hat{\delta}_A^\dagger(\boldsymbol{0},0)\rangle_{\text{free}} \\
&= \int_p \mathrm{Tr}_{f,c,d}[i\gamma_5\tau_2\lambda_A \mathcal{G}_0(k-p) i\gamma_5\tau_2\lambda_A \mathcal{G}_0^T(p)] \\
&= -2N_f(N_c-1)\int_p \mathrm{Tr}_D[\mathcal{G}_0(k-p)\mathcal{G}_0(k)], \qquad (5.10) \\
\mathcal{Q}_S(k) = \mathcal{Q}_S(\boldsymbol{k}, i\nu_n) &= \int d^3x dt e^{i\nu_n\tau - i\boldsymbol{k}\cdot\boldsymbol{x}} \langle T_\tau \hat{\sigma}(\boldsymbol{x},\tau)\hat{\sigma}(\boldsymbol{0},0)\rangle_{\text{free}} \\
&= \int_p \mathrm{Tr}_{f,c,d}[\mathcal{G}_0(k+p)\mathcal{G}_0(p)] \\
&= -2N_f N_c \int_p \mathrm{Tr}_D[\mathcal{G}_0(k+p)\mathcal{G}_0(p)]. \qquad (5.11)
\end{aligned}$$

Here, $\langle\cdot\rangle_{\text{free}}$ denotes the expectation value in the non-interacting system and

$$\mathcal{G}_0(p) = \mathcal{G}_0(\boldsymbol{p}, i\omega_m) = \frac{1}{(i\omega_m+\mu)\gamma_0 - \boldsymbol{p}\cdot\boldsymbol{\gamma} - M}, \tag{5.12}$$

is the free-quark propagator with $\omega_m = (2m+1)\pi T$. Tr denotes the trace over the flavor (f), color (c), and Dirac (D) indices, and $\int_p = T\sum_m \int d^3p/(2\pi)^3$ is the Matsubara-frequency summation and the momentum integration. Equations (5.10) and (5.11) are diagrammatically represented by the one-loop graphs as shown in Fig. 5.1, while $\mathcal{D}_D(k)$ and $\mathcal{D}_S(k)$ are given by the sum of their products as in the figure. The RPA for the particle-particle mode $\mathcal{D}_D(k)$ is also referred to as the T-matrix approximation in the literature [45].

The integrands of $\mathcal{Q}_D(k)$ and $\mathcal{Q}_S(k)$ are computed as

$$\begin{aligned}
\mathrm{Tr}_d[\mathcal{G}_0(k-p)\mathcal{G}_0(p)] &= (i\omega_m+\mu)(i\nu_n - i\omega_m+\mu) + (e_1^2+e_2^2-\boldsymbol{k}^2)/2 \\
&\quad \times \frac{1}{e_1e_2}\sum_{s,t=\pm}\frac{st}{(i\omega_m+\mu+se_1)(i\omega_m - i\nu_n - \mu + te_2)}, \qquad (5.13) \\
\mathrm{Tr}[_d\mathcal{G}_0(k+p)\mathcal{G}_0(p)] &= (i\omega_m+\mu)(i\nu_n + i\omega_m+\mu) + (e_1^2+e_2^2-\boldsymbol{k}^2-4M^2)/2 \\
&\quad \times \frac{1}{e_1e_2}\sum_{s,t=\pm}\frac{st}{(i\omega_m+\mu+se_1)(i\omega_m - i\nu_n + \mu + te_2)}, \qquad (5.14)
\end{aligned}$$

where $e_1 = \sqrt{\boldsymbol{p}^2 + M^2}$ and $e_2 = \sqrt{(\boldsymbol{k} \mp \boldsymbol{p})^2 + M^2}$. Replacing the sum of $i\omega_m$ by the residue integration with Eq. (3.23), we obtain

$$\begin{aligned}\mathcal{Q}_D(\boldsymbol{k}, i\nu_n) = \frac{N_f(N_c-1)}{2}\int \frac{d^3p}{(2\pi)^3}\frac{1}{e_1e_2} \\ \times \sum_{s,t=\pm} st\Bigg\{ \tanh\frac{se_1-\mu}{2T}\left[2e_1 - \frac{(se_1-te_2)^2-\boldsymbol{k}^2}{se_1-te_2-i\nu_n-2\mu}\right] \\ + \tanh\frac{te_2-\mu}{2T}\left[2e_2 - \frac{(te_2-se_1)^2-\boldsymbol{k}^2}{te_2-se_1-i\nu_n-2\mu}\right]\Bigg\},\end{aligned} \tag{5.15}$$

$$\begin{aligned}\mathcal{Q}_S(\boldsymbol{k}, i\nu_n) = \frac{N_fN_c}{2}\int \frac{d^3p}{(2\pi)^3}\frac{1}{e_1e_2} \\ \times \sum_{s,t=\pm} st\Bigg\{ \tanh\frac{se_1-\mu}{2T}\left[\frac{(se_1-te_2)^2-\boldsymbol{k}^2-4M^2}{se_1-te_2-i\nu_n} - 2e_1\right] \\ + \tanh\frac{te_2-\mu}{2T}\left[\frac{(te_2-se_1)^2-\boldsymbol{k}^2-4M^2}{te_2-se_1-i\nu_n} - 2e_2\right]\Bigg\}.\end{aligned} \tag{5.16}$$

The momentum integral in Eqs. (5.15) and (5.16) are nicely converted as follows

$$\int \frac{d^3p}{(2\pi)^3}\frac{1}{e_1e_2} = \frac{1}{(2\pi)^2}\int p^2dp\int_{-1}^{1} d(\cos\theta) = \frac{1}{2(2\pi)^2|\boldsymbol{k}|}\int_{\lambda(|\boldsymbol{k}|,0)}^{\bar{\Lambda}} dE_1\int_{-\lambda(|\boldsymbol{k}|,E_1)}^{+\lambda(|\boldsymbol{k}|,E_1)} dE_2, \tag{5.17}$$

$$\lambda(|\boldsymbol{k}|,\omega) = |\boldsymbol{k}|\sqrt{1-4M^2/(\omega^2-\boldsymbol{k}^2)},\quad \bar{\Lambda} = 2\sqrt{\Lambda^2+M^2}, \tag{5.18}$$

where $E_1 = e_1 + e_2$ and $E_2 = e_1 - e_2$. In Eq. (5.17), we have introduced the UV cutoff $\bar{\Lambda}$ on the E_1 integral. This cutoff is often called the four-momentum cutoff, which is chosen so that the range of the three-momentum integral is consistent with that used for Eq. (4.31) at $\boldsymbol{k} = \boldsymbol{0}$. In general, there are a variety of schemes to determine the cutoff into the momentum direction, while the behavior of the correlation function in the low energy/momentum is insensitive to them in any case.

The retarded Green's functions $Q_D^R(\boldsymbol{k},\omega)$ and $Q_S^R(\boldsymbol{k},\omega)$ of Eqs. (5.15) and (5.16), respectively, are obtained by the analytic continuation $i\nu_n \to \omega + i\eta$. Their imaginary parts are calculated to be

$$\begin{aligned}\mathrm{Im}Q_D^R(\boldsymbol{k},\omega) = \frac{N_f(N_c-1)}{32\pi|\boldsymbol{k}|}\int_{-\lambda(|\boldsymbol{k}|,\bar{\Lambda})}^{+\lambda(|\boldsymbol{k}|,\bar{\Lambda})} dE_2\int_{\lambda(|\boldsymbol{k}|,E_2)}^{\bar{\Lambda}} dE_1, \\ \times \sum_{s,t=\pm}\Big\{ s(E_1^2-\boldsymbol{k}^2)\tanh\frac{E_1+tE_2-2s\mu}{4T}\,\delta\big(E_1 - s(\omega+2\mu)\big) \\ - s(E_2^2-\boldsymbol{k}^2)\tanh\frac{E_2+tE_1-2s\mu}{4T}\,\delta\big(E_2 - s(\omega+2\mu)\big)\Big\},\end{aligned} \tag{5.19}$$

$$\begin{aligned}\mathrm{Im}Q_S^R(\boldsymbol{k},\omega) = \frac{N_fN_c}{32\pi|\boldsymbol{k}|}\int_{\lambda(|\boldsymbol{k}|,0)}^{\bar{\Lambda}} dE_1\int_{-\lambda(|\boldsymbol{k}|,E_1)}^{+\lambda(|\boldsymbol{k}|,E_1)} dE_2, \\ \times \sum_{s,t=\pm}\Big\{ s(E_1^2-\boldsymbol{k}^2-4M^2)\tanh\frac{E_1+t(E_2-2s\mu)}{4T}\,\delta\big(E_1 - s\omega\big) \\ - s(E_1^2-\boldsymbol{k}^2-4M^2)\tanh\frac{E_2+t(E_1-2s\mu)}{4T}\,\delta\big(E_2 - s\omega\big)\Big\},\end{aligned} \tag{5.20}$$

where the following formula

$$\frac{1}{x \pm i\eta} = \frac{P}{x} \mp i\pi\delta(x) \tag{5.21}$$

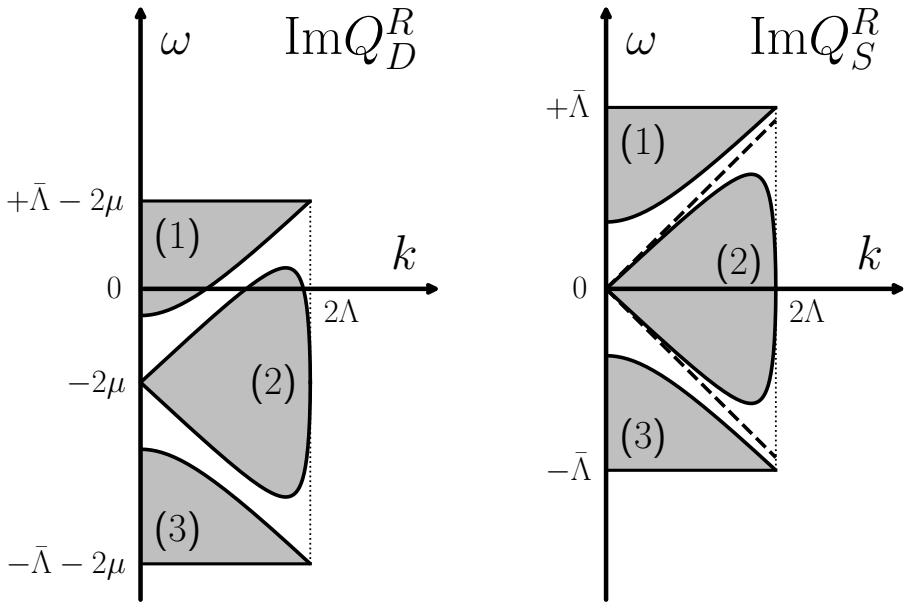

FIGURE 5.2: The support regions of $\mathrm{Im}Q_D^R(\boldsymbol{k},\omega)$ (left) and $\mathrm{Im}Q_S^R(\boldsymbol{k},\omega)$ (right) in the energy/momentum plane. The shaded areas in both panels are given by the step functions in Eqs. (5.19) and (5.20), respectively. The regions (1) and (3) represent the support of the first line of Eqs. (5.19) and (5.20), while the region (2) corresponds to the second line. The dashed line in the right panel shows the light cone.

has been used. After the delta functions in Eqs. (5.19) and (5.20) are integrated out, the remaining integrals of E_1 or E_2 can be carried out analytically as follows

$$\begin{aligned}\mathrm{Im}Q_D^R(\boldsymbol{k},\omega) = &-\frac{N_f(N_c-1)T}{4\pi}\frac{(\omega+2\mu)^2-\boldsymbol{k}^2}{|\boldsymbol{k}|}\\ &\times\Big\{\theta\big(\bar{\Lambda}-|\omega+2\mu|\big)\theta\big(|\omega+2\mu|-\lambda(|\boldsymbol{k}|,0)\big)F_D\big(\omega,\lambda(|\boldsymbol{k}|,\omega+2\mu)\big)\\ &\quad+\theta\big(\lambda(|\boldsymbol{k}|,\bar{\Lambda})-|\omega+2\mu|\big)\Big[F_D\big(\omega,\lambda(|\boldsymbol{k}|,\omega+2\mu)\big)-F_D\big(\omega,\bar{\Lambda}\big)\Big]\Big\},\end{aligned} \tag{5.22}$$

$$\begin{aligned}\mathrm{Im}Q_S^R(\boldsymbol{k},\omega) = &-\frac{N_fN_cT}{4\pi}\frac{\omega^2-\boldsymbol{k}^2-4M^2}{|\boldsymbol{k}|}\\ &\times\Big\{\theta\big(\bar{\Lambda}-|\omega|\big)\theta\big(|\omega|-\lambda(|\boldsymbol{k}|,0)\big)F_S\big(\omega,\lambda(|\boldsymbol{k}|,\omega)\big)\\ &\quad+\theta\big(\lambda(|\boldsymbol{k}|,\bar{\Lambda})-|\omega|\big)\Big[F_S\big(\omega,\lambda(|\boldsymbol{k}|,\omega)\big)-F_S\big(\omega,\bar{\Lambda}\big)\Big]\Big\},\end{aligned} \tag{5.23}$$

where

$$F_D(\omega,z) = 2\sum_{s=\pm} s\log\,\cosh([\omega+sz]/4T), \tag{5.24}$$

$$F_S(\omega,z) = \sum_{s,t=\pm} s\log\,\cosh([\omega+sz-2t\mu]/4T). \tag{5.25}$$

Although $\mathrm{Im}\Xi_\gamma^R(\boldsymbol{k},\omega)$ have seemingly similar structures with each other, the analytic structures are significantly different due to the different locations of the term 2μ, which leads to a difference in the supports of Eqs. (5.19) and (5.20). The first (second) term in the curly bracket in Eq. (5.19) takes a nonzero value at $|\omega+2\mu|>\lambda(|\boldsymbol{k}|,0)$ ($|\omega+2\mu|<\lambda(|\boldsymbol{k}|,\bar{\Lambda})$), while that in Eq. (5.20) is nonzero at $|\omega|>\lambda(|\boldsymbol{k}|,0)$ ($|\omega|<\lambda(|\boldsymbol{k}|,\bar{\Lambda})$). As is shown in Fig. 5.2, these supports are deviated by 2μ in the ω–$|\boldsymbol{k}|$ plane between Eqs. (5.19) and (5.20). We also note that the supports of the terms in Eq. (5.20) are both in the time- and space-like regions.

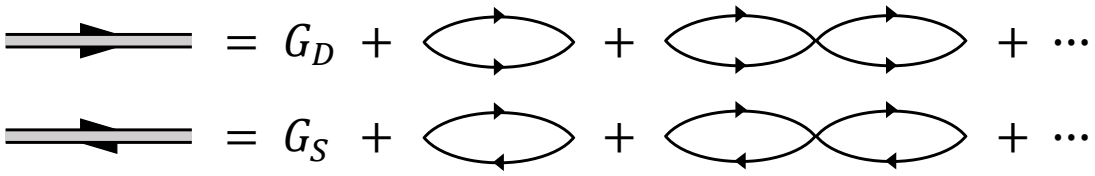

FIGURE 5.3: Diagrammatic representation of $\Xi_\gamma(\boldsymbol{k},\omega)$ in the RPA. The double lines are the propagators of the soft modes.

An explicit calculation easily shows that $Q_D^R(\boldsymbol{k},\omega)$ and $Q_S^R(\boldsymbol{k},\omega)$ are not analytic at the boundary of the supports. Accordingly, $Q_S^R(\boldsymbol{k},\omega)$ is not analytic at the origin $(|\boldsymbol{k}|,\omega) = (0,0)$ in the ω–$|\boldsymbol{k}|$ plane, while $Q_D^R(\boldsymbol{k},\omega)$ is continuous there. The non-analyticity of $Q_S^R(\boldsymbol{k},\omega)$ at the origin is readily understood by the fact that the limiting value of $\mathrm{Im}Q_S^R(\boldsymbol{k},\omega)$ at the origin depends on the direction to approach,

$$\lim_{|\boldsymbol{k}|\to 0} \mathrm{Im}Q_S^R(\boldsymbol{k}, a|\boldsymbol{k}|) = a\,\frac{N_f N_c M^2}{2\pi}\sum_{t=\pm}\left\{\tanh\frac{\lambda_a - 2t\mu}{4T} - \tanh\frac{\bar{\Lambda} - 2t\mu}{4T}\right\}\theta\left(\frac{2\Lambda}{\bar{\Lambda}} - |a|\right), \tag{5.26}$$

with $\lambda_a = \sqrt{4M^2/(1-a^2)}$.

To calculate the real parts of $Q_D^R(\boldsymbol{k},\omega)$ and $Q_S^R(\boldsymbol{k},\omega)$, it is convenient to use the Kramers-Kronig relation for Eqs. (5.22) and (5.23)

$$\mathrm{Re}Q_\gamma^R(\boldsymbol{k},\omega) = \frac{P}{\pi}\int d\omega' \frac{\mathrm{Im}Q_\gamma^R(\boldsymbol{k},\omega')}{\omega' - \omega}, \tag{5.27}$$

where P denotes the principal value. The integral regions in Eqs. (5.27) are determined by the supports of $\mathrm{Im}Q_\gamma^R(\boldsymbol{k},\omega')$ given in Eqs. (5.22) and (5.23). One can easily verify that Eq. [**?**] agrees with the retarded functions obtained by the analytic continuation of Eqs. (5.15) and (5.16) with Eq. (5.17).

5.2 Thouless criterion

Since $D_D^R(\boldsymbol{k},\omega)$ and $D_S^R(\boldsymbol{k},\omega)$ possess all the information of collective modes coupled to the operators in Eq. (5.5), they encode the properties of the respective soft modes. Thus the fact that the soft modes become massless at the second-order phase transition is ensured by the Thouless criterion [94], which is a peculiar property of $D_D^R(\boldsymbol{k},\omega)$ and $D_S^R(\boldsymbol{k},\omega)$. These response functions have a pole at the origin of the complex ω plane at $\boldsymbol{k} = \boldsymbol{0}$ at the critical point.

To show the Thouless criterion, it is convenient first to introduce the retarded T-matrix $\Xi_\gamma^R(\boldsymbol{k},\omega)$ defined by

$$\begin{aligned}\Xi_\gamma^R(\boldsymbol{k},\omega) &= G_\gamma - G_\gamma D_\gamma^R(\boldsymbol{k},\omega)G_\gamma \\ &= \frac{1}{G_\gamma^{-1} + Q_\gamma^R(\boldsymbol{k},\omega)},\end{aligned} \tag{5.28}$$

Their diagrammatic representations are given in Fig. 5.3. From Eq. (5.28), it is readily confirmed that the following relations hold with the curvatures of the respective thermodynamic potentials,

$$\Xi_D^{R\,-1}(\boldsymbol{0},0) = \frac{\partial^2\omega_{\mathrm{MFA}}}{\partial\Delta^2}, \tag{5.29}$$

$$\Xi_S^{R\,-1}(\boldsymbol{0},0) = \frac{\partial^2\omega_{\mathrm{MFA}}}{\partial M_D^2}. \tag{5.30}$$

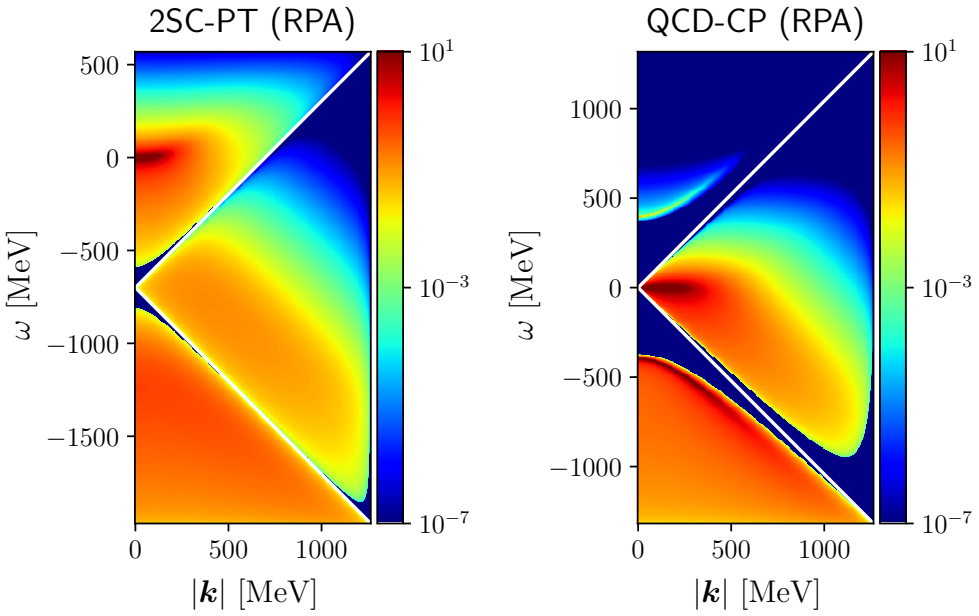

FIGURE 5.4: Contour map of the dynamical structure factor for the respective soft modes with $G_D = 0.7G_S$ in the energy/momentum plane calculated by the RPA. The left panel is the result of $S_D(\boldsymbol{k},\omega)$ at $T = T_c$ (47.260 MeV) and $\mu = 350$ MeV, while the right one is the result of $S_S(\boldsymbol{k},\omega)$ at $T = T_{\rm CP}$ and $\mu = \mu_{\rm CP}$. In both panels, the white lines show the discontinuities in the massless case.

Since the thermodynamic potential satisfies the conditions (4.37) and (4.38), we obtain

$$0 = \Xi_\gamma^{R\,-1}(\boldsymbol{0},0) = D_\gamma^{R\,-1}(\boldsymbol{0},0), \tag{5.31}$$

at the respective critical points. Equation (5.31) proves the existence of a pole in $D_\gamma^R(\boldsymbol{k},\omega)$ at the origin $(|\boldsymbol{k}|,\omega) = (0,0)$, implying that the Thouless criterion surely holds. The pole at $\omega = 0$ at the critical point, whose existence is ensured by the Thouless criterion, moves continuously in the lower-half complex-energy plane as a function of T and μ. This means the existence of the soft mode near the critical point, i.e., the collective mode associated with a pole near the origin that eventually becomes massless at the critical point. In this sense, we call $\tilde{\Xi}_\gamma(k)$ the propagator of the respective soft modes in this thesis.

Let us consider the difference between the 2SC-PT and QCD-PT soft modes. As was discussed in Sec. 5.1, $D_D^R(\boldsymbol{k},\omega)$ is analytic at the origin, while $D_S^R(\boldsymbol{k},\omega)$ is not. This difference leads to a qualitative difference in the analytic properties between the soft modes of 2SC-PT and QCD-CP. In terms of the dynamical structure factor, $S_D(\boldsymbol{k},\omega)$ is a smooth function around the origin, while $S_S(\boldsymbol{k},\omega)$ has distinct spectral supports in the time- and space-like regions. Correspondingly, $D_S^R(\boldsymbol{k},\omega)$ has poles in both regions. Among them, a pole in the space-like region behaves as the soft mode that moves toward the origin in the complex ω plane [20, 21], while any pole in the time-like region does not show such a softening behavior. Indeed the spectral supports of $S_S(\boldsymbol{k},\omega)$ in the time-like region exist only at $|\omega| > \lambda(|\boldsymbol{k}|,0) = \sqrt{\boldsymbol{k}^2 + 4M^2}$. Since M stays nonzero at the QCD-CP, the pole in the time-like region never becomes massless. On the other hand, both soft modes have one similarity, which is the fact that the contributions of the soft modes concentrate on the low energy/momentum region of the space-like region and the strength becomes prominently enhanced near the critical points.

In the left panel of Fig. 5.4, we show a contour map of the dynamical structure factor of diquark field $S_D(\boldsymbol{k},\omega)$ at $T = T_c$ for $\mu = 350$ MeV and $G_D = 0.7G_S$. From the panel, one finds that the spectral weight of $S_D(\boldsymbol{k},\omega)$ is concentrated in the low energy/momentum region, which implies a development of the collective diquark mode with the small energy. In the right panel of Fig. 5.4, we show a contour map of the dynamical structure factor $S_S(\boldsymbol{k},\omega)$ at the QCD-CP $(T,\mu) = (T_{\rm CP},\mu_{\rm CP})$.

From the figure, one sees that $S_S(\boldsymbol{k},\omega)$ has nonzero values only in the space-like region around the origin. The peak structure at the origin emerges within this region, while $S_S(\boldsymbol{k},\omega) = 0$ when approaching the origin in the time-like region. It is noted that the QCD-CP soft mode in the space-like region is called a particle-hole mode, while the collective mode in the time-like region is the sigma mode, the latter of which does not become massless even at the QCD-CP [20, 21, 95, 96]

Before closing this subsection, let us briefly discuss the effect of the current quark mass m on the properties of the soft modes. First, it is readily found that the properties of the soft mode of the 2SC-PT are hardly affected by m as one can confirm by an explicit calculation. This result is understood intuitively from the fact that the soft mode of the 2SC-PT is the diquark mode that is dominated by the excitations near the Fermi surface that are less affected by the quark mass when $\mu \gg M$. On the other hand, the properties of the soft mode of the QCD-CP are crucially affected by m since the QCD-CP becomes a tri-critical point in the $m \to 0$ limit. One can also argue that the soft mode of the QCD-CP is less affected by the diquark gap Δ, while that of the 2SC-PT is crucially modified by it.

5.3 Effective theory of the soft modes

In this section, we derive effective formulas of $\Xi_D^R(\boldsymbol{k},\omega)$ and $\Xi_S^R(\boldsymbol{k},\omega)$ that have a good accuracy near the 2SC-PT and QCD-CP, respectively. These formulas are used in the next chapter for the analysis of the photon self-energy including the effect of the soft modes.

5.3.1 2SC-PT soft mode

Noting that the T-matrix $\Xi_D^R(\boldsymbol{k},\omega)$ contains the information of the 2SC-PT soft mode, let us start by trying to derive an approximate formula of $\Xi_D^R(\boldsymbol{k},\omega)$ that is convenient to take into account the effects of the soft mode effectively.

Since the notion of the soft mode makes sense near the critical point where the collective excitation in the very soft mode channel has a spectral concentration in the low energy/momentum region, it is reasonable to make an approximation to $\Xi_D^R(\boldsymbol{k},\omega)$ by expanding its inverse with respect to ω and pick up the first two terms as

$$\Xi_D^{R\,-1}(\boldsymbol{k},\omega) \simeq A_D(\boldsymbol{k}) + C_D\omega, \tag{5.32}$$

$$A_D(\boldsymbol{k}) = G_D^{-1} + Q_D^R(\boldsymbol{k},0), \quad C_D = \left.\frac{\partial Q_D^R(\boldsymbol{0},\omega)}{\partial\omega}\right|_{\omega=0}, \tag{5.33}$$

where $A_D(\boldsymbol{k})$ and C_D are found to be real and complex numbers, respectively. From the Thouless criterion (5.31), $A_D(\boldsymbol{0}) = 0$ at $T = T_c$. In this approximation, we have neglected the $\boldsymbol{k}$ dependence of C_D as well as higher order terms of ω, which are justified near the origin. We call Eq. (5.32) the low-energy (LE) approximation. In Ref. [84], this approximate formula will be used for the calculation of the photon self-energy and the DPR. We note the limitation of this approximation: Since the 2SC-PT soft mode exists only at $\omega + 2\mu > \sqrt{\boldsymbol{k}^2 + 4M^2}$, the LE approximation is applicable only at $\boldsymbol{k}^2 < 4(\mu^2 - M^2)$. This means that we mostly cannot apply this approximation within the CSB phase because M tends to be bigger than μ there. Originally, the contribution of the 2SC-PT soft mode is contaminated by $M \geq 300$ MeV and the strength decreases drastically even in the analysis of the RPA level. Then, the issue of the limitation is consistent with the analysis of the RPA.

For treating the soft mode, one may make a further approximation to $\Xi_D^R(\boldsymbol{k},\omega)$ by expanding $A_D(\boldsymbol{k})$ with respect to $\boldsymbol{k}$. By picking up the first two terms of the expansion, one has

$$\Xi_D^{R\,-1}(\boldsymbol{k},\omega) \simeq a_D + b_D\boldsymbol{k}^2 + c_D\omega \tag{5.34}$$

$$a_D = A_D(\boldsymbol{0}) = G_D^{-1} + Q_D^R(\boldsymbol{0},0), \quad b_D = \left.\frac{\partial Q_D^R(\boldsymbol{k},0)}{\partial\boldsymbol{k}^2}\right|_{|\boldsymbol{k}|=0}, \quad c_D = C_D, \tag{5.35}$$

whose approximation is known as the linearized time-dependent Ginzburg-Landau (TDGL) approximation, as ${\Xi_D^R}^{-1}(\boldsymbol{k},\omega)\Delta(\boldsymbol{k},\omega) = 0$ with Eq. (5.37) corresponds to the linearized TDGL equation [45]. We note that $a_D = 0$ at $T = T_c$ is the Thouless criterion (5.31). The TDGL approximation has the same limitation of use as the one of the LE approximation.

It is noteworthy that Eq. (5.37) is rewritten as

$$\frac{1}{a_D + b_D\boldsymbol{k}^2 + c_D\omega} = \frac{i}{|\mathrm{Im}c_D|}\frac{1}{\omega + i\tau_D^{-1}(1+\xi_D^2\boldsymbol{q}^2)}, \tag{5.36}$$

where $\xi_D = \sqrt{b_D/a_D}$ and $\tau_D = |c_D|/a_D$ are interpreted as the coherence length and the relaxation time of the soft mode, respectively. These coefficients are corresponding to ξ_{GL} in Eq. (2.16) and $\tau_{GL}(\boldsymbol{0})$ in Eq. (2.26), which gives information on the transport phenomena for the 2SC-PT soft mode.

As was discussed in Sec. 5.1, $\Xi_D^R(\boldsymbol{k},\omega)$ is analytic in the shaded region in the left panel of Fig. 5.2. Since Eq. (5.37) is obtained by the expansion at the origin, it applies only to the region (2) in the panel where the origin is included. The same argument also applies to Eq. (5.32). In the following, we thus assume that $\Xi_D^R(\boldsymbol{k},\omega)$ vanishes outside the region (2), although this cutoff hardly modifies the property of the soft mode since $S_D(\boldsymbol{k},\omega)$ is well suppressed there.

Here, let us expand the coefficients of the TDGL approximation (5.35) for the T-direction at $T = T_c$. Since $a_D = 0$ at $T = T_c$ as described already, while b_D and c_D are insensitive to T in the vicinity of $T = T_c$, their coefficients can be approximated as follows

$${\Xi_D^R}^{-1}(\boldsymbol{k},\omega) \simeq \tilde{a}_D\epsilon + \tilde{b}_D\boldsymbol{k}^2 + \tilde{c}_D\omega \tag{5.37}$$

$$\tilde{a}_D = \left.\frac{\partial a_D}{\partial T}\right|_{T=T_c} = T\left.\frac{\partial Q_D^R(\boldsymbol{0},0)}{\partial T}\right|_{T=T_c}, \quad \tilde{b}_D = b_D|_{T=T_c}, \quad \tilde{c}_D = c_D|_{T=T_c}, \tag{5.38}$$

where ϵ is the reduced temperature for the 2SC-PT $\epsilon = (T - T_c)/T_c$. As is discussed in Appendix **??**, the coefficients a_D, b_D and c_D, can be calculated analytically at $M = 0$ and shown to take the following forms in the large Λ in the sense of $\Lambda \gg T_c + |\mu|$, respectively,

$$\tilde{a}_D = \frac{2N_f(N_c-1)}{\pi^2}\mu^2\left(1 + \frac{\pi^2}{3}\frac{T_c^2}{\mu^2}\right), \tag{5.39}$$

$$\tilde{b}_D = \frac{N_f(N_c-1)}{4\pi^2}\left(\frac{7\zeta(3)}{12\pi^2}\frac{\mu^2}{T_c^2} + \log\frac{\Lambda^2-\mu^2}{4T_c^2} + 2\gamma_{\mathrm{E}} - 2\log\frac{\pi}{4} - 1\right), \tag{5.40}$$

$$\mathrm{Re}\,\tilde{c}_D = -\frac{N_f(N_c-1)}{\pi^2}\mu\left(\log\frac{\Lambda^2-\mu^2}{4T_c^2} + 2\gamma_{\mathrm{E}} - 2\log\frac{\pi}{4} + 1\right), \tag{5.41}$$

$$\mathrm{Im}\,\tilde{c}_D = -\frac{N_f(N_c-1)}{4\pi}\frac{\mu^2}{T_c}. \tag{5.42}$$

Assuming further $T_c/\mu \ll 1$ and neglecting the logarithmic terms, we obtain

$$\tilde{a}_D = \frac{2N_f(N_c-1)}{\pi^2}\mu^2, \quad \tilde{b}_D = \frac{7N_f(N_c-1)\zeta(3)}{48\pi^4}\frac{\mu^2}{T_c^2}, \quad \tilde{c}_D = -i\frac{N_f(N_c-1)}{4\pi}\frac{\mu^2}{T_c}, \tag{5.43}$$

where in the last equation we neglected the real part of $\tilde{c}_D$ which is parametrically suppressed compared to the imaginary part. On account of Eq. (5.43), τ_D and ξ_D in Eq. (5.36) are reduced to

$$\xi_D \sim \frac{1}{T\epsilon^{1/2}}, \qquad \tau_D \sim \frac{1}{T\epsilon}. \tag{5.44}$$

This result shows that τ_D and ξ_D are divergent for $\epsilon \to 0$. Moreover, they do not depend on μ and G_D, which implies that the property of the soft mode is insensitive to μ and G_D. We note that the exponents of Eq. (5.44) are the same results as Eqs. (2.19) and (**??**). This means that the dynamics of

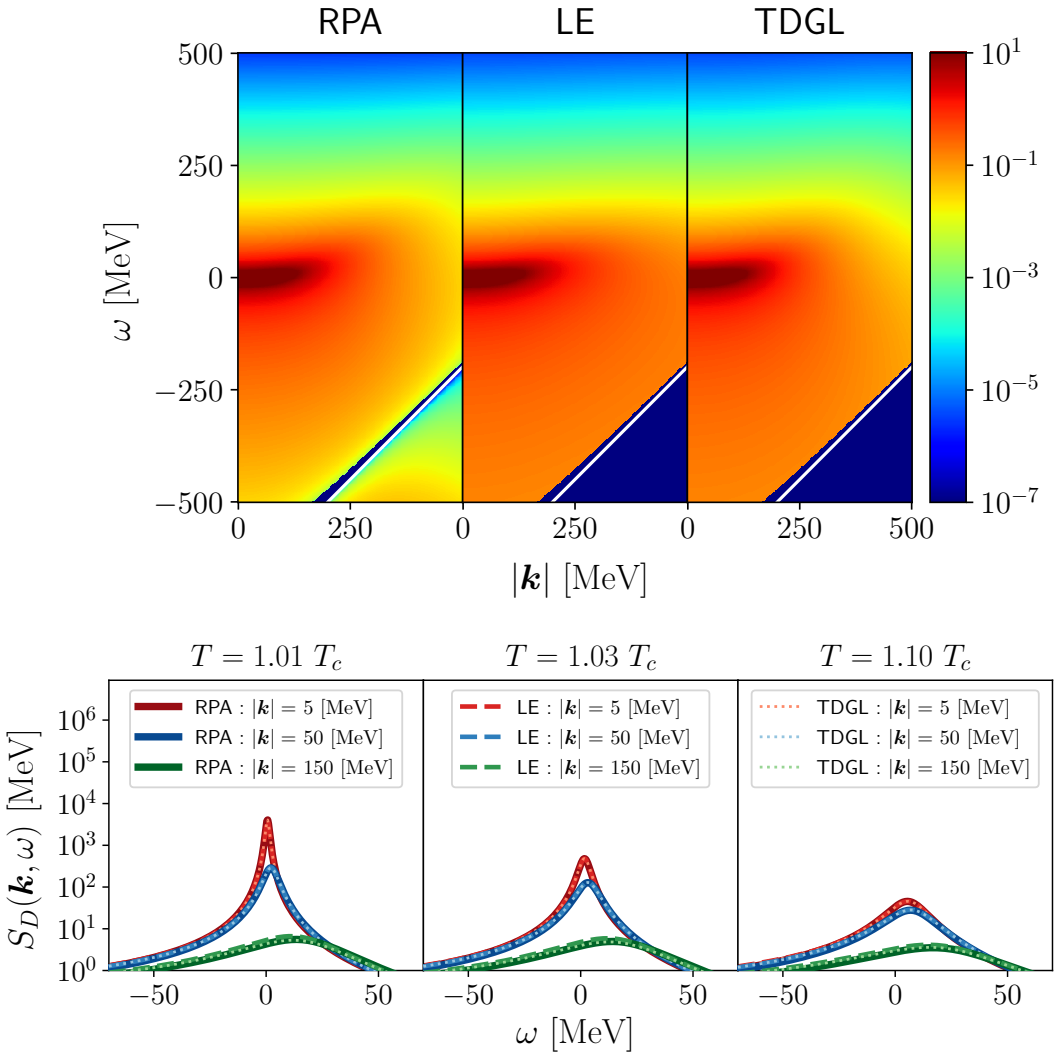

FIGURE 5.5: Comparison of the results of the dynamical structure factor of the 2SC-PT soft mode $S_D(\boldsymbol{k}, \omega)$ calculated by the RPA, the LE, and the TDGL approximations at $\mu = 350$ MeV with $G_D = 0.7G_S$. **Upper panels**: The contour map in the energy-momentum plane at $T = T_c$. **Lower panels**: The plots with $|\boldsymbol{k}| = 5$ MeV, 50 MeV, 150 MeV at $T = 1.01T_c$ (left), $1.03T_c$ (middle), $1.10T_c$ (right). In each panel, the solid, dashed, and dotted lines are the results by the RPA, the LE, and the TDGL approximations, respectively.

the 2SC-PT soft mode is described by the TDGL equation in Sec. 2.2.

Finally, let us confirm the validity of the LE and TDGL approximations for $\Xi_D^R(\boldsymbol{k}, \omega)$ numerically. In Fig. 5.5, the left, middle, and right panels show the contour maps of the dynamical structure factor $S_D(\boldsymbol{k}, \omega)$ at $T = T_c$ with $\mu = 350$ MeV calculated in the RPA, the LE approximation (5.32) and the TDGL approximation (5.37), respectively. One finds that the LE and TDGL approximations reproduce the result of the RPA well over a wide range of ω and $\boldsymbol{k}$. In the lower panel, we plot the results at $T = 1.01T_c$, $1.03T_c$, $1.10T_c$. One finds that the LE and TDGL approximation is valid when T goes away from T_c.

Now, we make one remark on the 2SC-PT soft mode. We have employed the MFA and the RPA to evaluate the phase transition of 2SC and soft modes, respectively. The existence of the soft mode is a generic feature of the second-order phase transition [44, 45]. Even if the phase transition is of first order, the development soft modes in the vicinity of the critical points is still expected when it is a weak first-order transition.

5.3.2 QCD-CP soft mode

Next, we perform a similar analysis for the soft mode of the QCD-CP. To this end, we adopt the LE approximation to $\Xi_S^R(\boldsymbol{k},\omega)$ as

$$\Xi_S^{R\,-1}(\boldsymbol{k},\omega) \simeq A_S(\boldsymbol{k}) + C_S(\boldsymbol{k})\omega, \tag{5.45}$$

$$A_S(\boldsymbol{k}) = G_S^{-1} + Q_S^R(\boldsymbol{k},0), \qquad C_S(\boldsymbol{k}) = \left.\frac{\partial Q_S^R(\boldsymbol{k},\omega)}{\partial\omega}\right|_{\omega=0}, \tag{5.46}$$

where $A_S(\boldsymbol{k})$ and $C_S(\boldsymbol{k})$ are found to be real and pure imaginary, respectively. Here, in contrast to the case of Eq. (5.32), we keep the $\boldsymbol{k}$ dependence of $C_S(\boldsymbol{k})$, since an explicit manipulation shows that $C_S(\boldsymbol{k})$ diverges as $1/|\boldsymbol{k}|$ for $\boldsymbol{k}\to\boldsymbol{0}$. This difference originates from the fact that $\Xi_S^R(\boldsymbol{k},\omega)$ is not analytic at the origin as discussed in Sec. 5.1. This is in contrast to that of $\Xi_D^R(\boldsymbol{k},\omega)$ where Eq. (5.32) is always applicable for $(\boldsymbol{k},\omega)$ near the origin. We also note that $\Xi_S^R(\boldsymbol{k},\omega)$ is discontinuous at $|\omega| = \lambda(|\boldsymbol{k}|,\bar{\Lambda}) \sim |\boldsymbol{k}|$. Therefore, the LE approximation (5.45) is applicable only for $|\omega| < \lambda(|\boldsymbol{k}|,\bar{\Lambda})$, i.e. the region (2) in the right panel of Fig. 5.2, which is within the space-like region. As was discussed already, however, the soft mode of QCD-CP has spectral support only in the space-like region, and hence this approximation is adequate for describing it. In this region, the term $C_S(\boldsymbol{k})\omega$ is finite. In Ref. [85], Eq. (5.45) is utilized for the analysis of the DPR near the QCD-CP.

To describe the low energy-momentum behavior, one would further expand the coefficients as

$$\Xi_S^{R\,-1}(\boldsymbol{k},\omega) \simeq\ a_S + b_S|\boldsymbol{k}|^2 + c_S\frac{\omega}{|\boldsymbol{k}|}, \tag{5.47}$$

$$a_S = \frac{1}{G_S} + Q_S^R(\boldsymbol{0},0), \quad b_S = \left.\frac{\partial Q_S^R(\boldsymbol{k},0)}{\partial\boldsymbol{k}^2}\right|_{|\boldsymbol{k}|=0}, \quad c_S = \left.\left(|\boldsymbol{k}|\left.\frac{\partial Q_S^R(\boldsymbol{k},\omega)}{\partial\omega}\right|_{\omega=0}\right)\right|_{|\boldsymbol{k}|\to 0}. \tag{5.48}$$

We refer to Eq. (5.47) as the TDGL approximation in analogy with Eq. (5.37). When we use both LE and TDGL approximation, it is assumed that $\Xi_S^R(\boldsymbol{k},\omega) = 0$ outside the region (2) in the right panel of Fig. 5.2.

The non-analyticity of $\Xi_S^R(\boldsymbol{k},\omega)$ at the origin also makes the behavior of the parameter a_S in Eq. (5.47) more complicated than in the case of the 2SC-PT. In the MFA, one finds that a_S goes to zero as $\epsilon_{\rm CP}\to 0$ where we have introduced

$$\epsilon_{\rm CP} = \sqrt{\left(\frac{T-T_{\rm CP}}{T_{\rm CP}}\right)^2 + \left(\frac{\mu-\mu_{\rm CP}}{\mu_{\rm CP}}\right)^2}. \tag{5.49}$$

However, the exponent is found to vary according to the path of the approach to zero;

$$a_S \sim \begin{cases} \epsilon_{\rm CP} & \text{parallel to the first-order line,} \\ \epsilon_{\rm CP}^{2/3} & \text{otherwise.} \end{cases} \tag{5.50}$$

This feature is actually generic in the mean-field theory and a simple account based on the Landau theory is given in Chap. 2. We will use Eq. (5.50) in Chaps. 7 and 8 to analyze the behavior of the DPR and the transport coefficients near the QCD-CP.

Figure 5.6 shows the dynamical structure factor $S_S(\boldsymbol{k},\omega)$ calculated by the RPA, the LE approximation (5.45) and the TDGL approximation (5.47), where the upper panel is the contour map in the ω-$|\boldsymbol{k}|$ plane at the critical point $(T,\mu) = (T_{CP},\mu_{CP})$, while the lower one shows the result of the different temperatures. One finds that both Eqs. (5.45) and (5.47) reproduce the result of the RPA near the origin of the ω-$|\boldsymbol{k}|$ plane in the relatively wide range of temperatures, while the former is slightly better than the latter. One also finds that the spectral density in the time-like region in the RPA that represents the mesonic excitation does not exist in the LE and TDGL results that are not

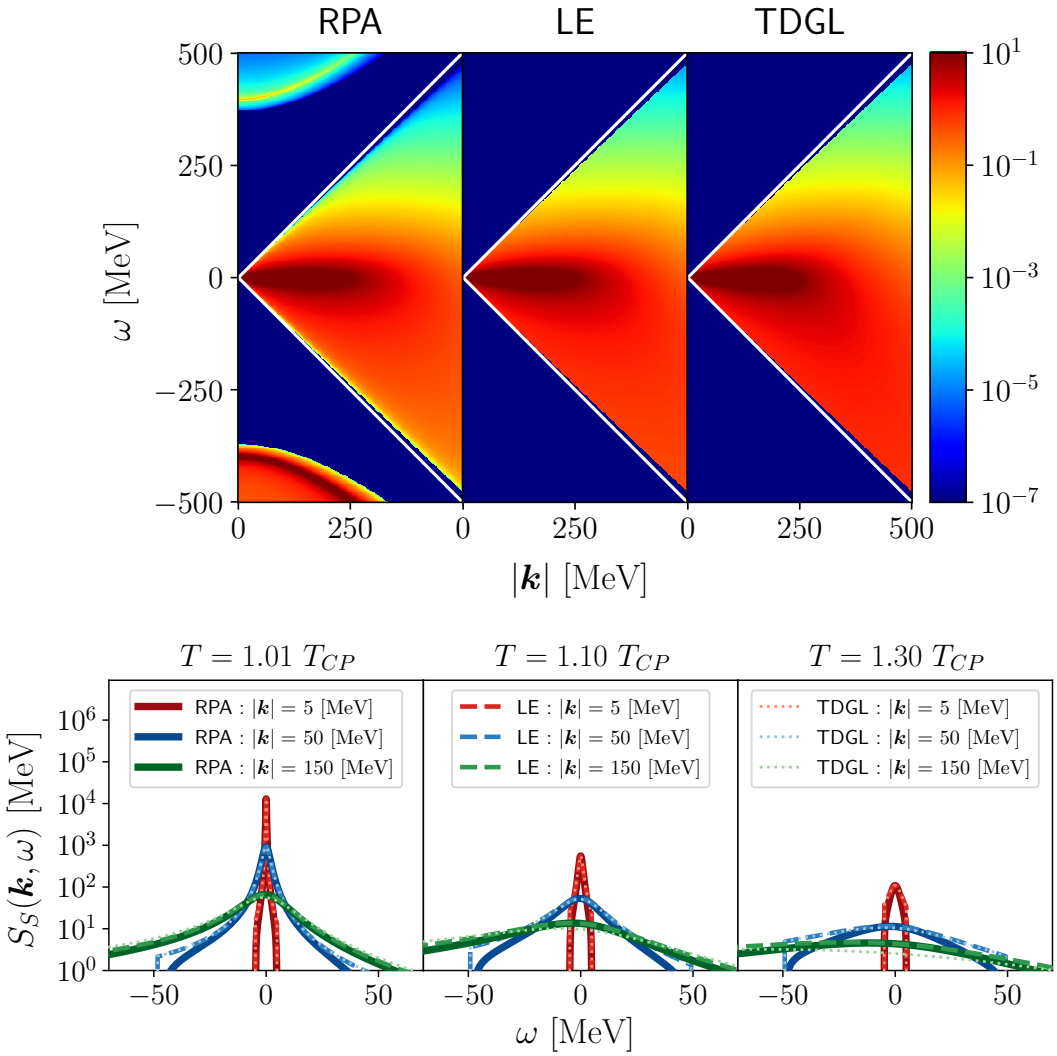

FIGURE 5.6: Comparison of the results of the dynamical structure factor of the QCD-CP soft mode $S_S(\boldsymbol{k},\omega)$ calculated by the RPA, the LE, and the TDGL approximations at $\mu = \mu_{CP}$ with $G_D = 0.7G_S$. **Upper panel**: The contour map in the energy-momentum plane at $T = T_{CP}$. **Lower panel**: The plots with $|\boldsymbol{k}| = 5$ MeV, 50 MeV, 150 MeV at $T = 1.01T_{CP}$, $1.10T_{CP}$, $1.30T_{CP}$. In each panel, the solid, dashed, and dotted lines are the results by the RPA, the LE, and the TDGL approximations, respectively.

applicable to the time-like region. However, since the mesonic excitation stays massive at the CP, it does not play a significant role in describing the critical phenomena. In the next chapters, we use Eqs. (5.45) and (5.47) for the analysis of the transport coefficients and the DPR.

Chapter 6

Modifications of photon self-energy due to the soft modes

In this chapter, we calculate the photon self-energy $\tilde{\Pi}^{\mu\nu}(k)$ incorporating the effects of the 2SC-PT and QCD-CP soft modes whose properties have been discussed in the previous sections. In particular, we derive the explicit form of the imaginary part of the spatial components of the retarded function, $\mathrm{Im}\Pi^{Rij}(\boldsymbol{k},\omega)$, which describes the dilepton production rate and the transport coefficients as described later. The formalism in this section is almost the same as our previous studies [84, 85] when the LE approximation (5.32) or (5.45) is adopted for the propagator of the soft modes. In the present study, the formalism is extended to the case with the TDGL approximation. Detailed procedure of manipulations skipped in Refs. [84, 85] are also elucidated. The parallel description for the cases of the 2SC-PT and QCD-CP is also useful for clarifying their similarity and difference.

In our study, the photon self-energy $\tilde{\Pi}^{\mu\nu}(k)$ consists of three contributions

$$\tilde{\Pi}^{\mu\nu}(k) = \tilde{\Pi}^{\mu\nu}_{\mathrm{free}}(k) + \tilde{\Pi}^{\mu\nu}_{D}(k) + \tilde{\Pi}^{\mu\nu}_{S}(k), \tag{6.1}$$

where $\tilde{\Pi}^{\mu\nu}_{D}(k)$ and $\tilde{\Pi}^{\mu\nu}_{S}(k)$ are the contributions from the soft modes of the 2SC-PT and QCD-CP, respectively, that will be constructed so as to satisfy the Ward-Takahashi (WT) identity below and

$$\tilde{\Pi}^{\mu\nu}_{\mathrm{free}}(k) = N_c(e_u^2+e_d^2)\int_p \mathrm{Tr}_d[\gamma^\mu \mathcal{G}_0(p+k)\gamma^\nu \mathcal{G}_0(p)], \tag{6.2}$$

is the self-energy of the free-quark system, with the electric charge of up (down) quark $e_u = 2|e|/3$ ($e_d = -|e|/3$), and the charge of electrons e. The explicit form of Eq. (6.2) is given in Sec. 6.1. Since $k_\mu \tilde{\Pi}^{\mu\nu}_{\mathrm{free}}(k) = 0$, the total photon self-energy $\tilde{\Pi}^{\mu\nu}(k)$ satisfies the WT identity

$$k_\mu \tilde{\Pi}^{\mu\nu}(k) = 0. \tag{6.3}$$

We emphasize that the analysis of transport coefficients is possible since the photon self-energies in this thesis satisfies with the Ward identity (6.3).

6.1 Contribution of free quark gases

Since the transport coefficients and DPR needs $g_{\mu\nu}\Pi^{R\mu\nu}(k)$, we calculate $g_{\mu\nu}\Pi^{R\mu\nu}_{\mathrm{free}}(k)$ from Eq. (6.2). As in Sec. 5.1, we obtain [87, 97]

$$\begin{aligned} g_{\mu\nu}\tilde{\Pi}^{\mu\nu}_{\mathrm{free}}(\boldsymbol{k}, i\nu_n) = N_c(e_u^2+e_d^2)\int \frac{d^3p}{(2\pi)^3}\frac{1}{e_1 e_2} \\ \times \sum_{s,t=\pm} st\left\{\left[se_1 - \frac{1}{2}\frac{(se_1-te_2)^2-\boldsymbol{k}^2+2M^2}{se_1-te_2+i\nu_n}\right]\tanh\frac{se_1-\mu}{2T}\right. \\ \left. + \left[te_2 - \frac{1}{2}\frac{(te_2-se_1)^2-\boldsymbol{k}^2+2M^2}{te_2-se_1-i\nu_n}\right]\tanh\frac{te_2-\mu}{2T}\right\}, \end{aligned} \tag{6.4}$$

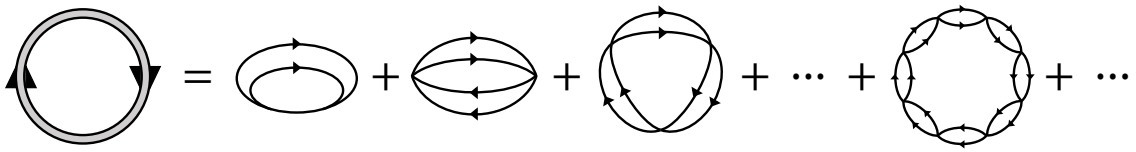

FIGURE 6.1: Contribution of the diquark soft mode to the thermodynamic potential.

where $e_1 = \sqrt{\boldsymbol{p}^2 + M^2}$ and $e_2 = \sqrt{(\boldsymbol{p}+\boldsymbol{k})^2 + M^2}$. The integral in Eq. (6.4) has no cutoff, i.e. the limit $\Lambda \to \infty$ is taken in Eqs. (5.17)

$$\int \frac{d^3p}{(2\pi)^3}\frac{1}{e_1 e_2} = \frac{1}{2(2\pi)^2|\boldsymbol{k}|}\int_{\lambda(|\boldsymbol{k}|,0)}^{\infty} dE_1 \int_{-\lambda(|\boldsymbol{k}|,E_1)}^{+\lambda(|\boldsymbol{k}|,E_1)} dE_2, \tag{6.5}$$

Then, we obtain the imaginary part of the retarded function

$$\begin{aligned} g_{\mu\nu}\mathrm{Im}\Pi^{R\mu\nu}_{\mathrm{free}}(\boldsymbol{k},\omega) &= -\frac{N_c(e_u^2+e_d^2)}{16\pi|\boldsymbol{k}|}\int_{\lambda(|\boldsymbol{k}|,0)}^{\infty} dE_1 \int_{-\lambda(|\boldsymbol{k}|,E_1)}^{+\lambda(|\boldsymbol{k}|,E_1)} dE_2 \\ &\quad \times \sum_{s,t=\pm}\Bigg\{ s(E_1^2 - \boldsymbol{k}^2 + 2M^2)\tanh\frac{E_1 + t(E_2 - 2s\mu)}{4T}\delta(E_1 + s\omega) \\ &\qquad - s(E_2^2 - \boldsymbol{k}^2 + 2M^2)\tanh\frac{E_2 + t(E_1 - 2s\mu)}{4T}\delta(E_2 + s\omega)\Bigg\} \\ &= \frac{N_c(e_u^2+e_d^2)T}{2\pi}\frac{\omega^2 - \boldsymbol{k}^2 + 2M^2}{|\boldsymbol{k}|}\Bigg\{\theta(|\omega| - \lambda(|\boldsymbol{k}|,0))F(\omega,\lambda(|\boldsymbol{k}|,\omega)) \\ &\qquad + \theta(|\boldsymbol{k}| - |\omega|)\left[F(\omega,\lambda(|\boldsymbol{k}|,\omega)) - \frac{\omega}{T}\right]\Bigg\}, \end{aligned} \tag{6.6}$$

where$\lambda(|\boldsymbol{k}|,\omega)$ and $F_S(\omega,x)$ have been given by Eqs. (5.18) and (5.25), respectively. As one sees, in Eq. (6.6), the first and second terms in the wavy bracket correspond to the time-like ($|\omega| > \lambda(|\boldsymbol{k}|,0)$) and space-like ($|\boldsymbol{k}| < |\omega|$) regions. Of these, only the contribution of time-like region is needed the analyses of the transport coefficients and DPR.

6.2 Case of 2SC-PT soft mode

6.2.1 Construction scheme

For the construction of photon self-energy including the 2SC-PT soft modes, it is reasonable to assume that $\tilde{\Pi}^{\mu\nu}_D(k)$ solely satisfies the WT identity,

$$k_\mu \tilde{\Pi}^{\mu\nu}_D(k) = 0. \tag{6.7}$$

To satisfy this condition, we start from the diagrams representing the lowest-order contribution of the soft mode to the thermodynamic potential

$$\Omega_D = 3\int_p \ln[G_D\tilde{\Xi}_D^{-1}(p)], \tag{6.8}$$

i.e. the one-loop diagram of $\tilde{\Xi}_D(k)$ shown in Fig. 6.1, where the overall coefficient 3 comes from three antisymmetric channels of the diquark field.

The photon self-energy satisfying Eq. (6.7) is then constructed by attaching electromagnetic vertices to two points of quark lines in Ω_D. This procedure leads to four types of diagrams shown in Fig. 6.2, which are called (a) Aslamazov-Larkin (AL) [98], (b) Maki-Thompson (MT) [99, 100] and (c, d) density of states (DOS) terms [45], respectively, in the theory of metallic superconductivity.

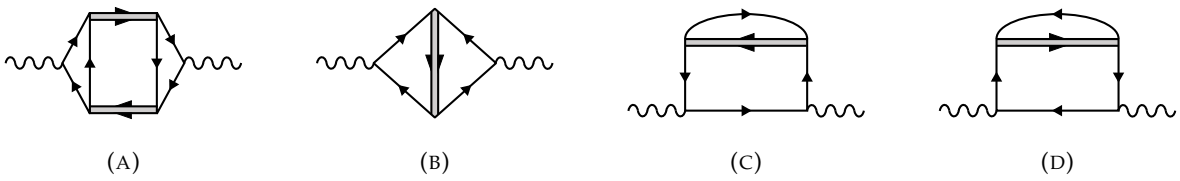

(A) (B) (C) (D)

FIGURE 6.2: Diagrammatic representations of the Aslamazov-Larkin (a), Maki-Thompson (b) and density of states (c, d) terms with the 2SC soft modes. The single, double, and wavy lines are quarks, soft modes, and photons, respectively.

In the case of metallic superconductivity, these terms at the vanishing energy/momentum limit are known to describe the anomolous enhancement of the electric conductivity above the critical temperature [45, 44]. The photon self-energy is then given by

$$\tilde{\Pi}^{\mu\nu}_D(k) = \tilde{\Pi}^{\mu\nu}_{\mathrm{AL},D}(k) + \tilde{\Pi}^{\mu\nu}_{\mathrm{MT},D}(k) + \tilde{\Pi}^{\mu\nu}_{\mathrm{DOS},D}(k), \tag{6.9}$$

where $\tilde{\Pi}^{\mu\nu}_{\mathrm{AL},D}(k)$, $\tilde{\Pi}^{\mu\nu}_{\mathrm{MT},D}(k)$ and $\tilde{\Pi}^{\mu\nu}_{\mathrm{DOS},D}(k)$ denote the respective contributions

$$\tilde{\Pi}^{\mu\nu}_{\mathrm{AL},D}(k) = 3\int_q \tilde{\Gamma}^{\mu}_D(q,q+k)\tilde{\Xi}_D(q+k)\tilde{\Gamma}^{\nu}_D(q+k,q)\tilde{\Xi}_D(q), \tag{6.10}$$

$$\tilde{\Pi}^{\mu\nu}_{\mathrm{MT},D}(k) = 3\int_q \tilde{\Xi}_D(q)\ \mathcal{R}^{\mu\nu}_{\mathrm{MT},D}(q,k), \tag{6.11}$$

$$\tilde{\Pi}^{\mu\nu}_{\mathrm{DOS},D}(k) = 3\int_q \tilde{\Xi}_D(q)\ \mathcal{R}^{\mu\nu}_{\mathrm{DOS},D}(q,k), \tag{6.12}$$

where $q = (\boldsymbol{q}, i\nu_n)$ is the four-momentum of the soft mode. The vertex functions $\tilde{\Gamma}^{\mu}_D(q,k)$, $\mathcal{R}^{\mu\nu}_{\mathrm{MT},D}(q,k)$ and $\mathcal{R}^{\mu\nu}_{\mathrm{DOS},D}(q,k)$ in Eqs. (6.10)–(6.12) are given by

$$\tilde{\Gamma}^{\mu}_D(q,q+k) = 4(N_c-1)e_\Delta \int_p \mathrm{Tr}[\mathcal{G}_0(p)\gamma^\mu\mathcal{G}_0(p+k)\mathcal{G}_0(q-p)], \tag{6.13}$$

$$\mathcal{R}^{\mu\nu}_{\mathrm{MT},D}(q,k) = 8(N_c-1)e_u e_d \int_p \mathrm{Tr}[\mathcal{G}_0(p)\gamma^\mu\mathcal{G}_0(p+k)\mathcal{G}_0(q-p-k)\gamma^\nu\mathcal{G}_0(q-p)], \tag{6.14}$$

$$\mathcal{R}^{\mu\nu}_{\mathrm{DOS},D}(q,k) = 4(N_c-1)(e_u^2+e_d^2)\sum_{s=\pm}\int_p \mathrm{Tr}[\mathcal{G}_0(p)\gamma^\mu\mathcal{G}_0(p+sk)\gamma^\nu\mathcal{G}_0(p)\mathcal{G}_0(q-p)], \tag{6.15}$$

with $e_\Delta = e_u + e_d$ being the electric charge of diquarks. From Eqs. (6.13)–(6.15), one can easily show that these vertices satisfy the WT identities

$$k_\mu\tilde{\Gamma}^{\mu}_D(q,q+k) = e_\Delta[\tilde{\Xi}_D^{-1}(q+k) - \tilde{\Xi}_D^{-1}(q)], \tag{6.16}$$

$$k_\mu\mathcal{R}^{\mu\nu}_D(q,k) = e_\Delta[\tilde{\Gamma}^{\nu}_D(q-k,q) - \tilde{\Gamma}^{\nu}_D(q,q+k)], \tag{6.17}$$

with $\mathcal{R}^{\mu\nu}_D(q,k) = \mathcal{R}^{\mu\nu}_{\mathrm{MT},D}(q,k) + \mathcal{R}^{\mu\nu}_{\mathrm{DOS},D}(q,k)$. Using Eqs. (6.16) and (6.17), one can also show that Eq. (6.7) is satisfied easily.

We note that the above construction of $\tilde{\Pi}^{\mu\nu}(k)$ corresponds to the linear approximation of the soft modes in the sense that the interaction between the soft modes is not included. This feature comes from the fact that Eq. (6.8) is composed only of a one-loop diagram of $\tilde{\Xi}_D(k)$. The linear approximation is eventually violated as T approaches T_c as the amplitude of the diquark fluctuations grows. Our analysis in the following is not applicable to such a range of T. To extend the analysis, we may start from the thermodynamic potential with multiple loops of $\tilde{\Xi}_D(k)$The properties of the soft mode will also be modified at such T range.

6.2.2 Approximation to vertices

The calculation of $\tilde{\Pi}_D^{\mu\nu}(k)$ involves three-loop diagrams, and it is a difficult task to compute these diagrams exactly. We thus need an approximate method for them. Since we are interested in the critical phenomena of the 2SC-PT, the approximations should be introduced to describe the effects of the soft modes at low energy-momentum regions well.

For the first step of such procedures, we employ the effective formulae: the LE approximation (5.32) and the TDGL approximation (5.37), for the T-matrix $\Xi_D^R(\boldsymbol{k},\omega)$. As discussed in the previous chapter, these formulas reproduce the low energy-momentum behavior of the soft modes and thus are appropriate for our purpose. Once Eqs. (5.32) or (5.37) are employed for $\Xi_D^R(\boldsymbol{k},\omega)$, the vertices $\tilde{\Gamma}_D^{\mu}(q,q+k)$ and $\mathcal{R}_D^{\mu\nu}(q,k)$ must satisfy the WT identities (6.16) and (6.17) in accordance with the effective form of $\Xi_D^R(\boldsymbol{k},\omega)$. To construct such vertices that are valid in the low energy-momentum region, we resort to their WT identities, instead of directly calculating Eqs. (6.13)–(6.15).

We start from the vertex of the AL term $\tilde{\Gamma}_D^{\mu}(q,q+k)$. We use the analytic continuation of the LE approximation (5.32) that is given by

$$\tilde{\Xi}_D(q) = A_D(\boldsymbol{q}) + \mathcal{C}_D(q_0) \quad \text{with} \quad \mathcal{C}_D(q_0) = \begin{cases} (C_D q_0)^* & \mathrm{Im} q_0 > 0, \\ 0 & \mathrm{Im} q_0 = 0, \\ C_D q_0 & \mathrm{Im} q_0 < 0, \end{cases} \tag{6.18}$$

where it is noted that $A_D(\boldsymbol{q})$ takes the same form in the entire complex energy (q_0) plane since it is independent of the energy in this approximation. Substituting Eq. (6.18) into the right-hand side of Eq. (6.16), one obtains

$$\begin{aligned} &\tilde{\Xi}_D^{-1}(\boldsymbol{q}+\boldsymbol{k}, i\nu_n + i\nu_l) - \tilde{\Xi}_D^{-1}(\boldsymbol{q}, i\nu_n) \\ &\qquad = [\mathcal{C}_D(i\nu_n + i\nu_l) - \mathcal{C}_D(i\nu_n)] + A_D(\boldsymbol{q}+\boldsymbol{k}) - A_D(\boldsymbol{q}) \\ &\qquad = [\mathcal{C}_D(i\nu_n + i\nu_l) - \mathcal{C}_D(i\nu_n)] + A_D^{(1)}(\boldsymbol{q}+\boldsymbol{k}, \boldsymbol{q})(2\boldsymbol{q}+\boldsymbol{k})\cdot\boldsymbol{k}, \end{aligned} \tag{6.19}$$

where

$$A_D^{(1)}(\boldsymbol{q}_1, \boldsymbol{q}_2) = \frac{A_D(\boldsymbol{q}_1) - A_D(\boldsymbol{q}_2)}{|\boldsymbol{q}_1|^2 - |\boldsymbol{q}_2|^2}, \tag{6.20}$$

is a real number since $A_D(\boldsymbol{q})$ is real. In Eq. (6.19), one sees that only the second term has the $\boldsymbol{k}$ dependence. We thus identify the first and second terms in Eq. (6.19) as $k_0\tilde{\Gamma}_D^0(q,q+k)$ and $k_i\tilde{\Gamma}_D^i(q,q+k)$ in Eq. (6.16), respectively, so that

$$\tilde{\Gamma}_D^0(q,q+k) = e_\Delta[\mathcal{C}_D(i\nu_n + i\nu_l) - \mathcal{C}_D(i\nu_n)]/i\nu_l, \tag{6.21}$$

$$\tilde{\Gamma}_D^i(q,q+k) = \Gamma_D^i(\boldsymbol{q},\boldsymbol{q}+\boldsymbol{k}) = -e_\Delta A_D^{(1)}(\boldsymbol{q}+\boldsymbol{k},\boldsymbol{q})(2q+k)^i, \tag{6.22}$$

where $\tilde{\Gamma}_D^0(q,q+k)$ and $\tilde{\Gamma}_D^i(q,q+k)$ are complex and real numbers, respectively. Similarly, when one employs the TDGL approximation (5.37), the spatial component is approximated as

$$\Gamma_D^i(\boldsymbol{q},\boldsymbol{q}+\boldsymbol{k}) = -e_\Delta b_D(2q+k)^i, \tag{6.23}$$

while the temporal component $\tilde{\Gamma}_D^0(q,q+k)$ is the same as Eq. (6.21) because of $c_D = C_D$ as shown in Eq. (5.35). We note that Eq. (6.23) is consistent with Eq. (6.22) in the small $\boldsymbol{k}$ limit. Also, Eq. (6.21) is obtained by substituting $\boldsymbol{k} = 0$ into Eq. (6.16). In the analysis of the DPR and transport coefficients, we do not use Eq. (6.21) as described in Chap. 8 and 7.

In general, the functional form of the vertex cannot be uniquely determined solely by the WT identity. Therefore, the vertices determined in the above should be taken as one of the functional forms that are consistent with the WT identity. However, the approximation (6.21)–(6.23) is quite

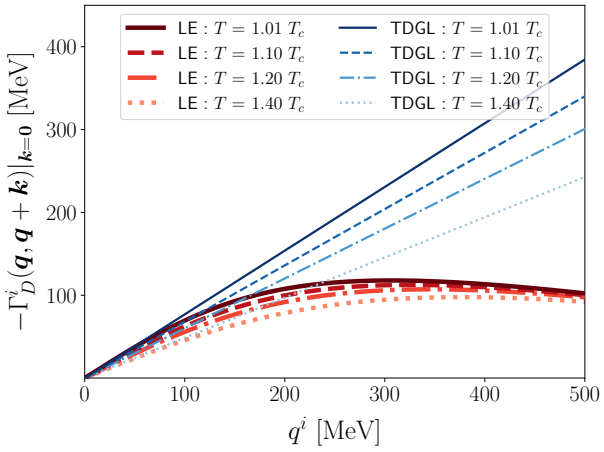

FIGURE 6.3: Momentum dependence of the vertex in the AL term $\tilde{\Gamma}^i_D(q, q+k)$ at $\mu = 350$ MeV and $G_D = 0.7\ G_S$ with $q^i = |\boldsymbol{q}|$ and $|\boldsymbol{k}| = 0$ for $T/T_c = 1.01$, 1.10, 1.20, and 1.40. The solid (red) and dashed (blue) lines are corresponding to the results by the LE approximation and the TDGL approximation, respectively.

adequate in the small k^μ region, as we will see: Equation (6.13) in this limit reads

$$\lim_{k_\mu \to 0} \tilde{\Gamma}^\mu_D(q, q+k) = 4(N_c - 1)\, e_\Delta \int_p \mathrm{Tr}_d[\mathcal{G}_0(p)\gamma^\mu \mathcal{G}_0(p)\mathcal{G}_0(q-p)] = e_\Delta \frac{\partial \tilde{\Xi}^{-1}_D(q)}{\partial q_\mu}. \tag{6.24}$$

Plugging Eq. (5.32) into Eq. (6.24), one finds

$$\lim_{k_\mu \to 0} \tilde{\Gamma}^0_D(q, q+k) = e_\Delta \frac{\partial \mathcal{Q}_D(\boldsymbol{q}, q_0)}{\partial q_0} = e_\Delta \mathcal{C}_D(q_0), \tag{6.25}$$

$$\lim_{k_\mu \to 0} \tilde{\Gamma}^i_D(q, q+k) = e_\Delta \frac{\partial \mathcal{Q}_D(\boldsymbol{q}, q_0)}{\partial q_i} = -e_\Delta \frac{\partial A_D(\boldsymbol{q})}{\partial |\boldsymbol{q}|^2} 2q^i, \tag{6.26}$$

In the small k^μ limit, Eq. (6.21) is equal to Eq. (6.25), and Eq. (6.22) coincides with Eq. (6.26). Thereby, one can see that the approximation for $\tilde{\Gamma}^\mu_D(q, q+k)$ based on the LE approximation (6.21) and (6.22) are justified in the low-k^μ region. Moreover, the validity of the TDGL approximation (6.23) are confirmed in the low-q^μ region in addition to the low-k^μ region.

To compare the behaviors of $\Gamma^i_D(\boldsymbol{q}, \boldsymbol{q}+\boldsymbol{k})$ in the LE and TDGL approximations, Eqs. (6.22) and (6.23), in Fig. 6.3 we show the momentum dependence of $\Gamma^i_D(\boldsymbol{q}, \boldsymbol{q})$ for several temperatures, where $q^i = |\boldsymbol{q}|$. The figure shows that the difference between the LE and TDGL approximations becomes more significant as $|\boldsymbol{q}|$ becomes larger; while the latter is increasing linearly, the former is suppressed at large $|\boldsymbol{q}|$. This result indicates that the TDGL approximation tends to overestimate the non-critical contribution to $\tilde{\Pi}^{\mu\nu}_{\mathrm{AL},D}(k)$. The difference becomes more prominent as T goes away from T_c as the strength of the soft mode is scattered in a wide range of energy-momentum. Owing to the difference in the degrees of the approximation, the result in the LE approximation should be more reliable. Nevertheless, the TDGL approximation should be fine for exploring the limiting behavior of the DPR, σ and τ_σ in the vicinity of the critical temperature.

We then apply the same procedure to the vertices of the MT and DOS terms $\mathcal{R}^{\mu\nu}_D(q, k)$. Using the WT-identity (6.17) and the approximations for $\tilde{\Gamma}^\mu_D(q, q+k)$, $\mathcal{R}^{\mu\nu}_D(q, k)$ is determined as

$$\mathcal{R}^{00}_D(q, k) = -e_\Delta \frac{\tilde{\Gamma}^0_D(q, q+k) - \tilde{\Gamma}^0_D(q-k, q)}{k_0}, \tag{6.27}$$

$$\mathcal{R}^{ij}_D(q, k) = R^{ij}_D(\boldsymbol{q}, \boldsymbol{k}) = 4e_\Delta \frac{\Gamma^i_D(\boldsymbol{q}, \boldsymbol{q}+\boldsymbol{k}) - \Gamma^i_D(\boldsymbol{q}-\boldsymbol{k}, \boldsymbol{q})}{(\boldsymbol{q}+\boldsymbol{k})^2 - (\boldsymbol{q}-\boldsymbol{k})^2}\, q^j, \tag{6.28}$$

where $\mathcal{R}_D^{00}(q,k)$ and $\mathcal{R}_D^{ij}(q,k)$ are complex and real. These results can be obtained in the use of either the LE approximation or the TDGL approximation. Equations (6.27) and (6.28) are used for the analysis of the MT and DOS terms. In the analysis of the spatial components of the MT and DOS terms, however, one finds that the result satisfies

$$\mathrm{Im}\Pi^{Rij}_{\mathrm{DOS},D}(\boldsymbol{k},\omega)+\mathrm{Im}\Pi^{Rij}_{\mathrm{DOS},D}(\boldsymbol{k},\omega)=0, \tag{6.29}$$

In fact, Eq (6.29) is derived as follows,

$$\begin{aligned}
\tilde{\Pi}^{ij}_{\mathrm{MT},D}(k)+\tilde{\Pi}^{ij}_{\mathrm{DOS},D}(k) &= 3\int_q \tilde{\Xi}_D(q)\mathcal{R}^{ij}_D(q,k)\\
&= 3\int\frac{d^3p}{(2\pi)^3}R^{ij}_D(\boldsymbol{q},\boldsymbol{k})\oint_C\frac{dq_0}{2\pi i}\frac{\coth q_0/2T}{2}\tilde{\Xi}_D(\boldsymbol{q},q_0)\\
&= 3\int\frac{d^3p}{(2\pi)^3}R^{ij}_D(\boldsymbol{q},\boldsymbol{k})\int\frac{d\omega'}{2\pi i}\frac{\coth q_0/2T}{2}\left(\Xi^R_D(\boldsymbol{q},\omega')-\Xi^A_D(\boldsymbol{q},\omega')\right)\\
&= 3\int\frac{d^3p}{(2\pi)^3}R^{ij}_D(\boldsymbol{q},\boldsymbol{k})\int\frac{d\omega'}{2\pi}\coth\frac{q_0}{2T}\mathrm{Im}\Xi^R_D(\boldsymbol{q},\omega').
\end{aligned} \tag{6.30}$$

Here, in the second equality we used the fact that $\mathcal{R}^{ij}_D(q,k)=R^{ij}_D(\boldsymbol{q},\boldsymbol{k})$ does not depend on $q_0(=i\nu_n)$ and $k_0(=i\nu_l)$ and transformed the Matsubara sum into the integral over the contour C on the complex-energy plane that encircles the imaginary axis. In the third equality, the contour is deformed so as to avoid the cut in $\tilde{\Xi}_D(q)$ on the real axis with $\Xi^A_D(\boldsymbol{q},\omega)=\Xi^{R*}_D(\boldsymbol{q},\omega)$. One can find that the last line is real since this expression consists only of real functions. Moreover, Eq. (6.30) shows that it does not depend on k_0. Therefore, its analytic continuation is also real, which proves Eq. (6.29). A similar argument on the MT and DOS terms in the metallic superconductivity is found in Ref. [45].

6.2.3 Explicit form of AL term

In this section, we calculate the spatial component of the AL term since only the imaginary part of its retarded function is necessary for the analysis of the dilepton production rate and the transport coefficients as described in Chaps. 7 and 8.

Firstly, the spatial component of Eq. (6.10) is obtained within both LE approximation (5.32), (6.22), and TDGL approximation (5.37), (6.23),

$$\begin{aligned}
\tilde{\Pi}^{ij}_{\mathrm{AL},D}(k) &= 3\int\frac{d^3q}{(2\pi)^3}\,\tilde{\Gamma}^i_D(q,q+k)\,\tilde{\Gamma}^j_D(q+k,q)\,T\sum_n\tilde{\Xi}_D(\boldsymbol{q}+\boldsymbol{k},i\nu_n+i\nu_l)\,\tilde{\Xi}_D(\boldsymbol{q},i\nu_n)\\
&= 3\int\frac{d^3q}{(2\pi)^3}\,\Gamma^i_D(\boldsymbol{q},\boldsymbol{q}+\boldsymbol{k})\,\Gamma^j_D(\boldsymbol{q}+\boldsymbol{k},\boldsymbol{q})\\
&\qquad\times\frac{1}{2}\oint_C\frac{dq_0}{2\pi i}\,\coth\frac{q_0}{2T}\,\tilde{\Xi}_D(\boldsymbol{q}+\boldsymbol{k},q_0+i\nu_l)\,\tilde{\Xi}_D(\boldsymbol{q},q_0)\\
&= 3\int\frac{d^3q}{(2\pi)^3}\,\Gamma^i_D(\boldsymbol{q},\boldsymbol{q}+\boldsymbol{k})\,\Gamma^j_D(\boldsymbol{q}+\boldsymbol{k},\boldsymbol{q})\\
&\qquad\times\frac{1}{2}\Big[\int\frac{d\omega'}{2\pi i}\,\coth\frac{\omega'}{2T}\,\Xi^R_D(\boldsymbol{q}+\boldsymbol{k},\omega'+i\nu_l)\,\Xi^R_D(\boldsymbol{q},\omega')\\
&\qquad\quad-\int\frac{d\omega'}{2\pi i}\,\coth\frac{\omega'}{2T}\,\Xi^R_D(\boldsymbol{q}+\boldsymbol{k},\omega'+i\nu_l)\,\Xi^A_D(\boldsymbol{q},\omega')\\
&\qquad\quad-\int\frac{d\omega'}{2\pi i}\,\coth\frac{\omega'}{2T}\,\Xi^R_D(\boldsymbol{q}+\boldsymbol{k},\omega')\,\Xi^A_D(\boldsymbol{q},\omega'-i\nu_l)\\
&\qquad\quad-\int\frac{d\omega'}{2\pi i}\,\coth\frac{\omega'}{2T}\,\Xi^A_D(\boldsymbol{q}+\boldsymbol{k},\omega')\,\Xi^A_D(\boldsymbol{q},\omega'-i\nu_l)\Big],
\end{aligned} \tag{6.31}$$

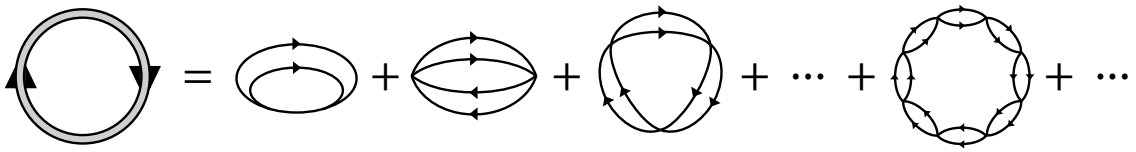

FIGURE 6.4: Contribution of the p-h soft mode to the thermodynamic potential.

where the manipulation in each equality is as follows:

- First: $\tilde{\Gamma}^i_D(q, q+k)$ and $\tilde{\Gamma}^i_D(q+k, q)$ can be put outside the sum of the Matsubara frequency $i\nu_n$ since it is independent of $i\nu_n$ in both approximations.
- Second: the sum of $i\nu_n$ is replaced by the residue integration through Eq. (3.24) and the contour C surrounds the poles of $\coth(q_0/2T)$.
- Third: the contour C is deformed so as to avoid the cut in the propagators $\tilde{\Xi}_D(\boldsymbol{q}+\boldsymbol{k}, q_0+i\nu_l)$ and $\tilde{\Xi}_D(\boldsymbol{q}, q_0)$ and the analytic continuations of their propagators are taken.

Then, its imaginary part is given by

$$\begin{aligned}
\mathrm{Im}\Pi^{Rij}_{\mathrm{AL},D}(\boldsymbol{k},\omega) &= 3\int\frac{d^3q}{(2\pi)^3}\,\Gamma^i_D(\boldsymbol{q},\boldsymbol{q}+\boldsymbol{k})\,\Gamma^j_D(\boldsymbol{q}+\boldsymbol{k},\boldsymbol{q})\int\frac{d\omega'}{2\pi}\coth\frac{\omega'}{2T} \\
&\quad\times\left\{\mathrm{Im}\Xi^R_D(\boldsymbol{q}+\boldsymbol{k},\omega'+\omega)\mathrm{Im}\Xi^R_D(\boldsymbol{q},\omega')-\mathrm{Im}\Xi^R_D(\boldsymbol{q}+\boldsymbol{k},\omega')\mathrm{Im}\Xi^R_D(\boldsymbol{q},\omega'-\omega)\right\} \\
&= 3\int\frac{d^3q}{(2\pi)^3}\,\Gamma^i_D(\boldsymbol{q}+\boldsymbol{k},\boldsymbol{q})\,\Gamma^j_D(\boldsymbol{q}+\boldsymbol{k},\boldsymbol{q})\int\frac{d\omega'}{2\pi}\coth\frac{\omega'}{2T} \\
&\quad\times\mathrm{Im}\Xi^R_D(\boldsymbol{q}+\boldsymbol{k},\omega')\left\{\mathrm{Im}\Xi^R_D(\boldsymbol{q},\omega'+\omega)-\mathrm{Im}\Xi^R_D(\boldsymbol{q},\omega'-\omega)\right\},
\end{aligned}\tag{6.32}$$

where in the first equality, the relation $\Xi^A_D(\boldsymbol{p},\omega') = \Xi^{R\,*}_D(\boldsymbol{p},\omega')$ is used, and in the second, the variable transformation for $\boldsymbol{q}$ is carried out and the following property is used: $\Gamma^i_D(\boldsymbol{q},\boldsymbol{q}+\boldsymbol{k}) = \Gamma^i_D(\boldsymbol{q}+\boldsymbol{k},\boldsymbol{q})$ and $\Gamma^i_D(-\boldsymbol{q}-\boldsymbol{k},-\boldsymbol{q}) = \Gamma^i_D(\boldsymbol{q}+\boldsymbol{k},\boldsymbol{q})$. The integration range of Eq. (6.32) is determined by the limitations of $\mathrm{Im}Q^R_D$ that $\mathrm{Im}\Xi^R_D$ has since both LE and TDGL approximations are valid for the region that the strength of the soft mode exists as described in Sec. 5.3.1.

It is noteworthy that the 2SC-PT soft modes that are formed by the fluctuations of the colored diquark field are coupled to the colorless photon field through the AL, MT, and DOS terms. This nontrivial complication due to the color degrees of freedom is absent in and contrasted with these terms for metallic superconductors.

6.3 Case of QCD-CP soft mode

Next, the photon self-energy modified by the soft modes of the QCD-CP and its calculation or approximation scheme are explained similarly to the previous subsection, which is based on Ref. [85]. In this section, the differences from the previous subsection will be mainly described and similar descriptions will be omitted.

6.3.1 Construction scheme

We construct $\tilde{\Pi}^{R\mu\nu}_S(\boldsymbol{k},\omega)$ that includes the QCD-CP soft modes as in Sec. 5.3.1. The starting point is also the one-loop diagram of the QCD-CP soft mode, which is the lowest-order contribution of the collective soft modes to the thermodynamic potential

$$\Omega_S = \int_p \ln[G_S\tilde{\Xi}^{-1}_S(p)],\tag{6.33}$$

which is diagrammatically shown in Fig. 6.4. Attaching electromagnetic vertices at two points of quark lines to Ω_S, we can obtain the ten types of diagrams in Fig. 6.5, which are corresponding

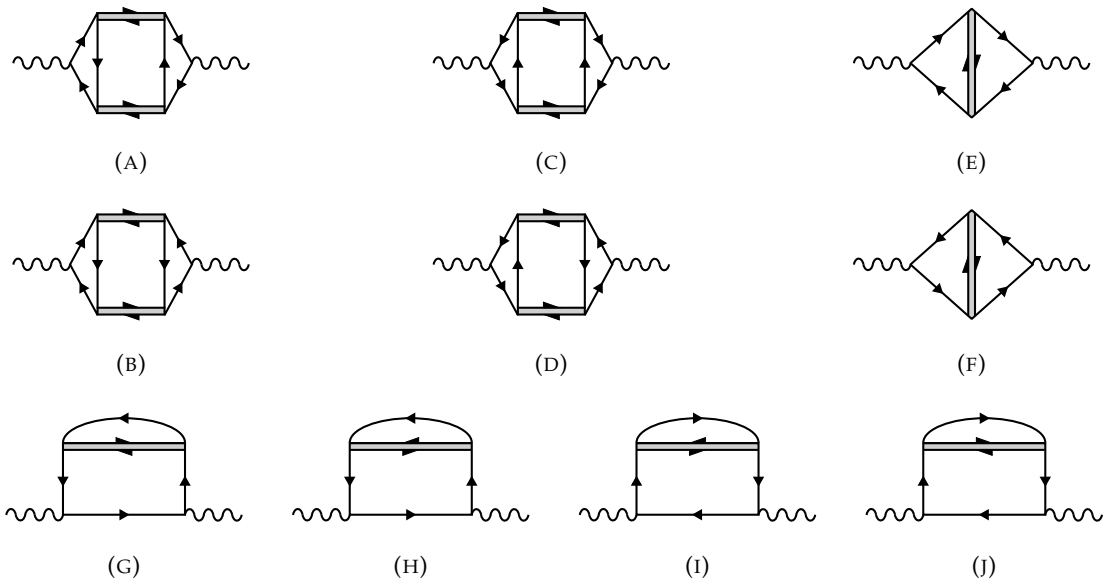

FIGURE 6.5: Diagrammatic representations of the Aslamazov-Larkin (a)–(d), Maki-Thompson (e, f) and density of states (g)–(j) terms with the QCD-CP soft modes.

to (a)-(d) Aslamazov-Larkin (AL), (e)-(f) Maki-Thompson (MT) and (g)-(j) density of states (DOS) terms, respectively. The respective contributions to the photon self-energy in the imaginary-time formalism are expressed, respectively, as

$$\tilde{\Pi}^{\mu\nu}_{\mathrm{AL},S}(k) = \sum_{f=u,d} \int_q \tilde{\Gamma}^{\mu}_f(q,q+k)\tilde{\Xi}_S(q+k)\tilde{\Gamma}^{\nu}_f(q+k,q)\tilde{\Xi}_S(q), \tag{6.34}$$

$$\tilde{\Pi}^{\mu\nu}_{\mathrm{MT},S}(k) = \sum_{f=u,d} \int_q \tilde{\Xi}_S(q)\ \mathcal{R}^{\mu\nu}_{\mathrm{MT},f}(q,k), \tag{6.35}$$

$$\tilde{\Pi}^{\mu\nu}_{\mathrm{DOS},S}(k) = \sum_{f=u,d} \int_q \tilde{\Xi}_S(q)\ \mathcal{R}^{\mu\nu}_{\mathrm{DOS},f}(q,k). \tag{6.36}$$

The vertex functions $\tilde{\Gamma}^{\mu}_f(q,k)$, $\mathcal{R}^{\mu\nu}_{\mathrm{MT},f}(q,k)$ and $\mathcal{R}^{\mu\nu}_{\mathrm{DOS},f}(q,k)$ in Eqs. (6.34)–(6.36) are given by

$$\tilde{\Gamma}^{\mu}_f(q,q+k) = 2N_c e_f \sum_{s=\pm} s \int_p \mathrm{Tr}_d[\mathcal{G}_0(p)\gamma^{\mu}\mathcal{G}_0(p+sk)\mathcal{G}_0(p-sq)], \tag{6.37}$$

$$\mathcal{R}^{\mu\nu}_{\mathrm{MT},f}(q,k) = 4N_c e_f^2 \sum_{s=\pm} \int_p \mathrm{Tr}_d[\mathcal{G}_0(p)\gamma^{\mu}\mathcal{G}_0(p+sk)\mathcal{G}_0(p+sk+sq)\gamma^{\nu}\mathcal{G}_0(p+sq)], \tag{6.38}$$

$$\mathcal{R}^{\mu\nu}_{\mathrm{DOS},f}(q,k) = 2N_c e_f^2 \sum_{s,t=\pm} \int_p \mathrm{Tr}_d[\mathcal{G}_0(p)\gamma^{\mu}\mathcal{G}_0(p+sk)\gamma^{\nu}\mathcal{G}_0(p)\mathcal{G}_0(p+tq)]. \tag{6.39}$$

From Eqs. (6.37)–(6.39), one can also easily show that these vertices satisfy the WT identities

$$k_\mu\tilde{\Gamma}^{\mu}_f(q,q+k) = e_f[\tilde{\Xi}_S^{-1}(q+k) - \tilde{\Xi}_S^{-1}(q)], \tag{6.40}$$

$$k_\mu\mathcal{R}^{\mu\nu}_{D,f}(q,k) = e_f[\tilde{\Gamma}^{\nu}_f(q-k,q) - \tilde{\Gamma}^{\nu}_f(q,q+k)], \tag{6.41}$$

with $\mathcal{R}^{\mu\nu}_{S,f}(q,k) = \mathcal{R}^{\mu\nu}_{\mathrm{MT},f}(q,k) + \mathcal{R}^{\mu\nu}_{\mathrm{DOS},f}(q,k)$.

We note that the number of diagrams is doubled compared with the case in Sec. 6.2.1, since the quark and anti-quark lines should be distinguished for the present case. Then, Eqs. (6.34)–(6.36)

gives the contribution of the QCD-CP soft modes to the photon self-energy in Eq. (6.1)

$$\tilde{\Pi}^{\mu\nu}_S(k) = \tilde{\Pi}^{\mu\nu}_{\mathrm{AL},S}(k) + \tilde{\Pi}^{\mu\nu}_{\mathrm{MT},S}(k) + \tilde{\Pi}^{\mu\nu}_{\mathrm{DOS},S}(k). \tag{6.42}$$

which satisfies the WT identity of the photon self-energy

$$k_\mu \tilde{\Pi}^{\mu\nu}_S(k) = 0, \tag{6.43}$$

Hence the total photon self-energy (6.1) satisfies the WT identity $k_\mu \tilde{\Pi}^{\mu\nu}(k) = 0$.

6.3.2 Approximation to vertices

We consider the approximation of $\tilde{\Gamma}^\mu_f(q, q+k)$ and $\mathcal{R}^{\mu\nu}_f(q,k) = \mathcal{R}^{\mu\nu}_{\mathrm{MT},f}(q,k) + \mathcal{R}^{\mu\nu}_{\mathrm{DOS},f}(q,k)$ as in the case of the 2SC. The WT identities for the vertices are

$$k_\mu \tilde{\Gamma}^\mu_f(q, q+k) = -e_f[\tilde{\Xi}^{-1}_S(q+k) - \tilde{\Xi}^{-1}_S(q)], \tag{6.44}$$

$$k_\mu \mathcal{R}^{\mu\nu}_f(q,k) = -e_f[\tilde{\Gamma}^\nu_f(q-k, q) - \tilde{\Gamma}^\nu_f(q, q+k)], \tag{6.45}$$

Using the analytic continuation of the LE approximation (5.45)

$$\tilde{\Xi}_S(q) = A_S(\boldsymbol{q}) + \mathcal{C}_S(q_0) \quad \text{with} \quad \mathcal{C}_S(\boldsymbol{q}, q_0) = \begin{cases} (C_S(\boldsymbol{q})q_0)^* & \mathrm{Im} q_0 > 0, \\ 0 & \mathrm{Im} q_0 = 0, \\ C_S(\boldsymbol{q})q_0 & \mathrm{Im} q_0 < 0, \end{cases} \tag{6.46}$$

The vertex of the AL term is approximated as

$$\tilde{\Gamma}^0_S(q, q+k) = -e_f[\mathcal{C}_S(\boldsymbol{q}+\boldsymbol{k}, q_0+k_0) - \mathcal{C}_S(\boldsymbol{q}, q_0)]/q_0, \tag{6.47}$$

$$\tilde{\Gamma}^i_S(q, q+k) = \Gamma^i_S(\boldsymbol{q}, \boldsymbol{q}+\boldsymbol{k}) = e_f A^{(1)}_S(\boldsymbol{q}+\boldsymbol{k}, \boldsymbol{q})(2q+k)^i, \tag{6.48}$$

with

$$A^{(1)}_S(\boldsymbol{q}_1, \boldsymbol{q}_2) = \frac{A_S(\boldsymbol{q}_1) - A_S(\boldsymbol{q}_2)}{|\boldsymbol{q}_1|^2 - |\boldsymbol{q}_2|^2}, \tag{6.49}$$

Since $C_S(\boldsymbol{q})$ and $A_S(\boldsymbol{q})$ are pure imaginary and real, $\tilde{\Gamma}^0_f(q, q+k)$ and $\tilde{\Gamma}^i_f(q, q+k)$ is also pure imaginary and real, respectively. Moreover, within the TDGL approximation (5.47), the spatial component is approximated as

$$\tilde{\Gamma}^i_f(q, q+k) = \Gamma^i_S(\boldsymbol{q}, \boldsymbol{q}+\boldsymbol{k}) = e_f b_S(2q+k)^i. \tag{6.50}$$

while the temporal one is obtained by replacing $C_S(\boldsymbol{q})$ to $c_S/|\boldsymbol{q}|$ in Eq. (6.47).

In Fig. 6.6, the momentum dependence of $\Gamma^i_{f=u}(\boldsymbol{q}, \boldsymbol{q}+\boldsymbol{k})$ at $\boldsymbol{k} = \boldsymbol{0}$ is compared, where $q^i = |\boldsymbol{q}|$. It is found that the TDGL approximation (6.50) can reproduce the LE approximation (6.48) in the small $\boldsymbol{q}$ region. Therefore, when the strength of the soft mode is concentrated on the origin of the ω'-$|\boldsymbol{q}|$ plane around the QCD-CP, both approximations give similar results. On the other hand, the behavior of the AL term calculated by both approximations becomes different as (T, μ) goes away from $(T_{\mathrm{CP}}, \mu_{\mathrm{CP}})$, since the strength of the soft mode is scattered and the contribution in the large $\boldsymbol{q}$ region is bigger owing to the difference of Eqs. (6.48) and (6.50).

As in Sec 6.2.2, let us show that the LE and TDGL approximations for the vertex are also adequate for the analysis of the AL term in the small k^μ region. Firstly, from Eq. (6.37), one can find

$$\tilde{\Gamma}^\mu_f(q, q+k)|_{k=0} = 2N_c e_f \sum_{s=\pm} \int_p \mathrm{Tr}_d[\mathcal{G}_0(p)\gamma^\mu \mathcal{G}_0(p)\mathcal{G}_0(p-sq)] = -e_f \frac{\partial \mathcal{Q}_S(q)}{\partial q_\mu}. \tag{6.51}$$

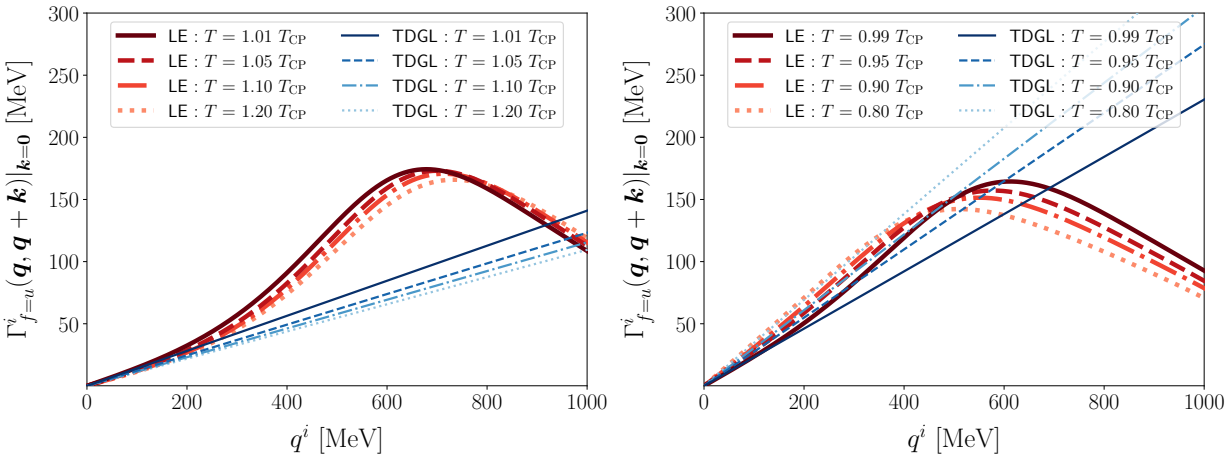

FIGURE 6.6: Momentum dependence of the vertex in the AL term approximated by the LE approximation (6.48) and TDGL approximation (6.50). at $\mu = \mu_{\rm CP}$ with $|\boldsymbol{k}| = 0$ for several temperatures. The solid (red) and dashed (blue) lines are corresponding to the results by the LE approximation and the TDGL approximation, respectively.

Through easy calculations, it is found that $\partial \mathcal{Q}_S(q)/\partial q_0$ has a factor $1/|\boldsymbol{q}|$, while $\partial \mathcal{Q}_S(q)/\partial q_i$ does not. Both approximations (6.47) and (6.50), are satisfied with these functional properties.

Additionally, let us examine the WT identity (6.44) at $\boldsymbol{k} = \boldsymbol{0}$,

$$k_0 \tilde{\Gamma}^0_f(q, q+k)|_{\boldsymbol{k}=\boldsymbol{0}} = -e_f[\tilde{\Xi}_S^{-1}(\boldsymbol{q}, q_0+k_0) - \tilde{\Xi}_S^{-1}(\boldsymbol{q}, q_0)]. \tag{6.52}$$

By substituting the LE approximation for the soft mode (5.45) into Eq. (6.52) and dividing both sides by k_0, we find Eq. (6.47). This means the LE approximation satisfies with the WT identity (6.52), which is also fulfilled in the TDGL approximation. Owing to these analyses, it is confirmed that our approximation method is validated in the small k^μ region.

Also, the vertices of the MT and DOS terms $\mathcal{R}^{\mu\nu}_f(q,k)$ can be approximated as

$$\mathcal{R}^{00}_f(q,k) = -e_f \frac{\tilde{\Gamma}^0_f(q, q+k) - \tilde{\Gamma}^0_f(q-k, q)}{k_0}, \tag{6.53}$$

$$\mathcal{R}^{ij}_f(q,k) = R^{ij}_f(\boldsymbol{q}, \boldsymbol{k}) = 4e_f \frac{\Gamma^i_f(\boldsymbol{q}, \boldsymbol{q}+\boldsymbol{k}) - \Gamma^i_f(\boldsymbol{q}-\boldsymbol{k}, \boldsymbol{q})}{(\boldsymbol{q}+\boldsymbol{k})^2 - (\boldsymbol{q}-\boldsymbol{k})^2} q^j, \tag{6.54}$$

where Eqs. (6.53) and (6.54) is pure imaginary and real, respectively. As in Eq. (6.30), the imaginary part of the spatial components cancel out since the spatial components of the vertices are real functions and independent of the energy as follows

$$\mathrm{Im}\Pi^{Rij}_{\mathrm{MT},S}(\boldsymbol{k}, \omega) + \mathrm{Im}\Pi^{Rij}_{\mathrm{DOS},S}(\boldsymbol{k}, \omega) = 0. \tag{6.55}$$

6.3.3 Explicit form of AL term

In the same manner as Eq. (6.32), using the LE approximation (5.45), (6.48) or the TDGL approximation (5.47), (6.50), the AL term is calculated as

$$\mathrm{Im}\Pi^{Rij}_{\mathrm{AL},S}(\boldsymbol{k}, \omega) = \sum_f \int \frac{d^3q}{(2\pi)^3} \Gamma^i_{S,f}(\boldsymbol{q}+\boldsymbol{k}, \boldsymbol{q}) \Gamma^j_{S,f}(\boldsymbol{q}+\boldsymbol{k}, \boldsymbol{q}) \int \frac{d\omega'}{2\pi} \coth\frac{\omega'}{2T}$$
$$\times \mathrm{Im}\Xi^R_S(\boldsymbol{q}+\boldsymbol{k}, \omega')\{\mathrm{Im}\Xi^R_S(\boldsymbol{q}, \omega'+\omega) - \mathrm{Im}\Xi^R_S(\boldsymbol{q}, \omega'-\omega)\}, \tag{6.56}$$

whose integration range is also determined by the limitations of $\mathrm{Im}Q^R_S$ within $\mathrm{Im}\Xi^R_S$ as in Eq. (6.32).

Let us mention the limitation of the formulation for the QCD-PT case. In this case, we focus on the effect of the QCD-CP mode that lives in the space-like region and neglect the effect of the sigma mode in the time-like region. This approximation can be justified as long as the DPR in the low energy/momentum region and associated transport coefficients near the QCD-CP is considered since the mass of the sigma mode is larger than $2M \simeq 370$ MeV. However, the effect of this mode will be important when the DPR above $2M$ is considered.

Finally, we note that the above construction of $\tilde{\Pi}^{\mu\nu}_{\gamma}(k)$ corresponds to the linear approximation of the soft modes in the sense that the interaction between the soft modes is neglected. This feature comes from the fact that Eqs. (6.8) and (6.33) is composed only of a one-loop diagram of $\tilde{\Xi}_{\gamma}(q)$. The linear approximation would be eventually violated as T approaches T_c and the amplitude of the diquark fluctuations grows. Our analysis in the following thus is not applicable to such a temperature range, where the growth of critical fluctuations is governed by the critical exponents determined by the dynamical universality class [101]. However, it is known that the formalism similar to ours developed for metallic superconductivity [45] well describes the precursory phenomena in electric conductivity in metals for a wide range of T. It thus is expected that our analysis in the following would also be capable of describing quantitative behaviors of the transport coefficients in a certain range of T. To extend our formalism to the vicinity of Tc, one may start from the thermodynamic potential with multiple loops of $\tilde{\Xi}_{\gamma}(q)$ [99]. The properties of the soft mode will also be modified there, which will be amended via the self-consistent treatment. Another issue in our formalism is that the thermodynamics is determined in the MFA, where Eqs. (6.8) and (6.33) is not included. While this treatment would be justified when the system is away from the critical point and effects of the soft modes are suppressed [45], in the vicinity of Tc the thermodynamic potential should include the effects of fluctuations so as to make the formalism self-consistent. In the present study, however, we neglect these effects to investigate the magnitude of fluctuations qualitatively in a simple formalism.

Chapter 7

Transport coefficients

In this chapter, we investigate the effect of the soft modes on the transport coefficients, electric conductivity σ and associated relaxation time τ_σ, through the analysis of the photon self-energy that has been constructed in Chap. 6. This study is based on Ref. [83].

To start the analysis of the transport coefficients, we define the spectral density at zero momentum using the retarded function of the photon self-energy (6.1) by the manner described in Sec. 1.3.3:

$$\rho(\omega) = g_{\mu\nu}\mathrm{Im}\Pi^{R\mu\nu}(\mathbf{0},\omega) = -\sum_{i=1,2,3}\mathrm{Im}\Pi^{Rii}(\mathbf{0},\omega). \tag{7.1}$$

Since the Ward identity for the photon self-energy (6.3) is satisfied, the coefficients σ and τ_σ can be read using Eq. (7.2) as follows

$$\sigma = \frac{1}{3}\frac{\partial\rho(\omega)}{\partial\omega}\bigg|_{\omega=0}, \quad \tau_\sigma = \sqrt{-\frac{1}{3!}\frac{\partial^3\rho(\omega)}{\partial^3\omega}\bigg|_{\omega=0} \Big/ \frac{\partial\rho(\omega)}{\partial\omega}\bigg|_{\omega=0}}. \tag{7.2}$$

Eq. (6.1) consists of the three contributions, and then the spectral density (7.1) is decomposed as

$$\rho(\omega) = \rho_{\mathrm{free}}(\omega) + \rho_D(\omega) + \rho_S(\omega) \tag{7.3}$$

with

$$\rho_{\mathrm{free}}(\omega) = -\sum_i \mathrm{Im}\Pi^{Rii}_{\mathrm{free}}(\mathbf{0},\omega), \tag{7.4}$$

$$\rho_\gamma(\omega) = -\sum_i \mathrm{Im}\Pi^{Rii}_\gamma(\mathbf{0},\omega) \quad \text{for} \quad \gamma = D, S. \tag{7.5}$$

In our formalism, the photon self-energy with the soft modes consists of the AL, MT, and DOS terms. Of these terms, however, the spatial components of the MT and DOS terms cancel as in Eqs. (6.29) and (6.55). Thereby, the contributions of the soft modes $\rho_\gamma(\omega)$ is given by only the AL term, and then $\partial^n\rho_\gamma(\omega)/\partial^n\omega|_{\omega=0}$ for $n = 1, 3$ are calculated with Eqs. (6.32) and (6.56) as follows

- the LE approximation

$$\frac{\partial^n\rho_D(\omega)}{\partial^n\omega}\bigg|_{\omega=0} = 2\bar{N}_\gamma\int\frac{d^3q}{(2\pi)^3}\left(\frac{\partial A_\gamma(\boldsymbol{q})}{\partial|\boldsymbol{q}|}\right)^2\int d\omega'\coth\frac{\omega'}{2T} \times \mathrm{Im}\Xi^R_\gamma(\boldsymbol{q},\omega')\frac{\partial^n}{\partial^n\omega'}\mathrm{Im}\Xi^R_\gamma(\boldsymbol{q},\omega'), \tag{7.6}$$

- the TDGL approximation

$$\frac{\partial^n\rho_D(\omega)}{\partial^n\omega}\bigg|_{\omega=0} = 2\bar{N}_\gamma\int\frac{d^3q}{(2\pi)^3}\left(2b_\gamma\boldsymbol{q}\right)^2\int d\omega'\coth\frac{\omega'}{2T} \times \mathrm{Im}\Xi^R_\gamma(\boldsymbol{q},\omega')\frac{\partial^n}{\partial^n\omega'}\mathrm{Im}\Xi^R_\gamma(\boldsymbol{q},\omega'). \tag{7.7}$$

To obtain Eq. (7.6), $A_\gamma^{(1)}(\boldsymbol{q}+\boldsymbol{k},\boldsymbol{q})|_{k=0} = \partial A_\gamma/\partial|\boldsymbol{q}|$ has been used, where $A_\gamma^{(1)}(\boldsymbol{q}_1,\boldsymbol{q}_2)$ has been defined by Eqs. (6.20) and (6.49) for $\gamma = D$ and S, respectively. Also, the overall coefficient N_γ is

$$\bar{N}_D = 3e_\Delta^2, \quad \bar{N}_S = e_u^2 + e_d^2. \tag{7.8}$$

The integrand of $\partial^n\rho_\gamma(\omega)/\partial^n\omega|_{\omega=0}$ for $n = 1,3$ becomes divergent at $(\boldsymbol{q},\omega') = (\boldsymbol{0},0)$ as the system approaches the critical points, which is due to the property of the soft modes that have been described in Chap. 5. Then, this leads to the divergence of σ and τ_σ at the 2SC-PT and QCD-CP. Therefore, near the 2SC-PT, the contribution from $\rho_D(\omega)$ is dominates over the one from $\rho_S(\omega)$ and the behavior of σ and τ_σ is described only by $\rho_D(\omega)$, and vice versa. In this thesis, we calculate the transport coefficients from $\rho_D(\omega)$ and $\rho_S(\omega)$ separately near the 2SC-PT and QCD-CP, respectively,

On the other hand, $\rho_{\rm free}(\omega)$ does not contribute to σ and τ_σ since $\rho_{\rm free}(\omega) = 0$ for $|\omega| < 2M$ and M is finite. From Eq. (6.6), its density is given by

$$\rho_{\rm free}(\omega) = \frac{N_c(e_u^2+e_d^2)}{4\pi}(\omega^2+2M^2)\sqrt{\frac{\omega^2-4M^2}{\omega^2}}\sum_{s=\pm}\tanh\frac{\omega-2s\mu}{4T}\,\theta(|\omega|-2M), \tag{7.9}$$

and then all its ω derivatives vanish at $\omega = 0$. Even in the massless case, $\rho_{\rm free}(\omega)$ cannot give a finite contribution to σ. Taking the limit $\omega \to 0$ at $M = 0$, Eq. (7.9) becomes

$$\rho_{\rm free}(\omega)|_{M=0} = \frac{N_c(e_u^2+e_d^2)}{8\pi}\cosh^{-2}\frac{\mu}{2T}\,\frac{\omega^3}{T} + \mathcal{O}(\omega^5). \tag{7.10}$$

From this, $\partial\rho_{\rm free}(\omega)/\partial\omega|_{\omega=0} = 0$ can be checked. Also, the contribution of $\rho_{\rm free}(\omega)$ to τ_σ is neglected since$\partial^3\rho_\gamma(\omega)/\partial^3\omega \gg \partial^3\rho_{\rm free}(\omega)/\partial^3\omega$ around the 2SC-PT and QCD-CP

7.1 Analytical results

Let us investigate the limiting behaviors of the transport coefficients σ and τ_σ as the system approaches the 2SC-PT or QCD-CP with the TDGL approximation (7.7) that allows us to calculate the critical exponents of those coefficients analytically.

Firstly, we consider the case of 2SC-PT. Since the strength from the soft modes is concentrated around the origin of energy/momentum plane near the 2SC-PT, the dominant contribution to σ and τ_σ from the soft modes exists there. Then, in Eq. (7.7), one can carry out the following replacement

$$\coth\frac{\omega'}{2T} \;\to\; \frac{2T}{\omega'}. \tag{7.11}$$

Also, since the integrand of $\partial^n\rho_D(\omega)/\partial^n\omega|_{\omega=0}$ converges in the $|\omega'| \to \infty$ and $|\boldsymbol{q}| \to \infty$ limit, the integration range can be deformed as

$$\int\frac{d^3q}{(2\pi)^3}\int d\omega' = \int_0^{2\sqrt{\mu^2-M^2}} q^4dq\int_{\lambda(q,0)-2\mu}^{\bar{\Lambda}} d\omega' \;\to\; \int_0^\infty q^4dq\int_{-\infty}^{+\infty}d\omega'. \tag{7.12}$$

Here, the first equality is due to the limitation of approximation for $\mathrm{Im}\Xi_D^R(\boldsymbol{q},\omega')$ as described in Sec. 5.3.1. By these simplifications we can calculate Eq. (7.7) for $\gamma = D$ analytically as follows

$$\left.\frac{\partial\rho_D(\omega)}{\partial\omega}\right|_{\omega=0} = -\frac{9e_\Delta^2T}{16\pi}\frac{|c_D|^2}{\mathrm{Im}c_D}\frac{1}{a_D^{1/2}b_D^{1/2}}, \tag{7.13}$$

$$\left.\frac{\partial^3\rho_D(\omega)}{\partial^3\omega}\right|_{\omega=0} = \frac{27e_\Delta^2T}{512\pi}\frac{|c_D|^6}{(\mathrm{Im}c_D)^3}\frac{1}{a_D^{5/2}b_D^{1/2}}, \tag{7.14}$$

where $\partial\rho_D(\omega)/\partial\omega|_{\omega=0}$ and $\partial^3\rho_D(\omega)/\partial^3\omega|_{\omega=0}$ are positive and negative numbers, respectively, because of $\mathrm{Im}c_D < 0$. These detailed calculations are in Appendix C.

Inserting Eqs. (7.13) and (7.14) into Eq. (7.2) and using Eq. (5.38), we obtain

$$\sigma \sim T\frac{|c_D|}{a_D^{1/2}b_D^{1/2}} \sim \frac{T}{\epsilon^{1/2}}, \qquad \tau_\sigma \sim \sqrt{\frac{|c_D|^2}{a_D^2}} \sim \frac{1}{T\epsilon}. \tag{7.15}$$

This result shows that both coefficients diverge at $T = T_c$ and the critical exponents of σ and τ_σ are $-1/2$ and -1, respectively. Regarding conductivity, the exponent is the same as the one in the case of the ultra-clean case of the three-dimensional metal [45], where only the AL term can give a critical contribution owing to the cancellation of the MT and DOS terms as well.

Equation (7.15) also tells us that the magnitude of σ and τ_σ does not depend on either μ or G_D explicitly within the approximation (5.43). This suggests that σ and τ_σ are insensitive to μ around the 2SC-PT. These analytic results will be checked numerically in Sec. 7.2 with the LE approximation. Using ξ_D and τ_D that are introduced in Eq. (5.44), Eq. (7.15) is rewritten as

$$\sigma \sim T\frac{\tau_\mathrm{D}}{\xi_D}, \qquad \tau_\sigma \sim \tau_\mathrm{D}. \tag{7.16}$$

From this, it is found that the typical time scale of the relaxation to the Ohm's law is given by the one of the damping of the soft modes.

Next, we consider the case of the QCD-CP. In the same manner as the case of the 2SC-PT, the replacement of Eq. (7.11) in the TDGL approximation (7.7) can be applied for the case of $\gamma = S$. In this case, since the soft mode is restricted to the space-like region ($|\omega + 2\mu| < \bar{k}(|\boldsymbol{k}|, \bar{\Lambda})$) as described in Sec. 5.3.2, we deform the integration region of $\partial^n\rho_D(\omega)/\partial^n\omega|_{\omega=0}$ as

$$\int \frac{d^3q}{(2\pi)^3}\int d\omega' = \int_0^{\bar{\Lambda}} q^4 dq \int_{-\bar{k}(|\boldsymbol{k}|,\bar{\Lambda}))}^{+\bar{k}(|\boldsymbol{k}|,\bar{\Lambda}))} d\omega' \;\rightarrow\; \int_0^{\infty} q^4 dq \int_{-q}^{+q} d\omega'. \tag{7.17}$$

Finally, we then obtain

$$\left.\frac{\partial\rho_S(\omega)}{\partial\omega}\right|_{\omega=0} = \frac{(e_u^2+e_d^2)T}{2\pi^3}\frac{\mathrm{Im}c_S}{a_S}\tan^{-1}\frac{\mathrm{Im}c_S}{a_S}, \tag{7.18}$$

$$\left.\frac{\partial^3\rho_S(\omega)}{\partial^3\omega}\right|_{\omega=0} = \frac{(e_u^2+e_d^2)T}{2\pi^3}\frac{3b_S(\mathrm{Im}c_S)^3}{4a_S^4}\tan^{-1}\frac{\mathrm{Im}c_S}{a_S}. \tag{7.19}$$

These detailed calculations are also given in Chap. C. As seen in Eq. (5.50), the exponent of a_S with respect to ϵ_CP depends on the direction to approach the CP, while b_S and c_S are insensitive to ϵ_CP. Inserting Eqs. (7.18) and (7.19) into Eq. (7.2) and using Eq. (5.50), one thus can find the exponents of the divergences as follows

$$\sigma \sim \frac{1}{a_S} \sim \begin{cases} \epsilon_\mathrm{CP}^{-1} & \text{parallel to the first-order line,} \\ \epsilon_\mathrm{CP}^{-2/3} & \text{otherwise,} \end{cases} \tag{7.20}$$

$$\tau_\sigma \sim \frac{1}{a_S^{3/2}} \sim \begin{cases} \epsilon_\mathrm{CP}^{-3/2} & \text{parallel to the first-order line,} \\ \epsilon_\mathrm{CP}^{-1} & \text{otherwise.} \end{cases} \tag{7.21}$$

Unlike in the case of the 2SC-PT, the critical exponents due to the QCD-CP soft modes depend on the way to approach the critical point.

Before closing this subsection, several remarks are in order. First, as mentioned in Sec. 6.2, the above results are obtained in the linear approximation for the soft modes. The critical exponent thus corresponds to the mean-field ones. The non-linear effects will be negligible near the 2SC-PT and QCD-CP, which will alter the critical exponents to the values determined by the universality

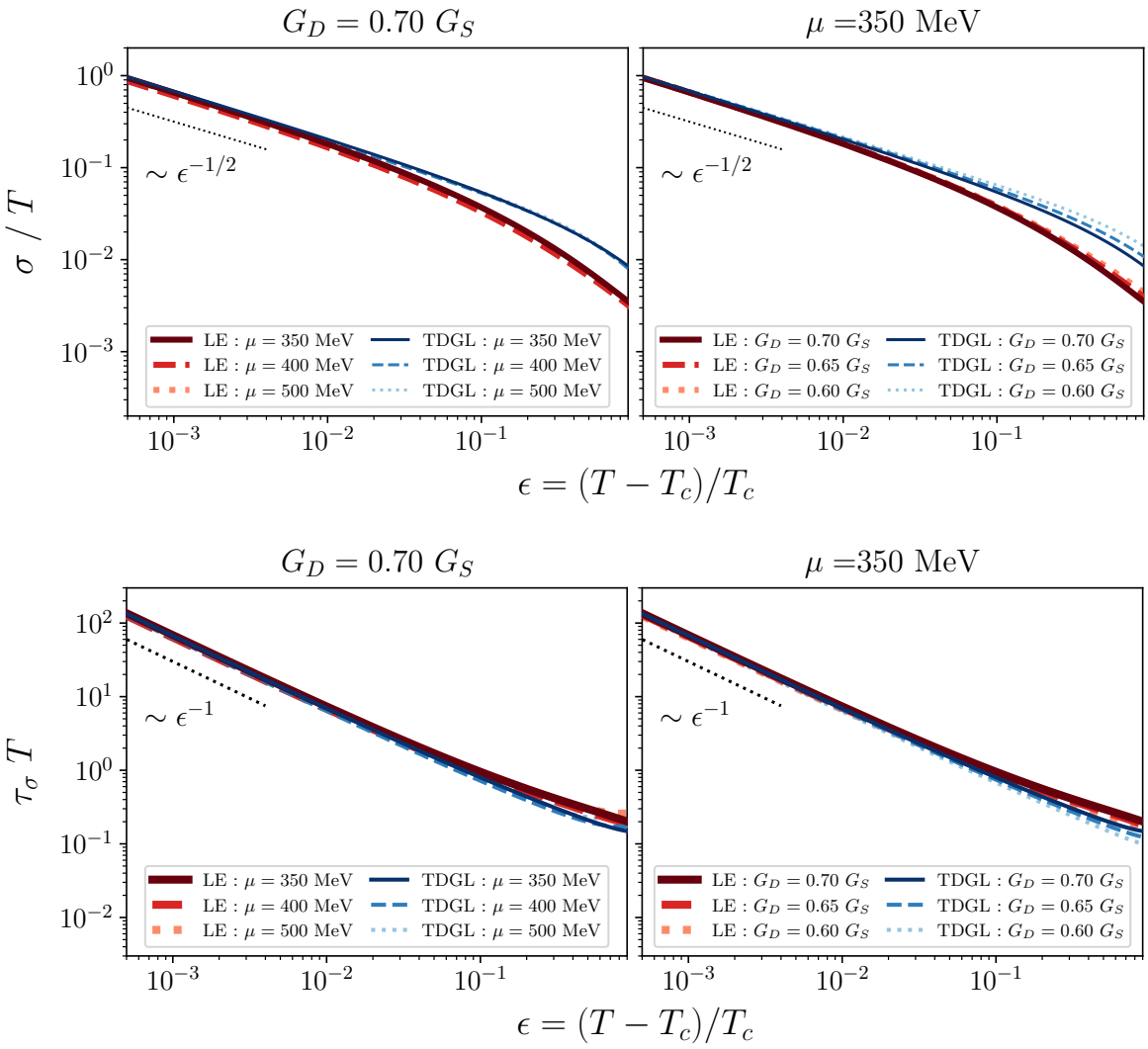

FIGURE 7.1: Electric conductivity and associated relaxation time due to the soft modes of the 2SC-PT at several values of μ and G_D. The thick red and thin blue lines are calculated by the LE and the TDGL approximation, respectively. The dotted line in each panel represents the critical exponent given in Eq. (7.15). In the left panels, the lines are plotted at $\mu = 350$, 400, 500 MeV with $G_D = 0.7G_S$, while the right panels, the lines are plotted with $G_D = 0.70$, 0.65, and $0.60G_S$ at $\mu = 350$MeV.

class. We, however, emphasize that our analysis gives the values of σ and τ_σ up to the absolute value, while the universal argument is not capable of constraining them. Second, let us discuss the origin of the different critical exponents. The dependencies of σ and τ_σ on the TDGL coefficient a_γ are different from each other, which is caused by the differences in the momentum dependence of the soft mode propagators $\Xi^R_\gamma(\boldsymbol{k}, \omega)$. Additionally, the exponents of a_D and a_S differ as shown in Eqs. (5.38) and (5.50). These two differences in the properties of the soft modes cause the various exponents of the transport coefficients. It is fascinating that the different exponents can be obtained even though the effects of soft modes are taken into account at the RPA level.

7.2 Numerical results

In this section, we study the behavior of σ and τ_σ numerically with the LE approximation (7.6) and TDGL approximations (7.7).

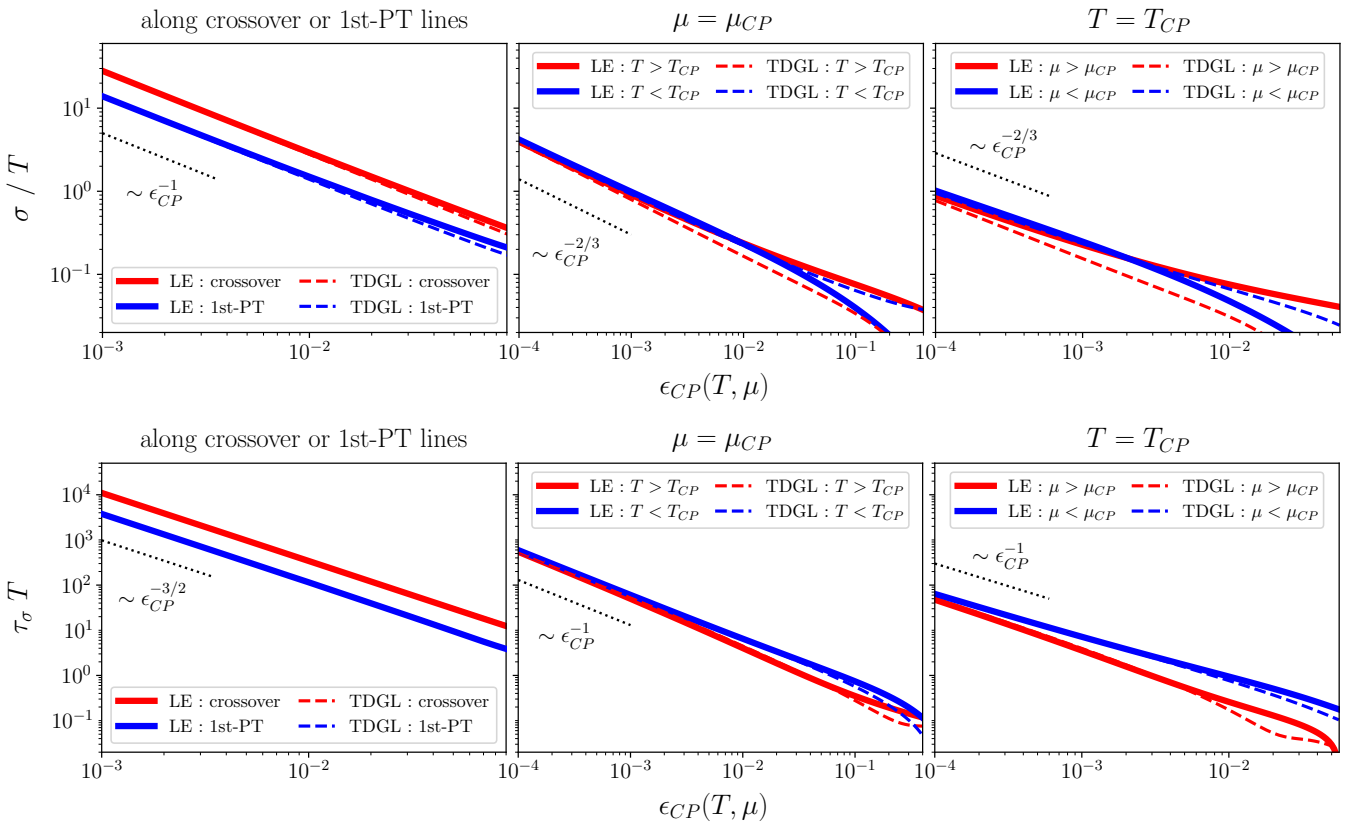

FIGURE 7.2: Electric conductivity and associated relaxation time due to the soft modes of the QCD-PT. The red thick and blue thin lines are calculated by the LE and the TDGL approximation, respectively. The upper and lower panels are the results of σ/T and $\tau_\sigma T$, respectively. The left panels are plotted along the crossover transition lines or first-order PT. The middle and right panels are plotted along the T-direction at $\mu = \mu_{\rm CP}$ and along the μ-direction at $T = T_{\rm CP}$, respectively. The thin dotted line in each panel represents the exponents of divergence as in Eqs. (7.20) and (7.21).

First, let us see the behavior of σ and τ_σ near the 2SC-PT. Figure 7.1 shows σ/T (upper panels) and $\tau_\sigma T$ (lower panels) that are obtained from $\rho_D(\omega)$. These are plotted as functions of $\epsilon = (T - T_c)/T_c$. The left panels show the results for $\mu = 350, 400, 500$ MeV with fixed $G_D = 0.7G_S$, while the results on the right panels are plotted with several values of G_D at fixed $\mu = 350$ MeV. The thick-red (thin-blue) lines represent the results obtained with the LE (TDGL) approximation. It is found that σ/T and $\tau_\sigma T$ grows as $\epsilon \to 0$. One also sees that the LE and TDGL results converge to the same behavior in this limit, while their difference grows as ϵ becomes larger. As explained in Sec. 6.2.2, this is a reasonable result because the TDGL approximation is well justified only in the vicinity of T_c where the strength of the soft modes is concentrated at the small energy-momentum region. For large ϵ, the TDGL result tends to underestimate the LE one. This result is mainly attributed to the behavior of the vertex function as discussed in Sec. 6.2.2. To check the critical exponents of σ and τ_σ, in Fig. 7.1 we show the slope of exponent in Eq. (7.15) by the thin dotted lines. One sees that the numerical results are in good agreement with these analytic results. Another interesting feature found in the figure is that the numerical results on σ/T and $\tau_\sigma T$ are insensitive to μ and G_D. This result is expected from Eq. (7.15).

Next, we show the numerical results for the QCD-CP in Fig. 7.2. The upper and lower panels are the results of σ/T and $\tau_\sigma T$ calculated from $\rho_S(\omega)$. These are plotted with respect to $\epsilon_{\rm CP}$. In the left panels, T and μ are varied along the line parallel to the first-order transition line passing through the CP, where the results for $T < T_{\rm CP}$ are plotted for two coexisting phases on the first-order phase transition, while the ones for $T > T_{\rm CP}$ is plotted along the crossover transition line. In the middle

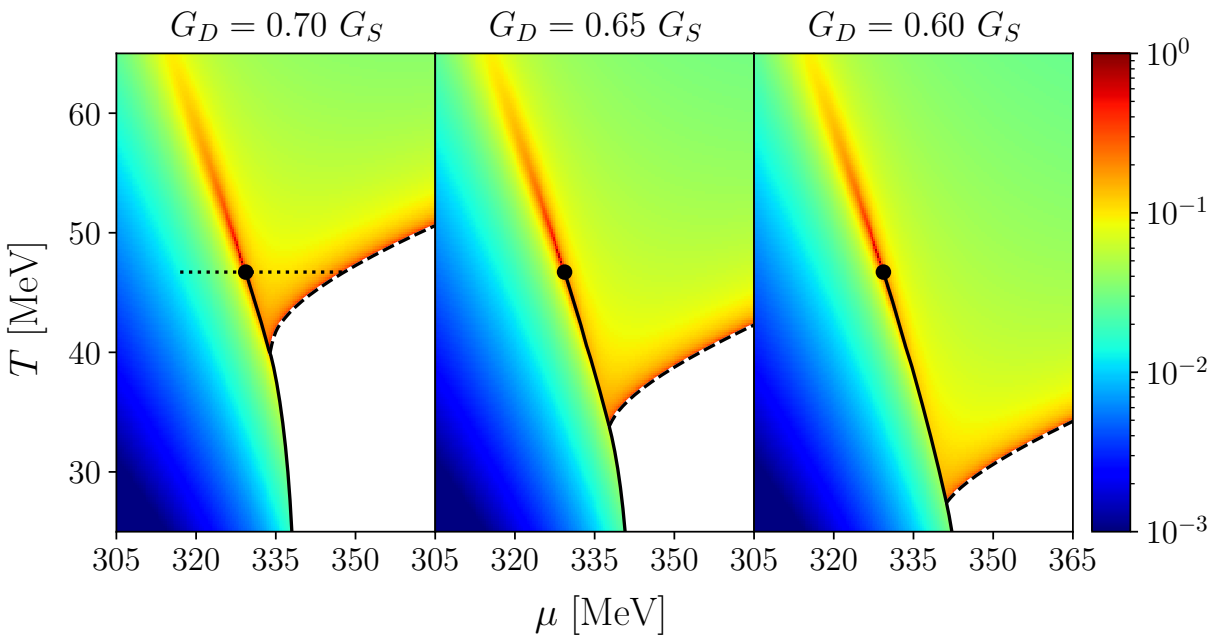

FIGURE 7.3: Contour maps of σ/T in the T-μ plane around the CP with $G_D/G_S = 0.70$, 0.65 and 0.60. The solid and dashed lines are the first-order and second-order phase transitions, respectively.

panels, we set $\mu = \mu_{\rm CP}$, while, in the right panels, T is fixed at $T_{\rm CP}$. In these panels, the thick-red and thin-blue lines are the results obtained by the LE and TDGL approximations, respectively, while the thin-dotted black lines represent the exponents given in Eqs. (7.20) and (7.21).

The above figures show that the numerical results reproduce these critical behaviors near the QCD-CP. In particular, near the critical point, the coefficients behave as in the exponents expected in the previous section in all panels. In the left panels, one finds that the magnitude of the results are different when T and μ approach the critical point along the first-order phase transition and crossover transition lines. This difference is explained as follows. The thermodynamic potential (4.31) are expanded with respect to the chiral condensate as in the Landau free energy (2.1) near the QCD-CP. In this case, the coefficient a_S behaves as in Eq. (2.5) along the first-order phase transition and crossover transition. The difference of the magnitude reflects the behavior of a_S. Also, the results from the LE and TDGL approximations are consistent with each other around the critical point. However, as T and/or μ go away from the CP, they become to deviate. This is because the vertex function of the TDGL approximation disagrees with the one of the LE approximation as shown in Fig. 6.6.

Here, we see the behavior of σ/T including the effects of both 2SC-PT and QCD-CP soft modes on the phase diagram. In Fig. 7.3, we show the contour maps of σ/T on the T–μ plane around the first-order transition line for three values of the diquark couplings at $G_D = 0.70G_S$, $0.65G_S$, and $0.60G_S$. This figure is obtained by the LE approximations. The solid and dashed lines show the first-order phase transition and the second-order phase transition of the 2SC, respectively. Since our formalism is not applicable to the 2SC phase where the diquark condensate has a nonzero expectation value $\Delta \neq 0$, this phase is left blank in the figure. One finds that σ/T is enhanced around the 2SC-PT and QCD-CP. A significant enhancement due to the QCD-CP soft mode occurs along the critical line parallel to the first-order transition line. For $G_D = 0.7G_S$, this enhancement is almost connected to the one due to the 2SC-PT soft modes. However, these two enhancements move away from each other since T_c of the 2SC-PT is lowered as the value of G_D decreases. Since the electric conductivity is related to the low energy-momentum behavior of the dilepton production rate in the HIC, from Fig. 7.3 it is expected that the dilepton yield is enhanced when the medium created by the HIC goes through the red color region.

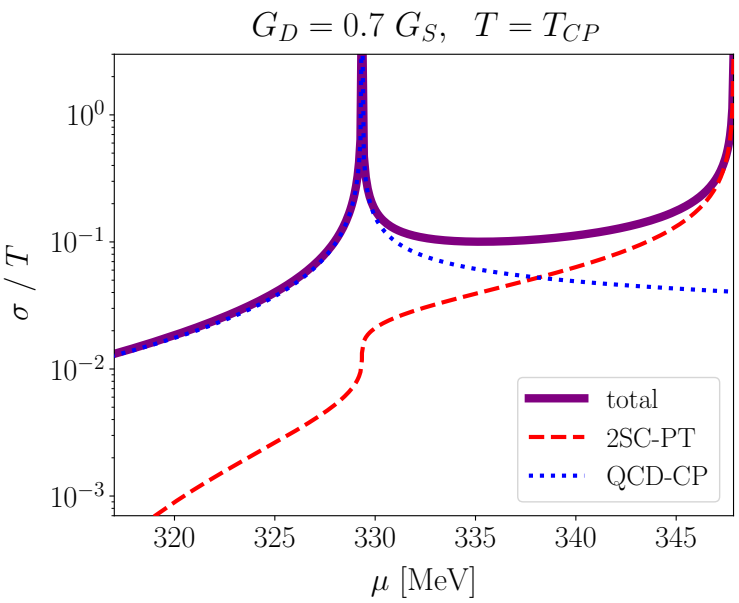

FIGURE 7.4: Comparison of the contributions of σ/T from the 2SC-PT and the QCD-CP soft modes at $T = T_{\rm CP}$. The solid line represents the total contribution of σ/T, and the dashed, and dotted lines are the ones from the soft modes of the 2SC and the QCD-CP, respectively.

In Fig. 7.4, we finally show the behavior of σ/T as a function of μ at $T = T_{\rm CP}$, i.e. along the dotted line in the left panel of Fig. 7.3 at $G_D = 0.7G_S$. In the figure, the solid line represents the total contribution of σ, and the dashed (dotted) line is the contribution from the soft modes of the 2SC-PT (QCD-CP). Since the QCD-CP is at $\mu_{\rm CP} \simeq 329$ MeV, the contribution of the QCD-CP is divergent there. On the other hand, the contribution of the 2SC-PT is divergent at $\mu \simeq 347$ MeV because the transition point of the 2SC-PT at $T = T_{\rm CP}$ exists there. Moreover, one can see that the contribution of the 2SC-PT is drastically decreasing around $\mu = \mu_{\rm CP}$. This is explained as follows. In our approximations, the denominators of the soft mode propagators are expanded in the direction of the energy at the origin of the energy/momentum plane of the soft mode. The 2SC-PT soft mode exists in the region $|\omega + 2\mu| > \lambda(\boldsymbol{k}, 0)$ as shown in Eq. (5.19), and then, the approximations are available only when when $M < \mu$. Additionally, at $M = \mu$, $\partial {\rm Im} Q^R(\boldsymbol{0}, \omega)/\partial\omega|_{\omega=0} = 0$. From these facts, the drastic decrease of σ due to the 2SC soft modes can be understood.

Let us give the brief summary for the analysis of the transport coefficients. In this chapter, the effects of the 2SC-PT and QCD-CP soft modes on the electric conductivity σ and the associated relaxation time τ_σ have been investigated through the analysis of the photon self-energy including these modes in the two-flavor NJL model. We considered the low energy/momentum limit of the AL, MT, and DOS terms for the photon self-energy. These terms constitute the self-energy in a gauge-invariant manner including the effects of the soft modes at the mean-field level. Through the analytic and numerical calculations, we have shown that the transport coefficients are enhanced near the 2SC-PT and QCD-CP with the power-like behavior owing to the existence of the soft modes near the respective phase transitions. Through the analytical analysis of the critical exponents of the transport coefficients, it has been shown that the origin of divergences is due to the soft modes and the difference in exponents comes from the different properties of the soft modes. As described in Sec. 1.3.3, the electric conductivity is related to the low energy and momentum behavior of the dilepton production rate (DPR) through the photon self-energy or electric current-current correlator. In the next Chapter, we will show the enhancement of the DPR due to the soft modes.

Chapter 8

Dilepton production rate (DPR)

In this chapter, we calculate the DPR using the photon self-energy constructed in Chap. (6). The DPR is calculated by using Eq. (1.10) together with Eq. (6.1)

$$\frac{d^4\Gamma}{d^4k}(\boldsymbol{k},\omega) = -\frac{\alpha}{12\pi^4}\frac{1}{k^2}\frac{1}{e^{\omega/T}-1}g_{\mu\nu}\mathrm{Im}\Pi^{R\mu\nu}(\boldsymbol{k},\omega). \tag{8.1}$$

Firstly, we give the explicit forms of $g_{\mu\nu}\mathrm{Im}\Pi^{R\mu\nu}_{\gamma}(k)$ for $\gamma = D, S$ and $g_{\mu\nu}\mathrm{Im}\Pi^{R\mu\nu}_{\mathrm{free}}(k)$ in Sec. 8.1. The numerical results of the energy and invariant-mass spectra are shown in Sec. 8.2 and 8.3, respectively, whose studies are based on Refs. [84, 85].

8.1 Explicit form of $g_{\mu\nu}\Pi^{R\mu\nu}(k)$

8.1.1 Contribution from the soft modes

We start from the WT identity for the photon self-energy $k_\mu\tilde{\Pi}^{\mu\nu}(k) = 0$. When the self-energy satisfies the Ward identity, $\tilde{\Pi}^{\mu\nu}(k)$ can be decomposed as follows

$$\tilde{\Pi}^{\mu\nu}(k) = P_T^{\mu\nu}\tilde{\Pi}_T(k) + P_L^{\mu\nu}\tilde{\Pi}_L(k), \tag{8.2}$$

where $P_T^{\mu\nu}$ and $P_L^{\mu\nu}$ are projection operators to transverse and longitudinal directions, respectively, and $\tilde{\Pi}_T(k)$ and $\tilde{\Pi}_L(k)$ are scalar functions of $|\boldsymbol{k}|$ and k^0. Each component of $P_T^{\mu\nu}$ and $P_L^{\mu\nu}$ is

$$P_T^{00} = P_T^{0i} = P_T^{i0} = 0, \quad P_T^{ij} = \delta^{ij} - k^i k^j/\boldsymbol{k}^2, \quad P_L^{\mu\nu} = k^\mu k^\nu/k^2 - g^{\mu\nu} - P_T^{\mu\nu}. \tag{8.3}$$

Let us give a useful formula for $\tilde{\Pi}^{00}(k)$ using the knowledge of the Ward identity. Considering $k_\mu k_\nu\tilde{\Pi}^{\mu\nu}(k) = 0$, we obtain the following relation

$$\tilde{\Pi}^{00}(k) = \frac{\boldsymbol{k}^2}{k^2}\tilde{\Pi}_L(k). \tag{8.4}$$

Here, we set $k = (k_1, k_2, k_3, k_0) = (|\boldsymbol{k}|, 0, 0, k_0)$, whose choice does not result in a loss of generality since $\tilde{\Pi}_T(k)$ and $\tilde{\Pi}_L(k)$ depend only on k^0 and $|\boldsymbol{k}|$ as described already. In this case, we find that the temporal component of the photon self-energy is

$$\tilde{\Pi}^{00}(k) = \frac{\boldsymbol{k}^2}{k_0^2}\tilde{\Pi}^{11}(k). \tag{8.5}$$

Then, we can express $g_{\mu\nu}\tilde{\Pi}^{\mu\nu}(k)$ with only the spacial components at $k = (|\boldsymbol{k}|, 0, 0, k_0)$ as

$$g_{\mu\nu}\tilde{\Pi}^{\mu\nu}(k) = \frac{\boldsymbol{k}^2}{k_0^2}\tilde{\Pi}^{11}(k) - g_{ij}\tilde{\Pi}^{ij}(k). \tag{8.6}$$

Next, we consider the contribution of the soft modes $g_{\mu\nu}\tilde{\Pi}^{\mu\nu}_{\gamma}(k)$ for $\gamma = D$ and S. As described in Secs. 6.2.2 and 6.3.2, the imaginary parts of spacial components in the MT and DOS terms cancel:

$$\mathrm{Im}\Pi^{Rij}_{\mathrm{MT},\gamma}(\boldsymbol{k},\omega) + \mathrm{Im}\Pi^{Rij}_{\mathrm{DOS},\gamma}(\boldsymbol{k},\omega) = 0.$$

Using this fact and Eq. (8.6), $g_{\mu\nu}\mathrm{Im}\Pi^{R\mu\nu}_{\gamma}(\boldsymbol{k},\omega)$ with $k = (|\boldsymbol{k}|,0,0,\omega)$ is given by only the spacial components of the retarded function of the AL term

$$g_{\mu\nu}\mathrm{Im}\Pi^{R\mu\nu}_{\gamma}(\boldsymbol{k},\omega) = \frac{\boldsymbol{k}^2}{\omega^2}\mathrm{Im}\Pi^{R11}_{\mathrm{AL},\gamma}(\boldsymbol{k},\omega) - \sum_{i=1,2,3}\mathrm{Im}\Pi^{Rii}_{\mathrm{AL},\gamma}(\boldsymbol{k},\omega). \tag{8.7}$$

The explicit forms of $\mathrm{Im}\Pi^{Rij}_{D}(\boldsymbol{k},\omega)$ and $\mathrm{Im}\Pi^{Rij}_{S}(\boldsymbol{k},\omega)$ are given by Eqs. (6.32) and (6.56), and then $g_{\mu\nu}\mathrm{Im}\Pi^{R\mu\nu}_{\gamma}(\boldsymbol{k},\omega)$ is obtained by the LE and TDGL approximations, respectively,

- the LE approximation

$$\begin{aligned} g_{\mu\nu}\mathrm{Im}\Pi^{R\mu\nu}_{\gamma}(\boldsymbol{k},\omega) =\ & \tilde{N}_\gamma \int \frac{d^3q}{(2\pi)^3}\left[A^{(1)}_{\gamma}(\boldsymbol{q}+\boldsymbol{k},\boldsymbol{q})\right]^2\left[\left(\frac{(\boldsymbol{q}+\boldsymbol{k})^2-\boldsymbol{q}^2}{\omega}\right)-(2\boldsymbol{q}+\boldsymbol{k})^2\right] \\ & \times\int\frac{d\omega'}{2\pi}\coth\frac{\omega'}{2T}\mathrm{Im}\Xi^{R}_{\gamma}(\boldsymbol{q}+\boldsymbol{k},\omega')\Big\{\mathrm{Im}\Xi^{R}_{\gamma}(\boldsymbol{q},\omega'+\omega)-\mathrm{Im}\Xi^{R}_{\gamma}(\boldsymbol{q},\omega'-\omega)\Big\}, \end{aligned} \tag{8.8}$$

  where $\Xi^{R}_{D}(\boldsymbol{q},\omega')$ and $\Xi^{R}_{S}(\boldsymbol{q},\omega')$ are Eqs. (5.32) and (5.45), and $A^{(1)}_{D}(\boldsymbol{q}+\boldsymbol{k},\boldsymbol{q})$ and $A^{(1)}_{S}(\boldsymbol{q}+\boldsymbol{k},\boldsymbol{q})$ have been defined in Eqs. (6.20) and (6.49), respectively.

- the TDGL approximation

$$\begin{aligned} g_{\mu\nu}\mathrm{Im}\Pi^{R\mu\nu}_{\gamma}(\boldsymbol{k},\omega) =\ & \tilde{N}_\gamma \int \frac{d^3q}{(2\pi)^3}\,b^2_{\gamma}\left[\left(\frac{(\boldsymbol{q}+\boldsymbol{k})^2-\boldsymbol{q}^2}{\omega}\right)-(2\boldsymbol{q}+\boldsymbol{k})^2\right] \\ & \times\int\frac{d\omega'}{2\pi}\coth\frac{\omega'}{2T}\mathrm{Im}\Xi^{R}_{\gamma}(\boldsymbol{q}+\boldsymbol{k},\omega')\Big\{\mathrm{Im}\Xi^{R}_{\gamma}(\boldsymbol{q},\omega'+\omega)-\mathrm{Im}\Xi^{R}_{\gamma}(\boldsymbol{q},\omega'-\omega)\Big\}, \end{aligned} \tag{8.9}$$

  which is obtained by using Eqs. (6.23) and (6.50) for the vertices. In this form, Eqs. (5.37) and (5.47) are utilized as the propagators for $\gamma = D$ and S, respectively.

In this Thesis, we utilize only the LE approximation (8.8) to evaluate the effect of the soft modes on the DPR since this approximation are more trusted than the TDGL approximation as described in Secs. 6.2.2 and 6.3.2.

Here, we investigate the qualitative behavior from the soft modes in the low energy/momentum region. Since real dileptons live in the time-like region $\omega > |\boldsymbol{k}|$, we consider the small-$\omega$ limit at $|\boldsymbol{k}| = 0$. From Eq. (7.2), it is found that $g_{\mu\nu}\mathrm{Im}\Pi^{R\mu\nu}(\boldsymbol{k},\omega) \sim 3\,\sigma\omega$ in this limit, and then one finds that the contribution from the soft modes to DPR (8.1) behaves

$$\frac{d^4\Gamma}{d^4k}(\boldsymbol{0},\omega) = -\frac{\alpha}{4\pi^4}\frac{T\sigma}{\omega^2}. \tag{8.10}$$

From this, it is found that the DPR due to the soft mode is divergent with $1/\omega^2$ at $\omega = 0$. As described in the previous chapter, the conductivity σ diverges as the system approaches the 2SC-PT of QCD-CP, and then the DPR in the low-energy region also prominently increases near the respective phase transitions.

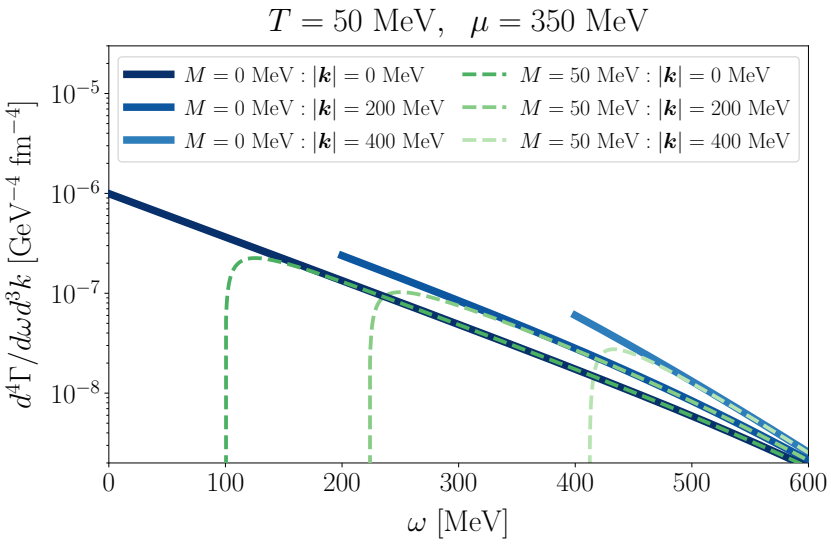

FIGURE 8.1: Comparison of the dilepton production rates per unit energy and momentum $d^4\Gamma/d\omega d^3k$ due to the massless and massive ($M = 50$ MeV) quark gases at $T = 50$ MeV and $\mu = 350$ MeV, where the former and latter ones are shown by the thick blue and thin green lines

8.1.2 Contribution of free quark gases

The results of the free quark gas system are used to compare with the ones due to the soft modes in the low energy/momentum and invariant-mass regions. However, Eq. (6.6) takes a zero value at $|\omega| < 2M$ as one can find. For that, we utilize the result at $M = 0$

$$g_{\mu\nu}\mathrm{Im}\Pi^{R\mu\nu}_{\mathrm{free}}(\boldsymbol{k},\omega)\big|_{M=0} = \frac{N_c(e_u^2+e_d^2)T}{2\pi}\frac{\omega^2-\boldsymbol{k}^2}{|\boldsymbol{k}|}\Bigg\{\theta(|\omega|-|\boldsymbol{k}|)F(\omega,|\boldsymbol{k}|) + \theta(|\boldsymbol{k}|-|\omega|)\left[F(\omega,|\boldsymbol{k}|)-\frac{\omega}{T}\right]\Bigg\} \tag{8.11}$$

for the comparison in the next sections. Here, we compare the results of the massive and massless cases in Fig. 8.1. One finds that the massless results by Eq. (8.11) become consistent with the massive ones by Eq. (6.6) as ω increases.

Let us investigate the behavior of the contribution from the free quark gases in the low energy/momentum region. Since Eq. (8.11) behaves $\sim \omega^3$ in the low ω region as shown in Eq. (7.10), we find the behavior of the contribution from the massless free quark in the small ω region as follows

$$\frac{d^4\Gamma}{d^4k}(\boldsymbol{0},\omega) = -\frac{\alpha}{12\pi^4}\frac{N_c(e_u^2+e_d^2)}{8\pi}\cosh^{-2}\frac{\mu}{2T} + \mathcal{O}(\omega^2). \tag{8.12}$$

From this, one sees that the contribution from the massless quarks is convergent at the origin of the energy/momentum plane of dileptons unlike the one from the soft modes as shown in Sec. 8.1.1. One finds that the magnitude of the contribution from the massless quarks is determined by only the μ/T ratio in the low ω-$|\boldsymbol{k}|$ region.

8.2 Energy spectra

In this section, we show the numerical results of the dilepton production rates per unit energy and momentum $d^4\Gamma/d\omega d^3k$ near the 2SC-PT and QCD-CP, where the contributions of the respective soft modes and the massless free quark gas are plotted separately.

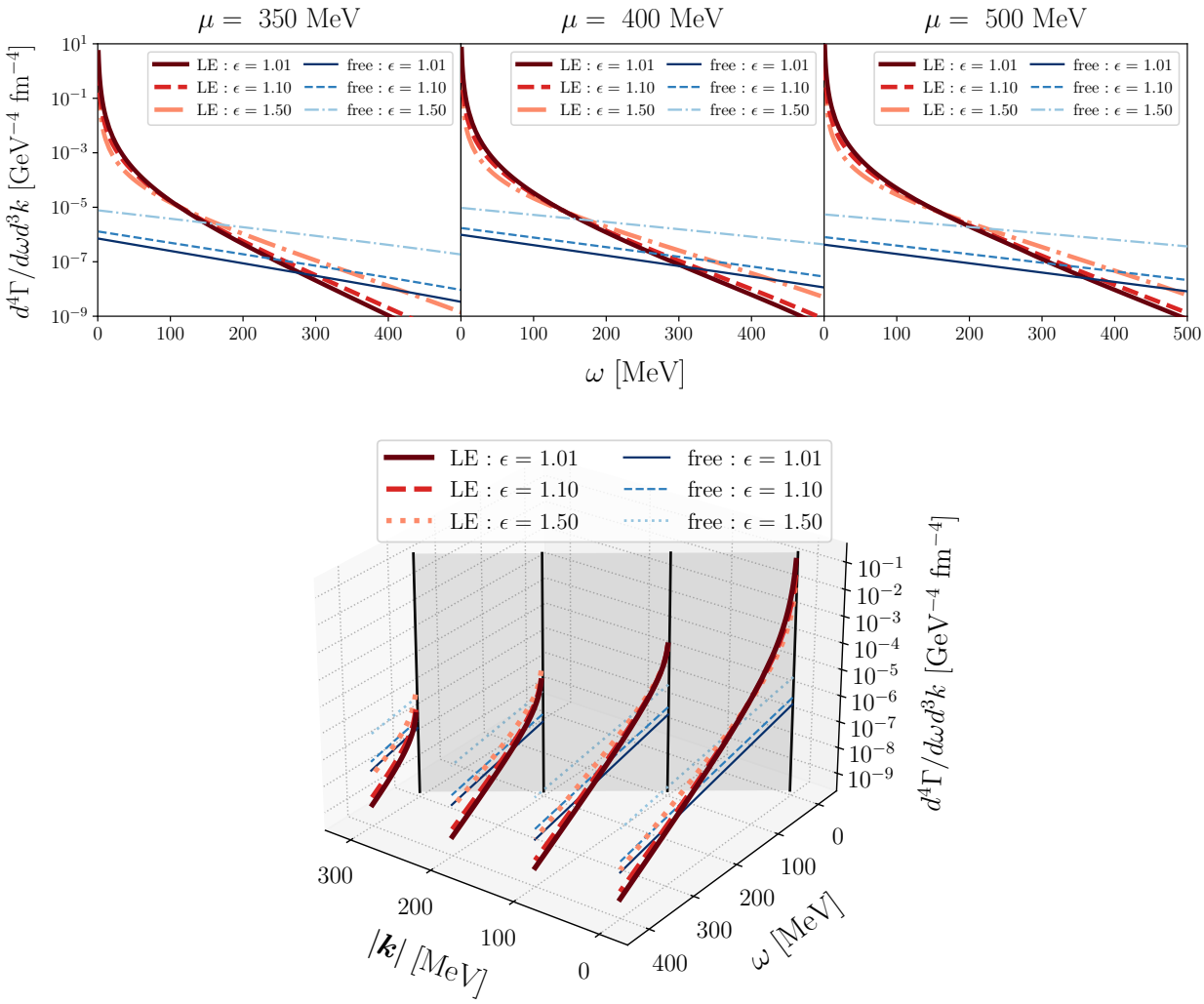

FIGURE 8.2: Dilepton production rates per unit energy and momentum $d^4\Gamma/d\omega d^3k$ for $\epsilon = (T - T_c)/T_c = 1.01, 1.10, 1.50$ with $G_D = 0.70G_S$. The thick red and thin blue lines represent the contribution of the 2SC-PT soft modes and massless free quarks. The upper panels are the results at $\boldsymbol{k} = \boldsymbol{0}$ for $\mu = 350$ MeV, 400 MeV, and 500 MeV, The lower one is the result at $\boldsymbol{k} \neq \boldsymbol{0}$ for $\mu = 350$ MeV, where the gray surface shows the light cone.

Figure 8.2 shows the contribution of the 2SC-PT soft mode for $\epsilon = (T - T_c)/T_c = 1.01, 1.10, 1.50$ with $G_D = 0.70G_S$, where the contribution of the QCD-CP is neglected. The thick red lines show the contributions of the soft mode, while the thin blue lines are the ones of the free quark gas, which are calculated with Eqs. (8.8) for $\gamma = D$ and (8.11), respectively. The upper panels are the results at $\boldsymbol{k} = \boldsymbol{0}$ for $\mu = 350$ MeV, 400 MeV, and 500 MeV. We find that the DPR is enhanced so much owing to the effect of the soft mode that it significantly goes beyond that of the free quarks in the range $\omega \lesssim 300$ MeV. The enhancement becomes more pronounced as $\epsilon \to 0$, while the enhancement within the range $\omega \lesssim 150$ MeV is found up to $\epsilon \simeq 1.50$. However, when $\epsilon \gtrsim 2.00$, since the contribution of the soft mode decreases and the one of the free quark increases owing to the factor $\cosh^{-2}(\mu/2T)$ in Eq. (8.12), the enhancement vanishes. In the lower panel of Fig. 8.2, the three-dimensional plot of DPR in the ω-$|\boldsymbol{k}|$ plane for $\mu = 350$ MeV is shown. One can see that the DPR is enhanced greatly around the origin in the ω-$|\boldsymbol{k}|$ plane, and the magnitude of the DPR becomes smaller as ω and/or $|\boldsymbol{k}|$ becomes bigger. It is noted that our present formalism is applicable for only $T > T_c$ because we do not incorporate the effect of the finite diquark gap yet.

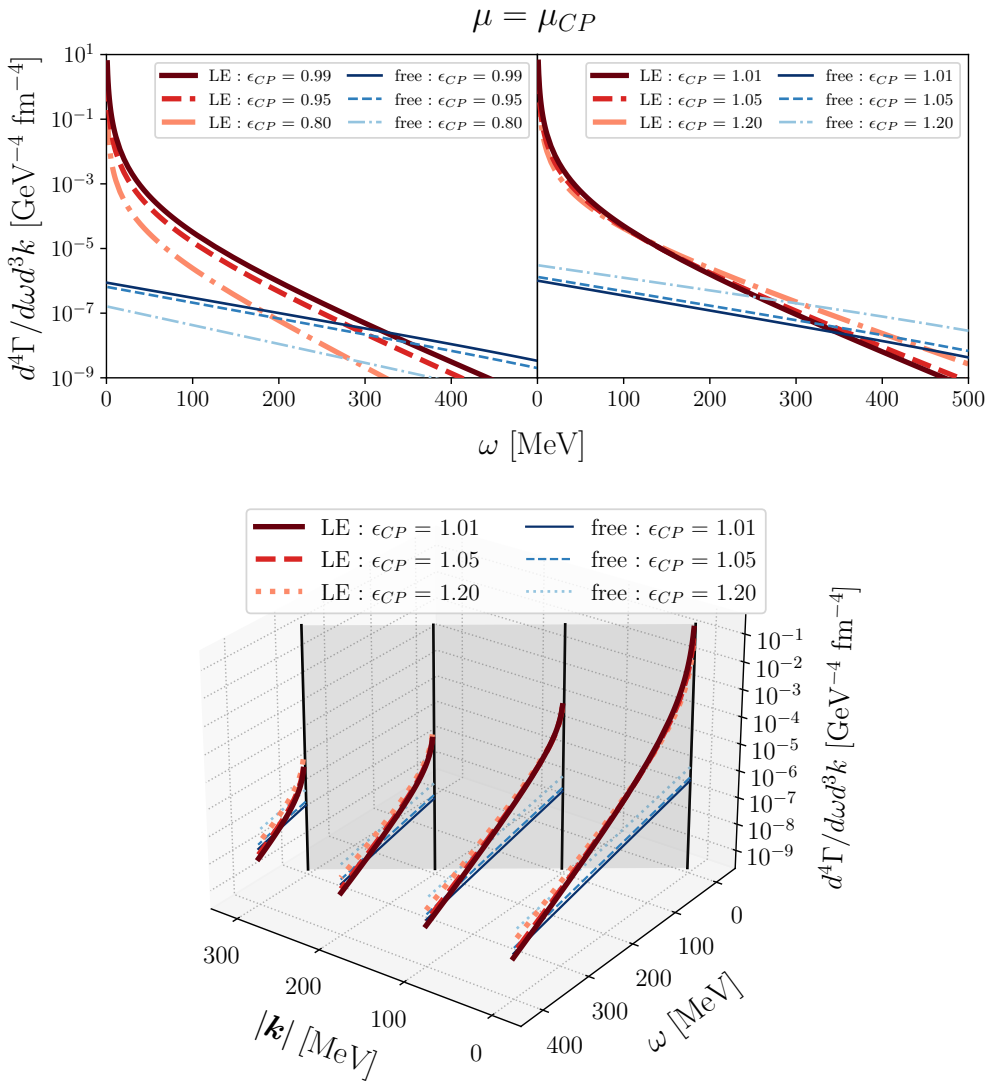

FIGURE 8.3: Dilepton production rates per unit energy and momentum $d^4\Gamma/d\omega d^3k$ at $\mu = \mu_{CP}$ with $G_D = 0.70G_S$. The thick red and thin blue lines represent the contribution of the QCD-CP soft modes and massless free quarks. The upper panels are the results at $\boldsymbol{k} = \boldsymbol{0}$, where the right and left ones show the results below and above T_{CP}, respectively, while The lower one is the result at $\boldsymbol{k} \neq \boldsymbol{0}$.

We mention that there is the study of the DPR within the CSC phases below the critical temperature [102]. In the CSC phases, it is possible that collective excitation modes due to the diquark condensate cause the enhancement of DPR in the low invariant mass region. However, such an enhancement decreases as T becomes higher and closer to the CSC-PT because they are given rise to by the finite diquark gap. On the other hand, the enhancement obtained by our calculation increase as $T \to T_c$. In this sense, our results may be useful to discuss the observability of the CSC phase in HIC experiments.

Next, we show the contribution from the QCD-PT soft mode to the DPR at $\mu = \mu_{CP}$ with $G_D = 0.70G_S$ in Fig. 8.3, which are calculated with Eqs. (8.8) for $\gamma = S$. The thick red and thin blue lines are the contribution of the QCD-CP soft modes and free quarks, respectively, where the contribution of the 2SC-PT is neglected. The upper panels are the results at $\boldsymbol{k} = \boldsymbol{0}$, in which the right and left ones show the results below and above T_{CP}, respectively. In this figure, we find that the QCD-CP soft modes also cause the enhancement of the DPR in the vicinity of the QCD CP and that the contributions from the soft modes exceed the results of the free-quark gas in the range $\omega \lesssim 250$ MeV.

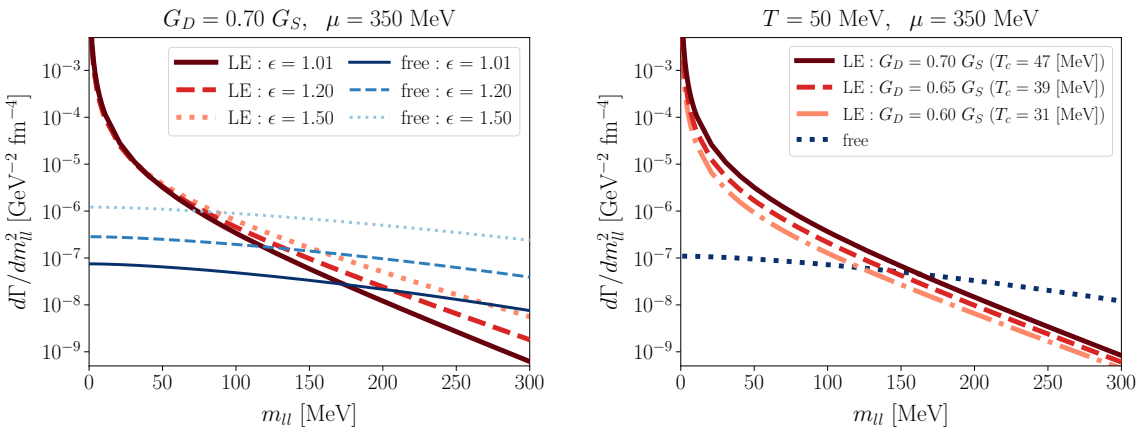

FIGURE 8.4: Invariant-mass spectrum $d\Gamma/dm_{ll}^2$ due to the 2SC-PT soft modes for $\mu = 350$ MeV. The left panel is the result for $\epsilon = 1.01, 1.20, 1.50$ with $G_D = 0.70G_S$, while the right one is the result at $T = 50$ MeV with $G_D = 0.70G_S, 0.65G_S, 0.60G_S$

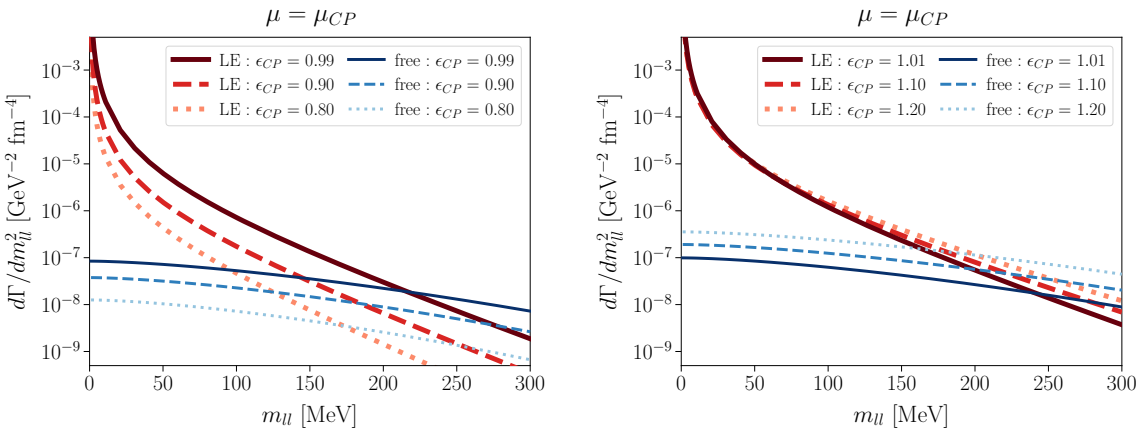

FIGURE 8.5: Invariant-mass spectrum $d\Gamma/dm_{ll}^2$ due to the QCD-CP soft modes for $\mu = \mu_{CP}$ with $G_D = 0.70G_S$. The right and left panels show the results below and above T_{CP}, respectively.

Comparing the left and right panels, it can be seen that the behavior of the contributions from the soft modes is different depending on whether T approaches T_{CP} from high-temperature or the low-temperature side. This can be explained by considering the softening of the soft mode near T_{CP} and the kinematic thermal effects. The latter means the factor $1/(e^{\omega/T} - 1) \sim T/\omega$ in Eq. (8.1). Both effects increase as T approach T_{CP} from below T_{CP}, while approaching from above T_{CP}, the competition between both effects leads to non-monotonicity. The lower panel of Fig. 8.3 shows the DPR at $\boldsymbol{k} \neq \boldsymbol{0}$. One finds significant enhancements in the lower-momentum region.

8.3 Invariant-mass spectra

In the HIC experiments, the DPR is usually measured as a function of the invariant mass m_{ll} to remove the flow effects due to motion of the matter created by the experiments, and the invariant-mass spectrum is given by

$$\frac{d\Gamma}{dm_{ll}^2} = \int d^3k \frac{1}{2\omega} \frac{d^4\Gamma}{d^4k}(\boldsymbol{k}, \omega)\Big|_{\omega=\sqrt{\boldsymbol{k}^2+4m_{ll}^2}}. \tag{8.13}$$

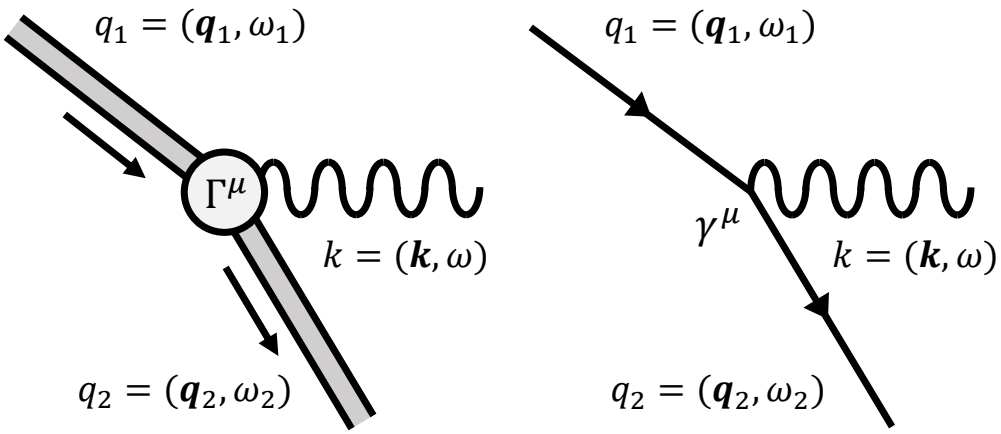

FIGURE 8.6: Diagrams representing the processes of virtual photon production through the scattering of the soft modes (right) and free quarks (left). The double lines show the soft modes of the 2SC-PT or QCD-CP, while the single and wavy lines are free quarks and photons.

In Fig. 8.4, we show the invariant-mass spectra due to the 2SC-PT soft mode. It is found that the enhancement is observed in the low invariant-mass region $m_{ll} < 100$ MeV up to $T \simeq 1.20 T_c$ in the left panel. One finds that the enhancement in the far low region of m_{ll} is mostly independent of T, which can be understood as a result of an accidental cancellation between the softening of soft mode and the thermal effect. The right panel shows the result at fixed $(T, \mu) = (90, 350)$ MeV for $G_D = 0.70 G_S$, $0.65 G_S$, and $0.60 G_S$. It shows that $d\Gamma/dm_{ll}^2$ is more enhanced for larger G_D and T_c. Since the critical temperature of 2SC-PT is sensitive to the value of the diquark coupling G_D in the NJL analysis, the DPR due to the soft mode is also sensitive to the magnitude of the coupling, while the results of the free quark gases are independent of G_D.

Figure 8.5 shows the result of $d\Gamma/dm_{ll}^2$ due to the QCD-CP soft mode at $\mu = \mu_{CP}$. We find that the contribution of the soft modes is conspicuous in the low invariant-mass region $m_{ll} \simeq 150$ MeV. In the case of $T > T_{CP}$, the little T dependence is seen in the low-mass region of $m_{ll} < 50$ MeV, whose behavior can be explained with the same reason as the 2SC-PT case.

Here, we discuss the production mechanism of the dileptons due to the soft modes by comparing the case of free quark gases. In our formalism, the virtual photons due to the soft modes are dominantly emitted through the processes obtained by cutting the AL terms that have been described by Fig. 6.2 (a) in the case of the 2SC-PT and Fig. 6.5 (a, b) in the case of the QCD-CP, i.e. the scattering of the soft modes shown in the left panel of Fig. 8.6, since the contributions of MT and DOS terms cancel out as in Eqs. (6.29) and (6.55). Then, the enhancements of dilepton productions in the low energy/momentum region within the time-like region are understood through these processes and the fact that the prominent strength of the soft modes is concentrating on the low energy/momentum region as shown in Fig. 5.4. However, since most of the strength lives in the space-like region, we have to give a more close explanation. In the process of the left panel of Fig. 8.6, the energy/momentum of the virtual photons $k = (\boldsymbol{k}, \omega)$ can be in time-like $|\omega| > |\boldsymbol{k}|$, since the absolute value of the momentum $\boldsymbol{k} = \boldsymbol{q}_1 - \boldsymbol{q}_2$ can be taken arbitrarily small keeping $\omega = \omega_1 - \omega_2$ finite, where $q = (\boldsymbol{q}, \omega)$ is of the soft modes. This kinematics is contrasted to the scattering process of free quarks shown in the right panel of Fig. 8.6, in which the produced virtual photon is always in the space-like region $|\omega| < |\boldsymbol{k}|$.

We mention that it is necessary to investigate the dilepton production yield integrated over the entire space-time evolution in HIC and compare it with the experimental data in order to clarify that these enhancements can serve as signals of the 2SC-PT and QCD-PT in HIC experiments. Then, as its first step, we integrated the production rate due to the soft modes with the isentropic expansion trajectory, whose study is based on Res. [103].

Chapter 9

Summary

We have investigated the effects of the 2SC-PT and QCD-CP soft modes on the dilepton production rates, the electric conductivity σ and the associated relaxation time τ_σ in the two-flavor NJL model. We considered the AL, MT, and DOS terms in order to incorporate the effect of the respective soft modes into the photon self-energy in Chap. 6. These terms constitute the self-energy in a gauge invariant manner including the effects of the soft modes at the mean-field level. Moreover, we have developed the approximation method for the AL, MT, and DOS terms such that the set of their terms keep to satisfy the Ward identity.

In this Thesis, we first have shown that σ and τ_σ are enhanced near the 2SC-PT and QCD-CP with the power-like behavior in Chap. 7. The critical exponents have been calculated analytically. We have shown that σ and τ_σ diverge at the 2SC-PT and QCD-CP with different critical exponents and that the origin of the difference comes from the different nature of the soft modes. After that, in Chap. 8, we have shown that the DPR is strongly enhanced in comparison with the free-quark gases in the low energy and low invariant-mass regions $m_{ll} \lesssim 200$ MeV near the respective phase transitions due to the formation of the soft modes within quite a wide T range.

We would like to say that it is worthwhile to attempt experimental measurements of dileptons in the ultra-low mass regions in order to investigate the possible enhancement of the DPR in HIC. If the enhancement obtained in our study is confirmed, this could provide experimental evidence for the existence of the CSC (2SC) phase and QCD-CP. These measurements would be an interesting target of the HIC experiments at future experimental facilities [104] and promote actively the understanding of phase structure in dense QCD.

On the other hand, there are many issues to be resolved to make such measurements meaningful. Since observed yield of the dilepton production in the HIC is a superposition of those due to various mechanisms in the space-time evolution of created matter, it is necessary to 'disentangle' the total yield observed in the experiments into those with the origins of respective productions. For that, we have to calculate the production rate from other mechanism such as the hadronic scenarios [105] and the perturbative calculation of QCD [106, 71, 107] including the one that we investigated in this Thesis and estimate the magnitudes of their rates to compare them each other. Additionally, it is necessary to apply their results to the dynamical transport model, e.g. [108], and compute the dilepton 'yield' expected to be finally observed in the experiments since experimental measurements are total amount of dileptons as described above.

Of course, it is not an easy experiment to measure the DPR in the far low invariant-mass region $m_{ll} \lesssim 200$ MeV. This is because di-electrons are only observable in this energy or mass range among dileptons and they are severely contaminated by the Dalitz decays. Therefore, the high-precision measurements are required to extract such interesting medium effects. However, these challenging tasks and issues would be resolved at the future HIC programs in GSI-FAIR, NICA-MPD and J-PARC-HI that are designed to carry out high-precision and -statistics experiments for dense matter. Additionally, the experiments that aim to explore for the ultra-low energy/momentum or invariant mass region of DPR are also being planed. They are very interesting because they will lead to the observation of the conductivity [82].

We have interesting extensions in our study. First, our formalism is not applicable to the 2SC phase. To investigate the behavior of the DPR and associated coefficients inside the 2SC phase, the

formalism has to be extended to incorporate the effects of the finite diquark gap. It is interesting to investigate the critical phenomena when T approaches T_c from below. Another interesting subject is to investigate the coupling between the soft mode of the QCD-CP and the density fluctuations. It is known that the soft mode of the QCD-CP is a diffusive mode due to the coupling, while this effect is not included in our formalism. In the NJL model, this effect can be described by the vector interaction. Investigating its effects on the DPR and transport coefficients is another important extension. We also note that our analysis is not self-consistent in the sense that the effects of the soft modes are not incorporated into the thermodynamic potential nor quark propagator composing the soft modes. Because of this inconsistency, we did not investigate the proper quark-number susceptibility. Once the susceptibility is obtained, one can study the behavior of the diffusion coefficient and the velocity of the shock near the critical point. We leave these interesting analyses for future studies.

Appendix A

Three-momentum cutoff scheme

We describe the three-momentum cutoff scheme determining the scalar coupling constant G_S and cutoff Λ with the given current quark mass m.

The pion mass m_π in the vacuum, i.e. at $T = \mu = 0$, is given by the pole of the retarded Green's function of the pseudoscalar field $\hat{\boldsymbol{\pi}}(\boldsymbol{x}, t) = \bar{\psi}(\boldsymbol{x}, t) i\gamma_5 \boldsymbol{\tau} \psi(\boldsymbol{x}, t)$ under the on-shell condition

$$D_{PS}^{R\ -1}(k)|_{k^2=\omega^2-\boldsymbol{k}^2=m_\pi^2} = 0. \tag{A.1}$$

In this scheme, the response function is evaluated by the RPA

$$\mathcal{D}_{PS}(k) = \mathcal{D}_{PS}(\boldsymbol{k}, \omega) = \frac{1}{G_S^{-1} + \mathcal{Q}_{PS}(\boldsymbol{k}, \omega)}, \tag{A.2}$$

$$\begin{aligned} \mathcal{Q}_{PS}(k) = \mathcal{Q}_{PS}(\boldsymbol{k}, \omega) &= \int d^3x dt\, e^{i\omega t - i\boldsymbol{k}\cdot\boldsymbol{x}} \left\langle T\hat{\boldsymbol{\pi}}(\boldsymbol{x}, t) \cdot \hat{\boldsymbol{\pi}}(\boldsymbol{0}, 0) \right\rangle \\ &= -2 \int \frac{d^3p}{(2\pi)^3} \int \frac{dp_0}{2\pi i} \mathrm{Tr}_{f,c,d}[(\mathcal{G}_F(k+p) i\gamma_5 \boldsymbol{\tau}) \cdot (\mathcal{G}_F(p) i\gamma_5 \boldsymbol{\tau})], \end{aligned} \tag{A.3}$$

where $\mathcal{G}_F(p)$ is the Feynman propagator for free quarks

$$\mathcal{G}_F(p) = \mathcal{G}_F(\boldsymbol{p}, p_0) = \frac{i}{\not{p} - M + i\eta} = \frac{i(\not{p} + M)}{p_0^2 - e_{\boldsymbol{p}}^2 + i\eta} = \frac{i(\not{p} + M)}{(p_0 - e_{\boldsymbol{p}} + i\eta)(p_0 + e_{\boldsymbol{p}} - i\eta)}, \tag{A.4}$$

where $e_{\boldsymbol{p}} = \sqrt{\boldsymbol{p}^2 + M^2}$. In the present formulation, the retarded function is obtained by closing the contour of the p_0-integral in the upper half-plane C_+. The retarded one-loop pseudoscalar correlation function (A.3) is

$$\begin{aligned} Q_{PS}^R(\boldsymbol{k}, \omega) &= -2N_f N_c \int \frac{d^3p}{(2\pi)^3} \oint_{C_+} \frac{dp_0}{2\pi} \mathrm{Tr}_d[\mathcal{G}_F(\boldsymbol{k}+\boldsymbol{p}, \omega + p_0) i\gamma^5 \mathcal{G}_F(\boldsymbol{p}, p_0) i\gamma^5] \\ &= -2N_f N_c \int \frac{d^3p}{(2\pi)^3} \frac{1}{e_1 e_2} \oint_{C_+} \frac{dp_0}{2\pi i} \sum_{s,t=\pm} st \frac{p_0(\omega + p_0) - (e_1^2 + e_2^2 - \boldsymbol{k}^2)/2}{(p_0 + \omega - s(e_1 - i\eta))(p_0 + t(e_2 - i\eta))} \\ &= -N_f N_c \int \frac{d^3p}{(2\pi)^3} \frac{1}{e_1 e_2} \sum_{s=\pm} s \frac{(e_1 + e_2)^2 - \boldsymbol{k}^2}{e_1 + e_2 - s\omega - i\eta}. \end{aligned} \tag{A.5}$$

where $e_1 = \sqrt{\boldsymbol{p}^2 + M^2}$ and $e_2 = \sqrt{(\boldsymbol{p} + \boldsymbol{k})^2 + M^2}$. The momentum integral can be converted as follows

$$\int \frac{d^3p}{(2\pi)^3} \frac{1}{e_1 e_2} = \frac{1}{(2\pi)^2} \int p^2 dp \int_{-1}^{1} d(\cos\theta) = \frac{1}{2(2\pi)^2 |\boldsymbol{k}|} \int_{\lambda(|\boldsymbol{k}|,0)}^{\tilde{\Lambda}} dE_1 \int_{-\lambda(|\boldsymbol{k}|,E_1)}^{+\lambda(|\boldsymbol{k}|,E_1)} dE_2, \tag{A.6}$$

$$\lambda(|\boldsymbol{k}|, \omega) = |\boldsymbol{k}| \sqrt{1 - 4M^2/(\omega^2 - \boldsymbol{k}^2)}, \quad \tilde{\Lambda}(\boldsymbol{k}) = 2\sqrt{\Lambda^2 + M^2 + \boldsymbol{k}^2/4}, \tag{A.7}$$

where it is noted that the UV cutoff $\tilde{\Lambda}(\boldsymbol{k})$ is different from $\bar{\Lambda}$ in Eq. (5.18).

The imaginary part of Eq (A.5) can be calculated analytically as follows

$$\mathrm{Im}Q^R_{\mathrm{PS}}(\boldsymbol{k},\omega) = -\frac{N_f N_c}{4\pi}\theta\big(4(\Lambda^2+M^2)-k^2\big)\theta\big(k^2-4M^2\big)\,k^2\sqrt{1-\frac{4M^2}{k^2}}, \tag{A.8}$$

where Eq. (5.21) has been used. The support of $\mathrm{Im}Q^R_{\mathrm{PS}}(\boldsymbol{k},\omega)$ exists only in $k^2 > M^2$ (the time-like region) in the vacuum, and then, the real part of Eq (A.5) is

$$\begin{aligned}\mathrm{Re}Q^R_{\mathrm{PS}}(\boldsymbol{k},\omega) &= -\frac{N_f N_c}{4\pi^2|\boldsymbol{k}|}\int_{\lambda(|\boldsymbol{k}|,0)}^{\tilde{\Lambda}} dE_1 \int_{-\lambda(|\boldsymbol{k}|,E_1)}^{+\lambda(|\boldsymbol{k}|,E_1)} dE_2\,\frac{E_1(E_1^2-\boldsymbol{k}^2)}{E_1^2-\omega^2}\\ &= -\frac{N_f N_c}{\pi^2}\int_0^{\Lambda} p^2dp\,\frac{\sqrt{p^2+M^2}}{p^2+M^2-k^2/4}.\end{aligned} \tag{A.9}$$

To obtain Eq. (A.9) from Eq. (A.5), the variable transformation $p^2 = (E_1^2-\boldsymbol{k}^2-4M^2)/4$ has been used. The fact that $Q^R_{\mathrm{PS}}(\boldsymbol{k},\omega)$ is the function of $k^2=\omega^2-\boldsymbol{k}^2$ is owing to introducing the cutoff $\tilde{\Lambda}(\boldsymbol{k})$. Therefore, substituting Eqs. (A.8) and (A.9) to Eq. (A.3), we obtain the condition to determine m_π in the RPA from Eq. (A.1) as follows

$$\mathrm{Im}Q^R_{PS}(\boldsymbol{k},\omega)|_{k^2=m_\pi^2} = \frac{N_f N_c}{4\pi}\theta\big(\tilde{\Lambda}^2-m_\pi^2\big)\theta\big(m_\pi^2-4M^2\big)\,m_\pi^2\sqrt{1-\frac{4M^2}{m_\pi^2}} = 0, \tag{A.10}$$

$$\frac{1}{G_S}+\mathrm{Re}Q^R_{PS}(\boldsymbol{k},\omega)|_{k^2=m_\pi^2} = \frac{1}{G_S}-\frac{N_f N_c}{\pi^2}\int_0^{\Lambda} p^2dp\,\frac{\sqrt{p^2+M^2}}{p^2+M^2-m_\pi^2/4} = 0. \tag{A.11}$$

The pion decay constant f_π is described by the process that the on-shell pion decays to a quark and anti-quark pair via the pseudoscalar channel and the pair annihilates through the axial current. In the current formulation, the constant is defined by

$$f_\pi k_\mu = -\int\frac{d^3p}{(2\pi)^3}\oint_{C_+}\frac{dp_0}{2\pi i}\,\mathrm{Tr}_{f,c,d}[\mathcal{G}_F(p)i\gamma_\mu\gamma_5\tau_\mp\mathcal{G}_F(k+p)iG_{\pi\text{-}q}(k^2)\gamma_5\tau_\pm]|_{k^2=m_\pi^2}, \tag{A.12}$$

where $\tau_\pm=\tau_1\pm i\tau_2$, and $G_{\pi\text{-}q}(k^2)$ is the momentum-dependent pion–quark coupling that is given in terms of the retarded Green's function of $\hat{\boldsymbol{\pi}}(\boldsymbol{x},t)$ by

$$\begin{aligned}G^2_{\pi\text{-}q}(k^2) &= \frac{d}{dk^2}{D^R_{PS}}^{-1}(\boldsymbol{k},\omega)\\ &= \frac{d}{dk^2}Q^R_{PS}(\boldsymbol{k},\omega).\end{aligned} \tag{A.13}$$

From Eq. (A.12), the explicit form of the constant f_π is given by

$$\begin{aligned}f_\pi &= -\frac{N_f N_c}{2}\,G_{\pi\text{-}q}(k^2)\int\frac{d^3p}{(2\pi)^3}\oint_{C_+}\frac{dp_0}{2\pi i}\mathrm{Tr}_d[\mathcal{G}_F(p)i\gamma_\mu\gamma_5\mathcal{G}_F(k+p)i\gamma_5]\,\frac{k^\mu}{k^2}\Big|_{k^2=m_\pi^2}\\ &= -\frac{N_f N_c}{2}\,G_{\pi\text{-}q}(k^2)\int\frac{d^3p}{(2\pi)^3}\frac{1}{e_1e_2}\oint_{C_+}\frac{dp_0}{2\pi i}\sum_{s,t=\pm}\frac{-stM}{(p_0+\omega-s(e_1-i\eta))(p_0+t(e_2-i\eta))}\Big|_{k^2=m_\pi^2}\\ &= M\,G_{\pi\text{-}q}(m_\pi^2)\,d_\pi(m_\pi^2)\end{aligned} \tag{A.14}$$

with

$$d_\pi(k^2) = \frac{N_f N_c}{2}\int\frac{d^3p}{(2\pi)^3}\frac{1}{e_1e_2}\oint_{C_+}\frac{dp_0}{2\pi i}\sum_{s,t=\pm}\frac{st}{(p_0+\omega-s(e_1-i\eta))(p_0+t(e_2-i\eta))}, \tag{A.15}$$

which is calculated as follows

$$\mathrm{Im}d_\pi(k^2) = \frac{N_f N_c}{16\pi}\theta(\bar{\Lambda}^2 - m_\pi^2)\theta(m_\pi^2 - 4M^2)\sqrt{1-\frac{4M^2}{m_\pi^2}}, \tag{A.16}$$

$$\mathrm{Re}d_\pi(k^2) = \frac{N_f N_c}{4\pi^2}\int_0^\Lambda p^2 dp\,\frac{1}{\sqrt{p^2+M^2}}\frac{1}{p^2+M^2-m_\pi^2/4}. \tag{A.17}$$

Since the constant f_π is a real number, the imaginary part of $d_\pi(m_\pi^2)$ in Eq. (A.14) has to take zero value. From this, it is found that the pion mass m_π is lower than $2M$. Then, the condition for f_π is

$$f_\pi = M\,G_{\pi\text{-}q}(m_\pi^2)\,\mathrm{Re}d_\pi(m_\pi^2) \quad \text{with} \quad m_\pi < 2M. \tag{A.18}$$

The scalar coupling constant G_S and cutoff Λ are included within the integrals in Eqs. (A.11) and (A.18), and they are determined so as to give the values $m_\pi = 138$ MeV and $f_\pi = 93$ MeV with the conditions (A.11) and (A.18).

Appendix B

Expansion coefficients of soft modes

B.1 Coefficients of the 2SC-PT soft mode

In this section, we give the explicit form of the expansion coefficients in the LE and TDGL approximations for the 2SC-PT soft modes, which are given by Eqs (5.33) and (5.35).

First of all, we introduce the following notations

$$\int_{D\text{-time}} \frac{d\omega'}{\omega'} = \left[\int_{+\lambda(|\boldsymbol{k}|,0)-2\mu}^{+\bar{\Lambda}-2\mu} + \int_{-\bar{\Lambda}-2\mu}^{-\lambda(|\boldsymbol{k}|,0)-2\mu} \right] \frac{d\omega'}{\omega'}, \tag{B.1}$$

$$\int_{D\text{-space}} \frac{d\omega'}{\omega'} = \int_{-\lambda(|\boldsymbol{k}|,\bar{\Lambda})-2\mu}^{+\lambda(|\boldsymbol{k}|,\bar{\Lambda})-2\mu} \frac{d\omega'}{\omega'}, \tag{B.2}$$

$$F_D'(x,y) = \frac{\partial F_D(x,y)}{\partial x} = \frac{1}{2T} \sum_{s=\pm} s \tanh \frac{x+sy}{4T}, \tag{B.3}$$

where $F_D(x,y)$ has been defined by Eq. (5.24) and the integrals of Eqs. (B.1) and (B.2) appears in $\mathrm{Re}Q_D^R(\boldsymbol{k},\omega)$. Also, in this section, the simplified TDGL coefficients are calculated explicitly.

B.1.1 LE approximation

Firstly, from Eq. (5.33), we obtain

$$\begin{aligned} A_D(\boldsymbol{k}) =& \frac{1}{G_D} + \mathrm{Re}Q_D^R(\boldsymbol{k},0) \\ =& \frac{1}{G_D} - \frac{N_f(N_c-1)T}{4\pi^2} \Bigg\{ \int_{D\text{-time}} \frac{d\omega'}{\omega'} \frac{(\omega'+2\mu)^2-\boldsymbol{k}^2}{|\boldsymbol{k}|} F_D\big(\omega', \lambda(|\boldsymbol{k}|,\omega'+2\mu)\big) \\ &+ \int_{D\text{-space}} \frac{d\omega'}{\omega'} \frac{(\omega'+2\mu)^2-\boldsymbol{k}^2}{|\boldsymbol{k}|} \Big(F_D\big(\omega', \lambda(|\boldsymbol{k}|,\omega'+2\mu)\big) - F_D\big(\omega',\bar{\Lambda}\big) \Big) \Bigg\}. \end{aligned} \tag{B.4}$$

In order to derive the explicit form of C_D in Eq. (5.33), we calculate the ω-derivatives of $Q_D^R(\boldsymbol{k},\omega)$. Through integration by parts, we obtain the real part as follows

$$\begin{aligned} \frac{\partial \mathrm{Re}Q_D^R(\boldsymbol{k},\omega)}{\partial\omega}\Big|_{\omega=0} =& \frac{N_f(N_c-1)T}{4\pi} \Bigg\{ \frac{\bar{\Lambda}^2-\boldsymbol{k}^2}{|\boldsymbol{k}|} \sum_{s=\pm} s \frac{F_D\big(\bar{\Lambda}-2s\mu, \lambda(|\boldsymbol{k}|,\bar{\Lambda})\big)}{\bar{\Lambda}-2s\mu} \\ &- \int_{D\text{-time}} \frac{d\omega'}{\omega'} \left(\frac{2(\omega'+2\mu)}{|\boldsymbol{k}|} F_D\big(\omega', \lambda(|\boldsymbol{k}|,\omega'+2\mu)\big) + \frac{(\omega'+2\mu)^2-\boldsymbol{k}^2}{|\boldsymbol{k}|} \frac{\partial F_D\big(\omega', \lambda(|\boldsymbol{k}|,\omega'+2\mu)\big)}{\partial\omega'} \right) \\ &- \int_{D\text{-space}} \frac{d\omega'}{\omega'} \left(\frac{2(\omega'+2\mu)}{|\boldsymbol{k}|} F_D\big(\omega', \lambda(|\boldsymbol{k}|,\omega'+2\mu)\big) + \frac{(\omega'+2\mu)^2-\boldsymbol{k}^2}{|\boldsymbol{k}|} \frac{\partial F_D\big(\omega', \lambda(|\boldsymbol{k}|,\omega'+2\mu)\big)}{\partial\omega'} \right. \\ &\left. - \frac{2(\omega'+2\mu)}{|\boldsymbol{k}|} F_D\big(\omega',\bar{\Lambda}\big) - \frac{(\omega'+2\mu)^2-\boldsymbol{k}^2}{|\boldsymbol{k}|} F_D'\big(\omega',\bar{\Lambda}\big) \right) \Bigg\}, \end{aligned} \tag{B.5}$$

where

$$\frac{\partial F_D\big(\omega',\lambda(|\boldsymbol{k}|,\omega'+2\mu)\big)}{\partial\omega'} = F_D'\big(\omega',\lambda(|\boldsymbol{k}|,\omega'+2\mu)\big) + F_D\big(\omega',\lambda(|\boldsymbol{k}|,\omega'+2\mu)\big)\frac{\partial\lambda(|\boldsymbol{k}|,\omega'+2\mu)}{\partial\omega'},$$
$$\frac{\partial\lambda(|\boldsymbol{k}|,\omega'+2\mu)}{\partial\omega'} = \frac{|\boldsymbol{k}|^2}{\lambda(|\boldsymbol{k}|,\omega'+2\mu)}\frac{4M^2(\omega'+2\mu)}{((\omega'+2\mu)^2-|\boldsymbol{k}|^2)^2}.$$

Also, the imaginary part is

$$\left.\frac{\partial \mathrm{Im}Q_D^R(\boldsymbol{k},\omega)}{\partial\omega}\right|_{\omega=0} = -\frac{N_f(N_c-1)T}{4\pi}\frac{4\mu^2-\boldsymbol{k}^2}{|\boldsymbol{k}|}F_D'\big(0,\lambda(|\boldsymbol{k}|,2\mu)\big), \tag{B.6}$$

where it is noted that Eq. (B.6) is the result that is valid for only $|\boldsymbol{k}|<2\sqrt{\mu^2-M^2}$ since the strength of the 2SC-PT soft mode exists in $\lambda(|\boldsymbol{k}|,0)-2\mu<\omega$. Therefore, by taking the limit $|\boldsymbol{k}|\to 0$, one finds the explicit forms of C_D

$$\begin{aligned}
\mathrm{Re}C_D &= \left.\frac{\partial \mathrm{Re}Q_D^R(\boldsymbol{k},\omega)}{\partial\omega}\right|_{\omega=|\boldsymbol{k}|=0} \\
&= \frac{N_f(N_c-1)}{4\pi}\Bigg\{\bar{\Lambda}^2\sqrt{1-\frac{4M^2}{\bar{\Lambda}^2}}\sum_{s=\pm}\frac{s}{\bar{\Lambda}-2s\mu}\tanh\frac{\bar{\Lambda}-2s\mu}{4T} \\
&\qquad -\left[\int_{+2M-2\mu}^{+\bar{\Lambda}-2\mu}+\int_{-\bar{\Lambda}-2\mu}^{-2M-2\mu}\right]\frac{d\omega'}{\omega'}\Bigg(2\frac{(\omega'+2\mu)^2-2M^2}{\sqrt{(\omega'+2\mu)^2-4M^2}}\tanh\frac{\omega'}{4T} \\
&\qquad\qquad +\frac{\omega'+2\mu}{4T}\sqrt{(\omega'+2\mu)^2-4M^2}\cosh^{-2}\frac{\omega'}{4T}\Bigg)\Bigg\},
\end{aligned} \tag{B.7}$$

$$\begin{aligned}
\mathrm{Im}C_D &= \left.\frac{\partial \mathrm{Im}Q_D^R(\boldsymbol{k},\omega)}{\partial\omega}\right|_{\omega=|\boldsymbol{k}|=0} \\
&= -\frac{N_f(N_c-1)T}{4\pi}\frac{\mu}{T}\sqrt{\mu^2-M^2} \quad \text{for} \quad |\boldsymbol{k}|<2\sqrt{\mu^2-M^2}.
\end{aligned} \tag{B.8}$$

B.1.2 TDGL approximation

Next, we give the explicit form of the TDGL coefficients in Eq. (5.35). Since $a_D = A_D(\boldsymbol{0})$, we can obtain the explicit form of a_D by using Eq. (B.4) as follows

$$\begin{aligned}
a_D = \frac{1}{G_D} - \frac{N_f(N_c-1)}{4\pi^2}\Bigg\{&\left[\int_{+2M-2\mu}^{+\bar{\Lambda}-2\mu}+\int_{-\bar{\Lambda}-2\mu}^{-2M-2\mu}\right]\frac{d\omega'}{\omega'}(\omega'+2\mu) \\
&\times\sqrt{(\omega'+2\mu)^2-4M^2}\tanh\frac{\omega'}{4T}\Bigg\},
\end{aligned} \tag{B.9}$$

which is consistent with the Thouless criterion (4.40). Also, c_D is

$$\mathrm{Re}c_D = \mathrm{Re}C_D, \tag{B.10}$$
$$\mathrm{Im}c_D = \mathrm{Im}C_D. \tag{B.11}$$

On the other hand, the coefficient b_D is difficult to calculate it analytically. For that, we compute b_D numerically.

We have considered the more simplified TDGL approximation (5.38) at the end of Sec. 5.3.1. In this calculation, we set $M=0$, and then take the limit $\Lambda\to\infty$ to compute the T and μ dependence of $\tilde{a}_D$, $\tilde{b}_D$, and $\tilde{c}_D$ analytically. In the following, we give the explicit forms of these coefficients.

First of all, using Eq. (B.9), $\tilde{a}_D = T\partial Q_D^R(\mathbf{0},0)/\partial T|_{T=T_c}$ is given by

$$\begin{aligned}\tilde{a}_D &= \frac{N_f(N_c-1)}{2\pi^2 T}\int_{-\Lambda-\mu}^{\Lambda-\mu} dp(p+\mu)^2\cosh^{-2}\frac{p}{2T}\Big|_{T=T_c} \\ &\xrightarrow[\lambda\to\infty]{} \frac{N_f(N_c-1)}{2\pi^2 T}(C_2(T)+2\mu C_1(T)+\mu^2 C_0(T))\Big|_{T=T_c},\end{aligned} \tag{B.12}$$

with $C_n(T) = \int_{-\infty}^{\infty} dp p^n \cosh^{-2}(p/2T)$. Equation (5.39) is then obtained by substituting $C_2(T) = 4\pi^2T^3/3$, $C_1(T) = 0$, and $C_0(T) = 4T$.

Next, from Eq. (5.33), b_D is represented explicitly as

$$\begin{aligned}b_D = \frac{N_f(N_c-1)}{4\pi^2}\Bigg(&\frac{4T}{3\mu}\sum_{s=\pm} s\log\cosh\frac{\Lambda-s\mu}{2T} + \int_{-\Lambda-\mu}^{\Lambda-\mu}\frac{dp}{p}\tanh\frac{p}{2T} \\ &+\frac{1}{12T^2}\int_{-\Lambda-\mu}^{\Lambda-\mu}\frac{dp}{p}(p+\mu)^2\tanh\frac{p}{2T}\cosh^{-2}\frac{p}{2T}\Bigg).\end{aligned} \tag{B.13}$$

In the limit $\Lambda\to\infty$, the first term in the bracket in Eq. (B.13) becomes

$$\lim_{\Lambda\to\infty}\frac{4T}{3\mu}\sum_{s=\pm} s\log\cosh\frac{\Lambda-s\mu}{2T} = \lim_{\Lambda\to\infty}\frac{4T}{3\mu}\left(\frac{\Lambda-\mu}{2T}-\frac{\Lambda+\mu}{2T}\right) = -\frac{4}{3}. \tag{B.14}$$

The second term includes a logarithmic divergence in this limit. In order to isolate the divergence, we rewrite this term by the integral by parts as

$$\int_{-\Lambda-\mu}^{\Lambda-\mu}\frac{dp}{p}\tanh\frac{p}{2T} = \sum_{s=\pm}\log\frac{\Lambda-s\mu}{2T}\tanh\frac{\Lambda-s\mu}{2T} - \frac{1}{2T}\int_{-\Lambda-\mu}^{\Lambda-\mu} dp\log\frac{|p|}{2T}\cosh^{-2}\frac{p}{2T}.$$

Then, using the formulas $\int_{-\infty}^{\infty} dx\log x\cosh^{-2}x = -2\gamma_{\rm E}+2\log\pi/4 \simeq -1.63756$ and $\lim_{\Lambda\to\infty}\tanh((\Lambda\mp\mu)/2T) = 1$, we obtain

$$\lim_{\Lambda\to\infty}\int_{-\Lambda-\mu}^{\Lambda-\mu}\frac{dp}{p}\tanh\frac{p}{2T} = \log\frac{\Lambda^2-\mu^2}{4T^2}+2\gamma_{\rm E}-2\log\frac{\pi}{4}. \tag{B.15}$$

The third term is convergent in the limit $\Lambda\to\infty$ and calculated to be

$$\lim_{\Lambda\to\infty}\int_{-\Lambda-\mu}^{\Lambda-\mu}\frac{dp}{p}(p+\mu)^2\tanh\frac{p}{2T}\cosh^{-2}\frac{p}{2T} = T_1(T)+2\mu T_0(T)+\mu^2 T_{-1}(T),$$

with $T_n(T) = \int_{-\infty}^{\infty} dx p^n\tanh(p/2T)\cosh^{-2}(p/2T)$. The values $T_1(T) = 4T^2$, $T_0(T) = 0$, and $T_{-1}(T) = 7\zeta(3)/\pi^2$ together with Eq. (B.13) and (B.14) lead to Eq. (5.43).

Equation (5.41) is also obtained by using Eq. (B.7)

$$\begin{aligned}{\rm Rec}_D = \frac{N_f(N_c-1)}{4\pi^2}\Bigg(&2\Lambda^2\sum_{s=\pm}\frac{s}{\Lambda-s\mu}\tanh\frac{\Lambda-s\mu}{2T} \\ &-4\int_{-\Lambda-\mu}^{\Lambda-\mu}\frac{dp}{p}(p+\mu)\tanh\frac{p}{2T}-\frac{1}{T}\int_{-\Lambda-\mu}^{\Lambda-\mu}\frac{dp}{p}(p+\mu)^2\cosh^{-2}\frac{p}{2T}\Bigg) \\ \xrightarrow[\lambda\to\infty]{}\frac{N_f(N_c-1)}{4\pi^2}\Bigg(&4\mu\left[1-\log\frac{\Lambda^2-\mu^2}{4T^2}-2\gamma_{\rm E}+2\log\frac{\pi}{4}\right] \\ &-\frac{1}{T}(C_1(T)+2\mu C_0(T)+\mu^2 C_{-1}(T))\Bigg),\end{aligned} \tag{B.16}$$

where $C_1(T) = C_{-1}(T) = 0$ and $C_0(T) = 4T$. Also, Eq. (5.42) is obtained from at $M = 0$

$$\mathrm{Im}c_D = -\frac{N_f(N_c-1)T}{4\pi}\frac{\mu^2}{T} \quad \text{for} \quad |\boldsymbol{k}| < 2\sqrt{\mu^2 - M^2}. \tag{B.17}$$

We emphasize that only the approximation to obtain these results is the $\Lambda \to \infty$ limit. Therefore, these results are valid when $\Lambda \mp \mu \gg T$.

B.2 Coefficients of the QCD-CP soft mode

As in the previous section, the explicit form of the coefficients in the LE and TDGL approximations for the QCD-CP soft modes are given here. The definitions of these coefficients are given by Eqs (5.46) and (5.48).

We denote the integrals that $\mathrm{Re}Q_S^R(\boldsymbol{k},\omega)$ possesses as

$$\int_{S\text{-time}} \frac{d\omega'}{\omega'} = \left[\int_{+\lambda(|\boldsymbol{k}|,0)}^{+\bar{\Lambda}} + \int_{-\bar{\Lambda}}^{-\lambda(|\boldsymbol{k}|,0)}\right]\frac{d\omega'}{\omega'}, \tag{B.18}$$

$$\int_{S\text{-space}} \frac{d\omega'}{\omega'} = \int_{-\lambda(|\boldsymbol{k}|,\bar{\Lambda})}^{+\lambda(|\boldsymbol{k}|,\bar{\Lambda})} \frac{d\omega'}{\omega'}, \tag{B.19}$$

and the derivatives of $F_S(x,y)$ given by Eq. (5.25) is

$$F_S'(x,y) = \frac{\partial F_S(x,y)}{\partial x} = \frac{1}{4T}\sum_{s,t=\pm} s\tanh\frac{x+sy-2t\mu}{4T}. \tag{B.20}$$

B.2.1 LE approximation

From Eq. (5.46), we obtain

$$\begin{aligned} A_S(\boldsymbol{k}) &= \frac{1}{G_S} + \mathrm{Re}Q_S^R(\boldsymbol{k},0) \\ &= \frac{1}{G_S} - \frac{N_f N_c T}{4\pi^2}\left\{\int_{S\text{-time}}\frac{d\omega'}{\omega'}\frac{\omega'^2-\boldsymbol{k}^2-4M^2}{|\boldsymbol{k}|}F_S\big(\omega',\lambda(|\boldsymbol{k}|,\omega')\big)\right. \\ &\quad \left. + \int_{S\text{-space}}\frac{d\omega'}{\omega'}\frac{\omega'^2-\boldsymbol{k}^2-4M^2}{|\boldsymbol{k}|}\Big(F_S\big(\omega',\lambda(|\boldsymbol{k}|,\omega')\big) - F_S\big(\omega',\bar{\Lambda}\big)\Big)\right\}. \end{aligned} \tag{B.21}$$

One can find $\mathrm{Re}Q_S^R(\boldsymbol{k},\omega)$ and $\mathrm{Im}Q_S^R(\boldsymbol{k},\omega)$ are even and odd functions for ω at $\omega = 0$, and then $\partial\mathrm{Re}Q_S^R(\boldsymbol{k},\omega)/\partial\omega|_{\omega=0} = 0$. It is also noted that the strength of the QCD-CP soft mode exists in $|\omega| < \lambda(|\boldsymbol{k}|,\bar{\Lambda})$. Therefore,

$$\begin{aligned} C_S(\boldsymbol{k}) &= i\,\mathrm{Im}C_S(\boldsymbol{k}) \\ &= i\,\frac{\partial \mathrm{Im}Q_S^R(\boldsymbol{k},\omega)}{\partial\omega}\bigg|_{\omega=0} \\ &= i\,\frac{N_f N_c T}{4\pi}\frac{\boldsymbol{k}^2+4M^2}{|\boldsymbol{k}|}\left[F_S'\big(0,\lambda(|\boldsymbol{k}|,0)\big) - F_S'\big(0,\bar{\Lambda}\big)\right] \quad \text{for} \quad |\omega| < \lambda(|\boldsymbol{k}|,\bar{\Lambda}). \end{aligned} \tag{B.22}$$

As found in Eq. (B.22), $C_S(\boldsymbol{k})$ behaves $1/|\boldsymbol{k}|$ at small $|\boldsymbol{k}|$.

B.2.2 TDGL approximation

From Eq. (B.21),

$$\begin{aligned} a_S &= A_S(\mathbf{0}) \\ &= \frac{1}{G_S} - \frac{N_f N_c T}{4\pi^2}\int_{2M}^{\bar{\Lambda}} d\omega' \sqrt{\frac{\omega'^2 - 4M^2}{\omega'^2}} \\ &\qquad \times \sum_{s=\pm}\left[\frac{\omega'^2 - 4M^2}{\omega'^2}\tanh\frac{\omega' - 2s\mu}{4T} + \frac{M^2}{T}\cosh^{-2}\frac{\omega' - 2s\mu}{4T}\right]. \end{aligned} \tag{B.23}$$

Using Eq. (B.22),

$$\begin{aligned} c_S &= i\,\mathrm{Im}c_S = \left. i\,\mathrm{Im}C_S(\boldsymbol{q})|\boldsymbol{q}|\right|_{|\boldsymbol{q}|=0} \\ &= i\,\frac{N_f N_c T}{\pi} M^2\left[F_S'(0,2M) - F_S'(0,\bar{\Lambda})\right] \quad \text{for} \quad |\omega| < \lambda(|\boldsymbol{k}|,\bar{\Lambda}). \end{aligned} \tag{B.24}$$

On the other hand, the coefficient b_S is difficult to calculate it analytically. For that, we compute b_S numerically.

Appendix C

Derivatives of the spectral densities

In this appendix, we calculate the derivatives of the spectral densities $\rho_\gamma(\omega)$ in detail. First of all, we give the explicit forms of the derivatives within the LEE approximation, and taken into account the TDGL approximation. These forms are utilized for the numerical results in Sec. 7.2. After that, $\partial\rho_\gamma(\omega)/\partial\omega|_{\omega=0}$ and $\partial^3\rho_\gamma(\omega)/\partial^3\omega|_{\omega=0}$ are calculated analytically within the TDGL approximation, whose results leads to Sec. 7.1.

In the LE approximations, the explicit forms of the spectral densities are Eq.(7.6), and the derivatives of $\rho_\gamma(\omega)$ are then given by

$$\left.\frac{\partial\rho_\gamma(\omega)}{\partial\omega}\right|_{\omega=0} = 2\tilde{N}_\gamma \int \frac{d^3q}{(2\pi)^3}\left(\frac{\partial A_\gamma(\boldsymbol{q})}{\partial \boldsymbol{q}}\right)^2 \int \frac{d\omega'}{2\pi}\coth\frac{\omega'}{2T} \times \mathrm{Im}\Xi^R_\gamma(\boldsymbol{q},\omega')\,\frac{\partial}{\partial\omega'}\mathrm{Im}\Xi^R_\gamma(\boldsymbol{q},\omega'), \tag{C.1}$$

$$\left.\frac{\partial^3\rho_\gamma(\omega)}{\partial^3\omega}\right|_{\omega=0} = 2\tilde{N}_\gamma \int \frac{d^3q}{(2\pi)^3}\left(\frac{\partial A_\gamma(\boldsymbol{q})}{\partial \boldsymbol{q}}\right)^2 \int \frac{d\omega'}{2\pi}\coth\frac{\omega'}{2T} \times \mathrm{Im}\Xi^R_\gamma(\boldsymbol{q},\omega')\,\frac{\partial^3}{\partial^3\omega'}\mathrm{Im}\Xi^R_\gamma(\boldsymbol{q},\omega'). \tag{C.2}$$

where $\tilde{N}_D = 3e_\Delta^2$ and $\tilde{N}_S = e_u^2 + e_d^2$ given by Eq. (7.8). The imaginary part of $\Xi^R_\gamma(\boldsymbol{q},\omega')$ is written explicitly by

$$\mathrm{Im}\Xi^R_D(\boldsymbol{q},\omega') = -\frac{\mathrm{Im}C_D\omega'}{(A_D(\boldsymbol{q})+\mathrm{Re}C_D\omega')^2+(\mathrm{Im}C_D\omega')^2} \tag{C.3}$$

$$\mathrm{Im}\Xi^R_S(\boldsymbol{q},\omega') = -\frac{\mathrm{Im}C_S(\boldsymbol{q})\omega'}{A_D^2(\boldsymbol{q})+(\mathrm{Im}C_S(\boldsymbol{q})\omega')^2} \tag{C.4}$$

Here, for convenience, we introduce

$$g_D(\boldsymbol{q},\omega') = (A_D(\boldsymbol{q})+\mathrm{Re}C_D\omega')^2+(\mathrm{Im}C_D\omega')^2 \tag{C.5}$$

$$g_S(\boldsymbol{q},\omega') = A_S^2(\boldsymbol{q})+(\mathrm{Im}C_S(\boldsymbol{q})\omega')^2 \tag{C.6}$$

Then, $\mathrm{Im}\Xi^R_\gamma(\boldsymbol{q},\omega')$ and their derivatives are

$$\mathrm{Im}\Xi^R_D(\boldsymbol{q},\omega') = -\frac{\mathrm{Im}C_D\omega'}{g_D(\boldsymbol{q},\omega')} \tag{C.7}$$

$$\frac{\partial}{\partial\omega'}\mathrm{Im}\Xi^R_D(\boldsymbol{q},\omega') = -\frac{\mathrm{Im}C_D}{g_D^2(\boldsymbol{q},\omega')}\left(A_D^2(\boldsymbol{q})-|C_D|^2\omega'^2\right) \tag{C.8}$$

$$\frac{\partial^3}{\partial^3\omega'}\mathrm{Im}\Xi^R_D(\boldsymbol{q},\omega') = \frac{6\mathrm{Im}C_D}{g_D^2(\boldsymbol{q},\omega')}\left[|C_D|^2-\frac{4\alpha(\boldsymbol{q},\omega')\left(\alpha(\boldsymbol{q},\omega')+|C_D|^2\omega'\right)}{g_D(\boldsymbol{q},\omega')}+\frac{8\alpha^3(\boldsymbol{q},\omega')}{g_D^2(\boldsymbol{q},\omega')}\right] \tag{C.9}$$

where $\alpha(\boldsymbol{q},\omega') = \tilde{A}_D(\boldsymbol{q})\mathrm{Re}c_D + |c_D|^2\omega'$, and $\mathrm{Im}\Xi^R_\gamma(\boldsymbol{q},\omega')$ and their derivatives are

$$\mathrm{Im}\Xi^R_S(\boldsymbol{q},\omega') = -\frac{\mathrm{Im}C_S(\boldsymbol{q})\omega'}{g_S(\boldsymbol{q},\omega')} \tag{C.10}$$

$$\frac{\partial}{\partial\omega'}\mathrm{Im}\Xi^R_S(\boldsymbol{q},\omega') = -\frac{\mathrm{Im}C_S(\boldsymbol{q})}{g_S(\boldsymbol{q},\omega')}\left[1 - 2\,\frac{(\mathrm{Im}C_S(\boldsymbol{q})\omega')^2}{g_S(\boldsymbol{q},\omega')}\right] \tag{C.11}$$

$$\frac{\partial^3}{\partial^3\omega'}\mathrm{Im}\Xi^R_S(\boldsymbol{q},\omega') = \frac{6(\mathrm{Im}C_S(\boldsymbol{q}))^3}{g^2_S(\boldsymbol{q},\omega')}\left[1 - 8\,\frac{A^2_S(\boldsymbol{q})(\mathrm{Im}C_S(\boldsymbol{q})\omega')^2}{g^2_S(\boldsymbol{q},\omega')}\right] \tag{C.12}$$

In Eqs. (C.1) and (C.2), $\partial A_\gamma(\boldsymbol{q})/\partial\boldsymbol{q}$ corresponds to the vertex of AL term, and the explicit form is found

$$\begin{aligned}
\frac{\partial Q^R_D(\boldsymbol{q})}{\partial\boldsymbol{q}} = -\frac{N_f(N_c-1)T}{4\pi^2}\Bigg\{ &\left[\int_{\bar{k}(|\boldsymbol{q}|,0)-2\mu}^{+\bar{\Lambda}-2\mu}\frac{d\omega''}{\omega''} + \int_{-\bar{\Lambda}-2\mu}^{-\bar{k}(|\boldsymbol{q}|,0)-2\mu}\frac{d\omega''}{\omega''}\right] \\
&\times\Bigg(-\frac{(\omega''+2\mu)^2+\boldsymbol{q}^2}{\boldsymbol{q}^2}F_D\big(\bar{k}(|\boldsymbol{q}|,\omega''+2\mu),\omega''\big) \\
&\quad+\frac{(\omega''+2\mu)^2-\boldsymbol{q}^2}{\boldsymbol{q}^2}F'_D\big(\bar{k}(|\boldsymbol{q}|,\omega''+2\mu),\omega''\big)\,\bar{k}'(|\boldsymbol{q}|,\omega''+2\mu)\Bigg) \\
+\int_{-\bar{k}(|\boldsymbol{q}|,\bar{\Lambda})}^{\bar{k}(|\boldsymbol{q}|,\bar{\Lambda})}\frac{d\omega''}{\omega''}\Bigg(&-\frac{(\omega''+2\mu)^2+\boldsymbol{q}^2}{\boldsymbol{q}^2}F_D\big(\bar{k}(|\boldsymbol{q}|,\omega''+2\mu),\omega''\big) \\
&\quad+\frac{(\omega''+2\mu)^2-\boldsymbol{q}^2}{\boldsymbol{q}^2}F'_D\big(\bar{k}(|\boldsymbol{q}|,\omega''+2\mu),\omega''\big)\,\bar{k}'(|\boldsymbol{q}|,\omega''+2\mu) \\
&\quad-\frac{(\omega''+2\mu)^2+\boldsymbol{q}^2}{\boldsymbol{q}^2}F_D\big(\bar{\Lambda},\omega''+2\mu\big)\Bigg)\Bigg\}
\end{aligned} \tag{C.13}$$

$$\begin{aligned}
\frac{\partial Q^R_S(\boldsymbol{q})}{\partial\boldsymbol{q}} = -\frac{N_fN_cT}{4\pi^2}\Bigg\{ 2\int_{\bar{k}(|\boldsymbol{q}|,0)}^{\bar{\Lambda}}\frac{d\omega''}{\omega''}\Bigg(&-\frac{\omega''^2+\boldsymbol{q}^2-4M^2}{\boldsymbol{q}^2}F_S\big(\bar{k}(|\boldsymbol{q}|,\omega''),\omega''\big) \\
&\quad+\frac{\omega''^2-\boldsymbol{q}^2-4M^2}{\boldsymbol{q}^2}F'_S\big(\bar{k}(|\boldsymbol{q}|,\omega''),\omega''\big)\,\bar{k}'(|\boldsymbol{q}|,\omega'')\Bigg) \\
+\int_{-\bar{k}(|\boldsymbol{q}|,\bar{\Lambda})}^{\bar{k}(|\boldsymbol{q}|,\bar{\Lambda})}\frac{d\omega''}{\omega''}\Bigg(&-\frac{\omega''^2+\boldsymbol{q}^2-4M^2}{\boldsymbol{q}^2}F_S\big(\bar{k}(|\boldsymbol{q}|,\omega''),\omega''\big) \\
&\quad+\frac{\omega''^2-\boldsymbol{q}^2-4M^2}{\boldsymbol{q}^2}F'_S\big(\bar{k}(|\boldsymbol{q}|,\omega''),\omega''\big)\,\bar{k}'(|\boldsymbol{q}|,\omega'') \\
&\quad+\frac{\omega''^2+\boldsymbol{q}^2-4M^2}{\boldsymbol{q}^2}F_S\big(\bar{\Lambda},\omega''\big)\Bigg)\Bigg\}
\end{aligned} \tag{C.14}$$

Calculating Eqs. (C.1) and (C.2) with Eqs. (C.7)–(C.14) and substituting them to Eqs. (**??**)–(**??**), σ and τ_σ are obtained within the LE approximation.

In using the TDGL approximation, the following replacements in the above calculations are all that need to be done

$$A_D(\boldsymbol{q}) \to \tilde{A}_D(\boldsymbol{q}) = a_D + b_D\boldsymbol{q}^2, \qquad C_D \to c_D, \tag{C.15}$$

$$A_S(\boldsymbol{q}) \to \tilde{A}_S(\boldsymbol{q}) = a_S + b_S\boldsymbol{q}^2, \qquad \mathrm{Im}C_S(\boldsymbol{q}) \to -|c_S|/|\boldsymbol{q}|, \tag{C.16}$$

Through these replacements, we can obtain the derivatives of Eqs. (7.7), where $\partial\tilde{A}_\gamma(\boldsymbol{q})/\partial\boldsymbol{q}$ becomes $2b_\gamma\boldsymbol{q}$. We remind that c_S is purely imaginary and note that the signs of $\mathrm{Re}c_D$, $\mathrm{Im}c_D$, and $\mathrm{Im}c_S$ are all minus. In the following sections, we calculate the derivatives analytically using the TDGL approximation with some simplifications to evaluate the behavior of $\partial\rho_\gamma(\omega)/\partial\omega$ and $\partial^3\rho_\gamma(\omega)/\partial^3\omega$ in the vicinity of the respective critical points.

C.1 Exponents as for the 2SC-PT

Next, focusing on the vicinity of the 2SC-PT, we calculate the derivatives analytically. Since the strength of $\mathrm{Im}\Xi_D^R(\boldsymbol{q},\omega')$ is concentrating on the origin of the ω'-$|\boldsymbol{q}|$ plane near the critical points, the following simplification can be carried out

$$\coth\frac{\omega'}{2T}\simeq\frac{2T}{\omega'}. \tag{C.17}$$

Moreover, we can simplify the integration of Eqs. (C.1) and (C.2) for $\gamma=D$ as follows

$$\int d^3q\int d\omega'\simeq\int_{-\infty}^{+\infty}d^3q\int_{-\infty}^{+\infty}d\omega', \tag{C.18}$$

whose integration range is originally determined by the limitation of $\mathrm{Im}Q_D^R(\boldsymbol{q},\omega')$. These manipulations are valid as long we consider the vicinity of the critical points since the significant strength of the soft mode concentrates on the origin as described above and the integrand of $\partial\rho_D(\omega')/\partial\omega$ and $\partial^3\rho_D(\omega')/\partial^3\omega$ converges in the limit $|\boldsymbol{q}|\to\infty$ and/or $|\omega'|\to\infty$.

Through the simplifications (C.17) and (C.18), $\partial\rho_D(\omega')/\partial\omega$ and $\partial^3\rho_D(\omega')/\partial^3\omega$ can be evaluated analytically within the TDGL approximation, i.e. the use of Eqs. (C.7)–(C.9) with the replacements Eqs. (C.15), as follows

$$\begin{aligned}
\left.\frac{\partial\rho_D(\omega)}{\partial\omega}\right|_{\omega=0}&=2\tilde{N}_D\int_{-\infty}^{+\infty}\frac{d^3q}{(2\pi)^3}(2b_D\boldsymbol{q})^2\int_{-\infty}^{+\infty}\frac{d\omega'}{2\pi}\frac{2T}{\omega'}\,\mathrm{Im}\Xi_D^R(\boldsymbol{q},\omega')\,\frac{\partial}{\partial\omega'}\mathrm{Im}\Xi_D^R(\boldsymbol{q},\omega')\\
&=-\frac{\tilde{N}_DT}{\pi^2}\frac{|c_D|^2}{\mathrm{Im}c_D}b_D^2\int_0^\infty\frac{q^4dq}{A_D^3(\boldsymbol{q})}\\
&=-\frac{9e_\Delta^2T}{16\pi}\frac{|c_D|^2}{\mathrm{Im}c_D}\frac{1}{a_D^{1/2}b_D^{1/2}},
\end{aligned} \tag{C.19}$$

$$\begin{aligned}
\left.\frac{\partial^3\rho_D(\omega)}{\partial^3\omega}\right|_{\omega=0}&=2\tilde{N}_D\int_{-\infty}^{+\infty}\frac{d^3q}{(2\pi)^3}(2b_D\boldsymbol{q})^2\int_{-\infty}^{+\infty}\frac{d\omega'}{2\pi}\frac{2T}{\omega'}\,\mathrm{Im}\Xi_D^R(\boldsymbol{q},\omega')\,\frac{\partial^3}{\partial^3\omega'}\mathrm{Im}\Xi_D^R(\boldsymbol{q},\omega')\\
&=\frac{3\tilde{N}_DT}{2\pi^2}\frac{|c_D|^6}{(\mathrm{Im}c_D)^3}b_D^2\int_0^\infty\frac{q^4dq}{A_D^5(\boldsymbol{q})}\\
&=\frac{27e_\Delta^2T}{512\pi}\frac{|c_D|^6}{(\mathrm{Im}c_D)^3}\frac{1}{a_D^{5/2}b_D^{1/2}}.
\end{aligned} \tag{C.20}$$

C.2 Case of the QCD-CP

As the previous section, $\partial\rho_S(\omega')/\partial\omega$ and $\partial^3\rho_S(\omega')/\partial^3\omega$ are calculated analytically near the QCD-CP within the TDGL approximation. The simplification (C.17) can also be taken into account because $\mathrm{Im}\Xi_S^R(\boldsymbol{q},\omega')$ has the significant strength around the origin of ω'-$|\boldsymbol{q}|$ plane as well. Next, let us consider the integration range in this case. One would remember that $\mathrm{Im}\Xi_S^R(\boldsymbol{q},\omega')$ is limited in the region $|\omega'|<\bar{k}(|\boldsymbol{q}|,\omega)$ that is described in Chap. 5. Since this region becomes $|\omega'|<|\boldsymbol{q}|$ in the limit $\Lambda\to\infty$, the integration range of Eqs. (C.1) and (C.2) for $\gamma=S$ can be simplified as

$$\int d^3q\int d\omega'=\int_{-\infty}^{+\infty}d^3q\int_{-q}^{+q}d\omega', \tag{C.21}$$

Since the integrands of $\partial\rho_S(\omega')/\partial\omega$ and $\partial^3\rho_S(\omega')/\partial^3\omega$ converge in the limit $|\boldsymbol{q}|\to\infty$, these manipulations are valid near the QCD-CP as in the 2SC-PT case.

Under the simplifications (C.17) and (C.21), the derivatives can be computed by using Eqs. (C.10)–(C.12) with the replacements (C.16) as

$$\begin{aligned}
\left.\frac{\partial\rho_S(\omega)}{\partial\omega}\right|_{\omega=0} &= 2\tilde{N}_S\int_{-\infty}^{+\infty}\frac{d^3q}{(2\pi)^3}(2b_S\boldsymbol{q})^2\int_{-q}^{+q}d\omega'\,\frac{2T}{\omega'}\,\mathrm{Im}\Xi_S^R(\boldsymbol{q},\omega')\,\frac{\partial}{\partial\omega'}\mathrm{Im}\Xi_S^R(\boldsymbol{q},\omega') \\
&= \frac{2\tilde{N}_S T}{\pi^3}b_S^2\int_0^\infty q^3dq\left[\frac{|c_S|}{\tilde{A}_S^3(\boldsymbol{q})}\tan^{-1}\frac{|c_S|}{\tilde{A}_S(\boldsymbol{q})}+\frac{|c_S|^2}{\tilde{A}_S^2(\boldsymbol{q})}\frac{3\tilde{A}_S^3(\boldsymbol{q})+|c_S|^2}{(\tilde{A}_S^2(\boldsymbol{q})+|c_S|^2)^2}\right], \\
&= -\frac{(e_u^2+e_d^2)T}{2\pi^3}\left[\frac{a_S^2-|c_S|^2}{a_S|c_S|}\tan^{-1}\frac{|c_S|}{a_S}-1\right] \qquad \text{(C.22)} \\
\left.\frac{\partial^3\rho_S(\omega)}{\partial^3\omega}\right|_{\omega=0} &= 2\tilde{N}_S\int_{-\infty}^{+\infty}\frac{d^3q}{(2\pi)^3}(2b_S\boldsymbol{q})^2\int_{-q}^{+q}d\omega'\,\frac{2T}{\omega'}\,\mathrm{Im}\Xi_S^R(\boldsymbol{q},\omega')\,\frac{\partial^3}{\partial^3\omega'}\mathrm{Im}\Xi_S^R(\boldsymbol{q},\omega') \\
&= -\frac{48\tilde{N}_S T}{\pi^3}b_S^2|c_S|^4\int_0^\infty qdq\left[\frac{1}{16\tilde{A}_S^5(\boldsymbol{q})|c_S|}\tan^{-1}\frac{|c_S|}{\tilde{A}_S(\boldsymbol{q})}\right. \\
&\qquad\left.+\frac{45\tilde{A}_S^6(\boldsymbol{q})+5\tilde{A}_S^4(\boldsymbol{q})|c_S|^2+11\tilde{A}_S^2(\boldsymbol{q})|c_S|^4+3|c_S|^6}{48\tilde{A}_S^4(\boldsymbol{q})(\tilde{A}_S^2(\boldsymbol{q})+|c_S|^2)^4}\right] \\
&= -\frac{(e_u^2+e_d^2)T}{8\pi^3}b_S|c_S|^2\left[\frac{3|c_S|}{a_S^4}\tan^{-1}\frac{|c_S|}{a_S}-\frac{1}{a_S^3}+\frac{3}{a_S|c_S|^2}-\frac{3}{|c_S|^3}\tan^{-1}\frac{a_S}{|c_S|}\right. \\
&\qquad\left.-\frac{4|c_S|^2}{a_S^3}\frac{9a_S^4+2a_S^2|c_S|^2+|c_S|^4}{(a_S^2+|c_S|^2)^3}-\frac{3\pi}{2|c_S|^3}\right]. \qquad \text{(C.23)}
\end{aligned}$$

Extracting the leading terms in the limit $(T,\mu)\to(T_{CP},\mu_{CP})$, i.e. $a_S\to 0$, we obtain the results of Eqs. (7.18) and (7.19).

Appendix D

Dilepton yields along the isentropic lines

In Chap. 8, we calculated the production rate of dileptons $d^4\Gamma/d^4k(\boldsymbol{k},\omega)$ per unit volume and time and confirmed the enhancements due to the 2SC-PT and QCD-PT soft modes near the respective phase transitions. In order to clarify that these enhancements can serve as signals of the 2SC-PT and QCD-PT in HIC experiments, we have to investigate the dilepton production yields integrated over the entire space-time evolution in HIC. Then, as its first step, we estimate the excess of the production yields due to the soft modes over the contributions of the free quark gases with the isentropic expansion trajectory in this section. This study is based on Res. [103].

To compute the isentropic line, using the thermodynamic potential in the MFA $\omega_{\rm MFA}$ (4.31), we calculate the entropy density $s = s(T,\mu) = -\partial\omega_{\rm MFA}/\partial T$ and baryon number density $n_B = n_B(T,\mu) = -(\partial\omega_{\rm MFA}/\partial\mu)/3$ of the system. The time evolution due to isentropic lines are gained by assuming the Bjorken expansion of the perfect fluid, where the longitudinal component of the fluid velocity is the same as the free streaming of particles from the origin of the spatial coordinate: $v_z = z/t$ [109] with the time t and the coordinate in the longitudinal direction z. Under this ansatz, the entropy s and baryon density n_B evolves as follows

$$s(T(\tau),\mu(\tau)) = s(T(\tau_0),\mu(\tau_0))\frac{\tau_0}{\tau}, \tag{D.1}$$

$$n_B(T(\tau),\mu(\tau)) = n_B(T(\tau_0),\mu(\tau_0))\frac{\tau_0}{\tau}, \tag{D.2}$$

where $\tau = \sqrt{t^2 - z^2}$ is the proper time and τ_0 is the initial proper time. Then, we obtain the isentropic time evolution, i.e. lines of constant entropy per baryon $S/A = s(T(\tau),\mu(\tau))/n_B(T(\tau),\mu(\tau))$.

We show the isentropic trajectories in the phase diagram with the diquark coupling $G_D = 0.70G_S$ in Fig. D.1. In this figure, the thin solid lines represent the isentropic trajectories at different values of $S/A = 10, 9, \ldots, 2$. Their time evolutions are considered up to the crossover transition or the first-order phase transition line. For that, the contributions from the hadronic phase are neglected. When the values of S/A are small, the trajectories can pass through the 2SC phase until they reach the first-order phase transition line. According to the estimate in Ref. [110], the value range $S/A < 4$ corresponds to the collision energy of $\sqrt{s_{NN}} \leq 3.0$ GeV. However, owing to our simplifications and the model dependence of the QCD-CP location, we would not like to assert that we expect quark matter or the CSC phase to appear at such a low beam energy in this study.

For the time evolution, four initial conditions (IC) is considered in the present calculation, which are represented by the four types of markers in Fig. D.1. IC-1 is defined by the horizontal line at $T = 500$ MeV and the vertical line at $\mu = 600$ MeV, where let the condition be denoted by $\{T,\mu\} = \{500, 600\}$. In the same manner, IC-2, IC-3, and IC-4 are $\{T,\mu\} = \{400, 550\}$, $\{300, 500\}$ and $\{200, 450\}$, respectively. The initial conditions for low- to intermediate- collision energies may be calculated, e.g. by the Rankine-Hugoniot-Taub adiabat [110]. Instead of using specific models for initial conditions in this study, we shall show that the qualitative behavior of dilepton yields in the ultra-low energy regions is not dependent on the details of the initial conditions.

Figure D.2 shows the time (proper time τ) evolution of temperature T and chemical potnetial $\mu = \mu_B/3$ along the isentropic trajectory for different entropy per baryon number ratios $S/A = 2, 4, 6, 8$. For larger S/A values, T and $\mu = 3\mu_B$ decrease rapidly, leading to a shorter lifetime of

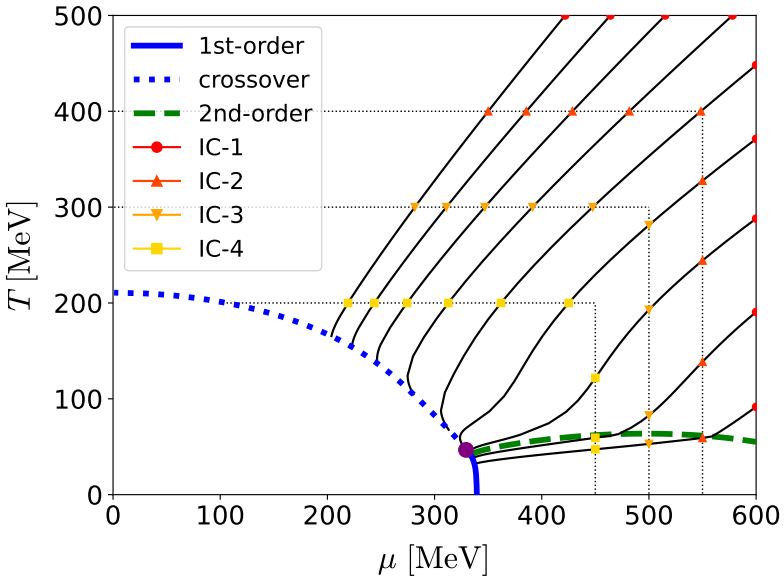

FIGURE D.1: Isentropic lines in the phase diagram calculated by the thermodynamic potential (4.31) in the MFA. The solid and dotted lines are the first-order and crossover phase transition of the chiral symmetry breaking, respectively. The circle marker is the QCD-CP, and the dashed line is the second-order phase transition line of the 2SC for the diquark coupling $G_D = 0.7G_S$. The thin solid lines are the isentropic lines with $S/A = 10, 9, 8, 7, 6, 5, 4, 3, 2$ and the small circles, triangles, inverse triangles, and squares represent the four different initial conditions for each isentropic trajectory.

the system. On the other hand, for smaller S/A values, specifically at lower T and higher μ, the time evolution slows down as the system approaches the phase boundary or critical point, resulting in a longer lifetime of the system. One finds that the lifetime at $S/A = 2$ is approximately twice the lifetime at $S/A = 8$. However, as will be shown later, the extent of enhancement in dilepton production yields depends on the proximity of the system's path to the 2SC-PT or the QCD-CP rather than on the lifetime of the system.

Here, we mention several remarks on the time evolution of the system. In order to provide a realistic description of the dynamics near the QCD-CP, it is crucial to consider the generation of entropy resulting from non-equilibrium fluctuations, which can change the evolution in the phase diagram as discussed in [111, 112]. Additionally, the transverse expansion should be included since the system may cool down faster than the 1+1 Bjorken longitudinal expansion, which reduces the total dilepton yields. These considerations into our calculation are interesting future works.

In this study, the dilepton yields are calculated by integrating over the isentropic trajectories for different entropy per baryon number S/A. As shown in the previous sections, the behavior of the energy spectrum is qualitatively similar to the one of the invariant spectrum. Therefore, we consider the energy spectrum with zero momentum for the dilepton production rate and calculate

$$\frac{dR}{d\Gamma} = \frac{1}{\tau_0^2}\frac{d^6R}{dxdyd\eta d^3k} = \int_{C(S/A)} \frac{\tau d\tau}{\tau_0^2} \int d\omega \frac{d^8R(\mathbf{0},\omega)}{d^4x d\omega d^3k}, \tag{D.3}$$

where the integral path C is taken along the constant S/A.

We show the numerical results of production yields as a function of S/A for the value of diquark coupling $G_D = 0.7G_S$ in Fig. D.3. In the top panel of the figure, we use the IC-1 as an initial condition. Instead of employing specific models for the initial conditions, the dilepton yields are divided by the factor τ_0^2 since we are only interested in the enhancement from the soft mode relative to the contributions from the free quark gas. We consider three integration ranges for ω-integral (left: $50\text{MeV} < \omega < 100\text{MeV}$, middle: $100\text{MeV} < \omega < 200\text{MeV}$, and right: $200\text{MeV} < \omega < 300\text{MeV}$).

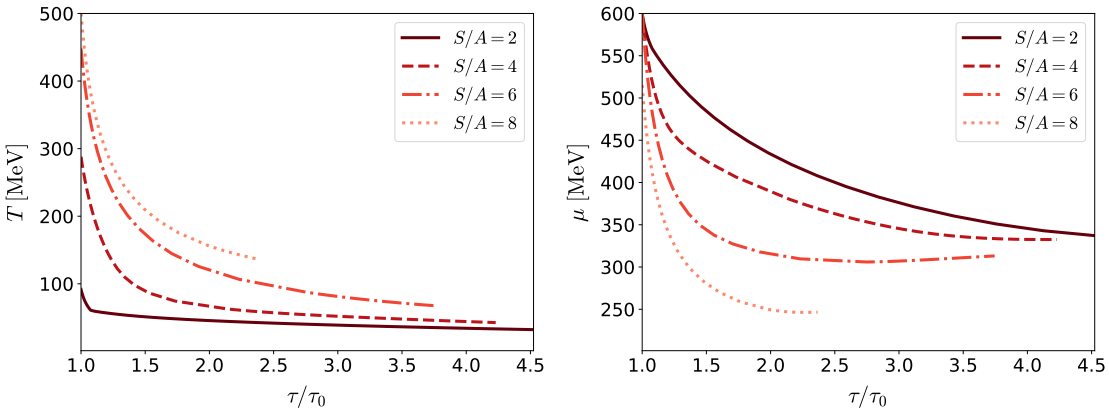

FIGURE D.2: Time evolution of the temperature T (left panel) and the quark chemical potential μ (right panel) along the isentropic trajectories for the initial condition 1. The solid, dashed, dash-dotted, and dotted lines correspond to $S/A = 2$, 4, 6, and 8, respectively.

The solid red and dashed blue lines represent the contributions of 2SC-PT and the contributions of QCD-CP, while the dotted green lines correspond to the yields from the free quark gases. The sum of them gives the total dilepton production in this study. It is found that the results from the soft modes in the low-energy region (50MeV $< \omega <$ 100MeV) exceed the ones of the free quark gases in a wide range of S/A values. One finds an interesting structure in these spectra: a local maximum and minimum at $S/A \approx 5.5$ and at $S/A \approx 4.0$, respectively. These bumps appear since the trajectory approaches close to the QCD-CP at $S/A \approx 5.5$ or largely aligns with the 2SC-PT at $S/A \approx 4.0$, as illustrated in Fig. D.1. In the energy range 100MeV $< \omega <$ 200MeV, the enhancement of the dilepton at $S/A < 4$ for both QCD-CP and 2SC is also found. The middle row panels shows the ratio of the dilepton production from the 2SC-PT and QCD-CP to the free quark gas with the IC-1. Dilepton enhancements over the free quark gas are seen in the region of $\omega < 300$ MeV and $S/A < 3-4$. The enhancement in this range is greatly significant with several orders of magnitude.

In the bottom panels of Fig.D.3, the dilepton yields for 50 MeV $< \omega <$ 100 MeV with IC-1,2,3,4 are shown to check the dependence of the dilepton yields on different initial conditions. One sees that production yields from the 2SC-PT, QCD-PT, and free quark gas are not affected largely by the initial conditions in a wide range of the S/A values. A relatively small change of the free quark contribution is due to an extended lifetime, which is not relevant when compared to a several-order-of-magnitude enhancement. As shown in the previous sections, since the T- and μ-dependence in the invariant mass spectrum is qualitatively similar to the energy/momentum spectrum, we expect that the nontrivial structure in the S/A dependence of the dilepton production from the soft modes of the 2SC-PT and QCD-CP can still be seen in the invariant mass spectra.

Since the phase transition to the 2SC phase are sensitive to diquark coupling as shown in Fig. 4.1, it is interesting to investigate the diquark coupling G_D dependence, which is shown in Fig .D.4. In this figure, the QCD-CP effect appears as a local maximum at $S/A \simeq 5.5$. The local minima are due to the soft mode of 2SC-PT. One can finds that the dilepton yield and the position of the local minima are sensitive to G_D. This results might suggest that heavy-ion collision experiments can provide information on diquark coupling. The sharp increase in the dilepton yield due to the 2SC-PT contribution at lower S/A is due to the neglect of the finite energy gap effect in the calculation of the retarded photon self-energy. This sharp increase is more pronounced when the trajectories penetrate into the 2SC phase. Incorporating the effect of the finite energy gap is expected to suppress this increase. Furthermore, even if the effect of the finite energy gap is taken into account for the self-energy, the results for QCD-CP and free quark gas are not expected to change much as described in the end of Sec. 5.2.

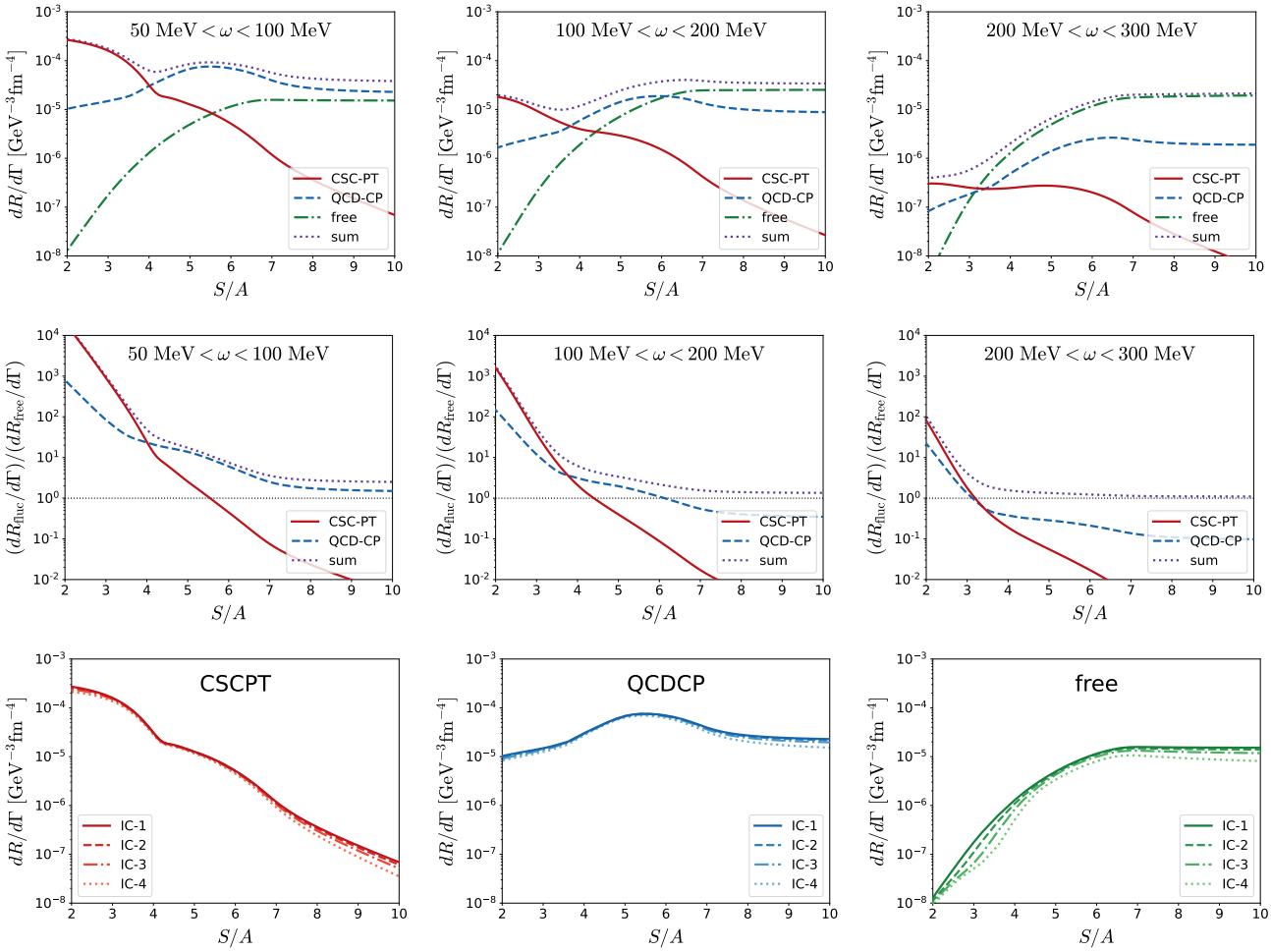

FIGURE D.3: Dilepton yields integrated over an isentropic trajectory for the initial condition 1 as a function of the entropy to baryon number (S/A) (top panels) are shown for different integral regions of the dilepton energy: The left panel shows the results for 50 MeV $< \omega <$ 100 MeV, while mid panel is for 100 MeV $< \omega <$ 200 MeV, and right panel is for 200 MeV $< \omega <$ 300 MeV. In the mid panels, the ratio of the dilepton yields (mid panels) are plotted. The integration ranges of the mid-three panels are the same as those for the top panels. The initial condition dependence of the dilepton yields for 50 MeV $< \omega <$ 100 MeVare shown in the bottom panels. The value of diquark coupling $G_D = 0.7G_S$ is used for all calculations.

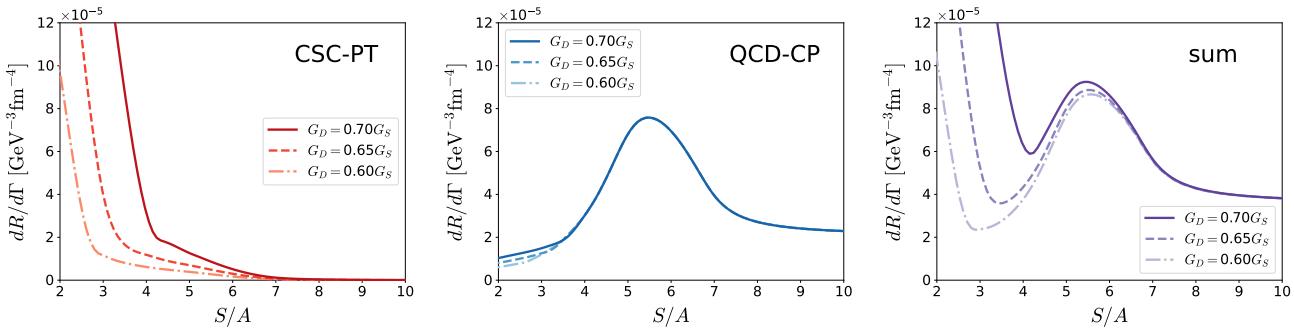

FIGURE D.4: Entropy per baryon ratio dependence of the dilepton yields integrated over an isentropic trajectory for the initial condition 1 are shown for different values of the diquark coupling G_D. The integration range of the dilepton energy is taken as 50 MeV $< \omega <$ 100 MeV.

Bibliography

[1] Kenji Fukushima and Tetsuo Hatsuda. The phase diagram of dense QCD. Rept. Prog. Phys., 74:014001, 2011.

[2] Kenji Fukushima and Chihiro Sasaki. The phase diagram of nuclear and quark matter at high baryon density. Prog. Part. Nucl. Phys., 72:99–154, 2013.

[3] David J. Gross and Frank Wilczek. Ultraviolet Behavior of Nonabelian Gauge Theories. Phys. Rev. Lett., 30:1343–1346, 1973.

[4] H. David Politzer. Reliable Perturbative Results for Strong Interactions? Phys. Rev. Lett., 30:1346–1349, 1973.

[5] J. S. Poucher et al. High-Energy Single-Arm Inelastic e - p and e - d Scattering at 6-Degrees and 10-Degrees. Phys. Rev. Lett., 32:118, 1974.

[6] Kenneth G. Wilson. Confinement of Quarks. Phys. Rev. D, 10:2445–2459, 1974.

[7] Yoichiro Nambu and G. Jona-Lasinio. Dynamical Model of Elementary Particles Based on an Analogy with Superconductivity. 1. Phys. Rev., 122:345–358, 1961.

[8] Yoichiro Nambu and G. Jona-Lasinio. Dynamical model of elementary particles based on an analogy with superconductivity. II. Phys. Rev., 124:246–254, 1961.

[9] John C. Collins and M. J. Perry. Superdense Matter: Neutrons Or Asymptotically Free Quarks? Phys. Rev. Lett., 34:1353, 1975.

[10] N. Cabibbo and G. Parisi. Exponential Hadronic Spectrum and Quark Liberation. Phys. Lett. B, 59:67–69, 1975.

[11] Szabocls Borsanyi, Zoltan Fodor, Christian Hoelbling, Sandor D. Katz, Stefan Krieg, and Kalman K. Szabo. Full result for the QCD equation of state with 2+1 flavors. Phys. Lett. B, 730:99–104, 2014.

[12] A. Bazavov et al. Equation of state in (2+1)-flavor QCD. Phys. Rev. D, 90:094503, 2014.

[13] M. Asakawa and K. Yazaki. Chiral Restoration at Finite Density and Temperature. Nucl. Phys. A, 504:668–684, 1989.

[14] A. Barducci, R. Casalbuoni, S. De Curtis, Raoul Gatto, and Giulio Pettini. Chiral Phase Transitions in QCD for Finite Temperature and Density. Phys. Rev. D, 41:1610, 1990.

[15] A. Barducci, R. Casalbuoni, Giulio Pettini, and Raoul Gatto. Chiral phases of QCD at finite density and temperature. Phys. Rev. D, 49:426–436, 1994.

[16] Juergen Berges and Krishna Rajagopal. Color superconductivity and chiral symmetry restoration at nonzero baryon density and temperature. Nucl. Phys. B, 538:215–232, 1999.

[17] O. Scavenius, A. Mocsy, I. N. Mishustin, and D. H. Rischke. Chiral phase transition within effective models with constituent quarks. Phys. Rev. C, 64:045202, 2001.

[18] Uwe C. Täuber. Critical Dynamics: A Field Theory Approach to Equilibrium and Non-Equilibrium Scaling Behavior. Cambridge University Press, 2014.

[19] Mikhail A. Stephanov. QCD Phase Diagram and the Critical Point. Prog. Theor. Phys. Suppl., 153:139–156, 2004.

[20] H. Fujii. Scalar density fluctuation at critical end point in NJL model. Phys. Rev. D, 67:094018, 2003.

[21] H. Fujii and M. Ohtani. Sigma and hydrodynamic modes along the critical line. Phys. Rev. D, 70:014016, 2004.

[22] D. T. Son and M. A. Stephanov. Dynamic universality class of the QCD critical point. Phys. Rev. D, 70:056001, 2004.

[23] P. C. Hohenberg and B. I. Halperin. Theory of Dynamic Critical Phenomena. Rev. Mod. Phys., 49:435–479, 1977.

[24] Misha A. Stephanov, K. Rajagopal, and Edward V. Shuryak. Signatures of the tricritical point in QCD. Phys. Rev. Lett., 81:4816–4819, 1998.

[25] Y. Hatta and M. A. Stephanov. Proton number fluctuation as a signal of the QCD critical endpoint. Phys. Rev. Lett., 91:102003, 2003. [Erratum: Phys.Rev.Lett. 91, 129901 (2003)].

[26] Yuki Minami and Teiji Kunihiro. Dynamical Density Fluctuations around QCD Critical Point Based on Dissipative Relativistic Fluid Dynamics -Possible fate of Mach cone at the critical point-. Prog. Theor. Phys., 122:881–910, 2010.

[27] Masayuki Asakawa, Shinji Ejiri, and Masakiyo Kitazawa. Third moments of conserved charges as probes of QCD phase structure. Phys. Rev. Lett., 103:262301, 2009.

[28] Masayuki Asakawa and Masakiyo Kitazawa. Fluctuations of conserved charges in relativistic heavy ion collisions: An introduction. Prog. Part. Nucl. Phys., 90:299–342, 2016.

[29] Md Hasanujjaman, Golam Sarwar, Mahfuzur Rahaman, Abhijit Bhattacharyya, and Jan-e Alam. Dynamical spectral structure of density fluctuation near the QCD critical point. Eur. Phys. J. A, 57(10):283, 2021.

[30] Alessandro Lovato et al. Long Range Plan: Dense matter theory for heavy-ion collisions and neutron stars. 11 2022.

[31] Mark G. Alford, Andreas Schmitt, Krishna Rajagopal, and Thomas Schäfer. Color superconductivity in dense quark matter. Rev. Mod. Phys., 80:1455–1515, 2008.

[32] Thomas Schäfer and Edward V. Shuryak. Instantons in QCD. Rev. Mod. Phys., 70:323–426, 1998.

[33] R. Rapp, Thomas Schäfer, Edward V. Shuryak, and M. Velkovsky. High density QCD and instantons. Annals Phys., 280:35–99, 2000.

[34] D. Bailin and A. Love. Superfluidity and Superconductivity in Relativistic Fermion Systems. Phys. Rept., 107:325, 1984.

[35] M. Iwasaki and T. Iwado. Hartree-Bogolyubov theory of quark matter: Condensation energy in strange quark matter. Prog. Theor. Phys., 94:1073–1088, 1995.

[36] Mark G. Alford, Krishna Rajagopal, and Frank Wilczek. QCD at finite baryon density: Nucleon droplets and color superconductivity. Phys. Lett. B, 422:247–256, 1998.

[37] R. Rapp, Thomas Schäfer, Edward V. Shuryak, and M. Velkovsky. Diquark Bose condensates in high density matter and instantons. Phys. Rev. Lett., 81:53–56, 1998.

[38] D. T. Son. Superconductivity by long range color magnetic interaction in high density quark matter. Phys. Rev. D, 59:094019, 1999.

[39] Akira Ohnishi. Approaches to QCD phase diagram; effective models, strong-coupling lattice QCD, and compact stars. J. Phys. Conf. Ser., 668(1):012004, 2016.

[40] Masakiyo Kitazawa, Tomoi Koide, Teiji Kunihiro, and Yukio Nemoto. Chiral and color superconducting phase transitions with vector interaction in a simple model. Prog. Theor. Phys., 108(5):929–951, 2002. [Erratum: Prog.Theor.Phys. 110, 185–186 (2003)].

[41] Masakiyo Kitazawa, Tomoi Koide, Teiji Kunihiro, and Yukio Nemoto. Pseudogap of color superconductivity in heated quark matter. Phys. Rev. D, 70:056003, 2004.

[42] Masakiyo Kitazawa, Tomoi Koide, Teiji Kunihiro, and Yukio Nemoto. Pre-critical phenomena of two-flavor color superconductivity in heated quark matter: Diquark-pair fluctuations and non-Fermi liquid behavior. Prog. Theor. Phys., 114:117–155, 2005.

[43] WJ Skocpol and M Tinkham. Fluctuations near superconducting phase transitions. Reports on Progress in Physics, 38(9):1049, 1975.

[44] Michael Tinkham. Introduction to superconductivity. Courier Corporation, 2004.

[45] AI Larkin and AA Varlamov. Fluctuation phenomena in superconductors. Springer, 2008.

[46] Hiroaki Abuki, Tetsuo Hatsuda, and Kazunori Itakura. Structural change of Cooper pairs and momentum dependent gap in color superconductivity. Phys. Rev. D, 65:074014, 2002.

[47] D. N. Voskresensky. Fluctuations of the color superconducting order parameter in heated and dense quark matter. 6 2003.

[48] B. O. Kerbikov and M. A. Andreichikov. Electrical Conductivity of Dense Quark Matter with Fluctuations and Magnetic Field Included. Phys. Rev. D, 91(7):074010, 2015.

[49] Berndt Muller, Jurgen Schukraft, and Boleslaw Wyslouch. First Results from Pb+Pb collisions at the LHC. Ann. Rev. Nucl. Part. Sci., 62:361–386, 2012.

[50] K. Adcox et al. Formation of dense partonic matter in relativistic nucleus-nucleus collisions at RHIC: Experimental evaluation by the PHENIX collaboration. Nucl. Phys. A, 757:184–283, 2005.

[51] John Adams et al. Experimental and theoretical challenges in the search for the quark gluon plasma: The STAR Collaboration's critical assessment of the evidence from RHIC collisions. Nucl. Phys. A, 757:102–183, 2005.

[52] Tetyana Galatyuk, Paul M. Hohler, Ralf Rapp, Florian Seck, and Joachim Stroth. Thermal Dileptons from Coarse-Grained Transport as Fireball Probes at SIS Energies. Eur. Phys. J. A, 52(5):131, 2016.

[53] Frank Geurts and Ralf-Arno Tripolt. Electromagnetic probes: Theory and experiment. Prog. Part. Nucl. Phys., 128:104004, 2023.

[54] Tetsufumi Hirano and Miklos Gyulassy. Perfect fluidity of the quark gluon plasma core as seen through its dissipative hadronic corona. Nucl. Phys. A, 769:71–94, 2006.

[55] A. Adare et al. Dielectron production in Au+Au collisions at $\sqrt{s_{NN}}$=200 GeV. Phys. Rev. C, 93(1):014904, 2016.

[56] L. Adamczyk et al. Measurements of Dielectron Production in Au+Au Collisions at $\sqrt{s_{\rm NN}}$ = 200 GeV from the STAR Experiment. Phys. Rev. C, 92(2):024912, 2015.

[57] E. L. Feinberg. Direct Production of Photons and Dileptons in Thermodynamical Models of Multiple Hadron Production. Nuovo Cim. A, 34:391, 1976.

[58] Zebo Tang, Yichun Xu, Lijuan Ruan, Gene van Buren, Fuqiang Wang, and Zhangbu Xu. Spectra and radial flow at RHIC with Tsallis statistics in a Blast-Wave description. Phys. Rev. C, 79:051901, 2009.

[59] A. Adare et al. Detailed measurement of the e^+e^- pair continuum in $p + p$ and Au+Au collisions at $\sqrt{s_{NN}} = 200$ GeV and implications for direct photon production. Phys. Rev. C, 81:034911, 2010.

[60] L. Adamczyk et al. Di-electron spectrum at mid-rapidity in $p + p$ collisions at $\sqrt{s} = 200$ GeV. Phys. Rev. C, 86:024906, 2012.

[61] J. J. Sakurai. Vector-Meson Dominance and Current Algebra in the Parity-Violating Nonleptonic Decays of K Mesons and Hyperons. Phys. Rev., 156:1508–1510, 1967.

[62] M. Dey, V. L. Eletsky, and B. L. Ioffe. Mixing of vector and axial mesons at finite temperature: an Indication towards chiral symmetry restoration. Phys. Lett. B, 252:620–624, 1990.

[63] Nathan P. M. Holt, Paul M. Hohler, and Ralf Rapp. Quantitative Sum Rule Analysis of Low-Temperature Spectral Functions. Phys. Rev. D, 87:076010, 2013.

[64] H. T. Ding, A. Francis, O. Kaczmarek, F. Karsch, E. Laermann, and W. Soeldner. Thermal dilepton rate and electrical conductivity: An analysis of vector current correlation functions in quenched lattice QCD. Phys. Rev. D, 83:034504, 2011.

[65] Joseph I. Kapusta and Edward V. Shuryak. Weinberg type sum rules at zero and finite temperature. Phys. Rev. D, 49:4694–4704, 1994.

[66] H. Gomm, O. Kaymakcalan, and J. Schechter. Anomalous Spin 1 Meson Decays From the Gauged Wess-Zumino Term. Phys. Rev. D, 30:2345, 1984.

[67] Larry D. McLerran and T. Toimela. Photon and Dilepton Emission from the Quark - Gluon Plasma: Some General Considerations. Phys. Rev. D, 31:545, 1985.

[68] H. A. Weldon. Reformulation of finite temperature dilepton production. Phys. Rev. D, 42:2384–2387, 1990.

[69] Joseph I. Kapusta, P. Lichard, and D. Seibert. High-energy photons from quark - gluon plasma versus hot hadronic gas. Phys. Rev. D, 44:2774–2788, 1991. [Erratum: Phys.Rev.D 47, 4171 (1993)].

[70] Jacopo Ghiglieri, Juhee Hong, Aleksi Kurkela, Egang Lu, Guy D. Moore, and Derek Teaney. Next-to-leading order thermal photon production in a weakly coupled quark-gluon plasma. JHEP, 05:010, 2013.

[71] M. Laine. NLO thermal dilepton rate at non-zero momentum. JHEP, 11:120, 2013.

[72] M. Laine. Thermal 2-loop master spectral function at finite momentum. JHEP, 05:083, 2013.

[73] J. Ghiglieri, O. Kaczmarek, M. Laine, and F. Meyer. Lattice constraints on the thermal photon rate. Phys. Rev. D, 94(1):016005, 2016.

[74] G. Jackson and M. Laine. Testing thermal photon and dilepton rates. JHEP, 11:144, 2019.

[75] Marco Cè, Tim Harris, Harvey B. Meyer, Aman Steinberg, and Arianna Toniato. Rate of photon production in the quark-gluon plasma from lattice QCD. Phys. Rev. D, 102(9):091501, 2020.

[76] K. Kajantie, Joseph I. Kapusta, Larry D. McLerran, and A. Mekjian. Dilepton Emission and the QCD Phase Transition in Ultrarelativistic Nuclear Collisions. Phys. Rev. D, 34:2746, 1986.

[77] Leo P. Kadanoff and Paul C. Martin. Hydrodynamic equations and correlation functions. Annals Phys., 24:419–469, 1963.

[78] Stefan Floerchinger, Charlotte Gebhardt, and Klaus Reygers. Electrical conductivity of the quark-gluon plasma from the low energy limit of photon and dilepton spectra. Phys. Lett. B, 837:137647, 2023.

[79] Gert Aarts and Aleksandr Nikolaev. Electrical conductivity of the quark-gluon plasma: perspective from lattice QCD. Eur. Phys. J. A, 57(4):118, 2021.

[80] Peter Brockway Arnold, Guy D. Moore, and Laurence G. Yaffe. Transport coefficients in high temperature gauge theories. 1. Leading log results. JHEP, 11:001, 2000.

[81] Peter Brockway Arnold, Guy D Moore, and Laurence G. Yaffe. Transport coefficients in high temperature gauge theories. 2. Beyond leading log. JHEP, 05:051, 2003.

[82] Letter of intent for ALICE 3: A next-generation heavy-ion experiment at the LHC. 11 2022.

[83] Toru Nishimura, Masakiyo Kitazawa, and Teiji Kunihiro. In preparation.

[84] Toru Nishimura, Masakiyo Kitazawa, and Teiji Kunihiro. Anomalous enhancement of dilepton production as a precursor of color superconductivity. PTEP, 2022(9):093D02, 2022.

[85] Toru Nishimura, Masakiyo Kitazawa, and Teiji Kunihiro. Enhancement of dilepton production rate and electric conductivity around the QCD critical point. PTEP, 2023(5):053D01, 2023.

[86] Alexander L Fetter and John Dirk Walecka. Quantum theory of many-particle systems. Courier Corporation, 2012.

[87] J. I. Kapusta and Charles Gale. Finite-temperature field theory: Principles and applications. Cambridge Monographs on Mathematical Physics. Cambridge University Press, 2011.

[88] Tetsuo Hatsuda and Teiji Kunihiro. QCD phenomenology based on a chiral effective Lagrangian. Phys. Rept., 247:221–367, 1994.

[89] Michael Buballa. NJL model analysis of quark matter at large density. Phys. Rept., 407:205–376, 2005.

[90] Taeko Matsuura, Kei Iida, Tetsuo Hatsuda, and Gordon Baym. Thermal fluctuations of gauge fields and first order phase transitions in color superconductivity. Phys. Rev. D, 69:074012, 2004.

[91] Ioannis Giannakis, De-fu Hou, Hai-cang Ren, and Dirk H. Rischke. Gauge field fluctuations and first-order phase transition in color superconductivity. Phys. Rev. Lett., 93:232301, 2004.

[92] Jorge L. Noronha, Hai-cang Ren, Ioannis Giannakis, Defu Hou, and Dirk H. Rischke. Absence of the London limit for the first-order phase transition to a color superconductor. Phys. Rev. D, 73:094009, 2006.

[93] Gergely Fejős and Naoki Yamamoto. Functional renormalization group approach to color superconducting phase transition. JHEP, 12:069, 2019.

[94] David J Thouless. Perturbation theory in statistical mechanics and the theory of superconductivity. Annals of Physics, 10(4):553–588, 1960.

[95] Takeru Yokota, Teiji Kunihiro, and Kenji Morita. Functional renormalization group analysis of the soft mode at the QCD critical point. PTEP, 2016(7):073D01, 2016.

[96] Takeru Yokota, Teiji Kunihiro, and Kenji Morita. Tachyonic instability of the scalar mode prior to the QCD critical point based on the functional renormalization-group method in the two-flavor case. Phys. Rev. D, 96(7):074028, 2017.

[97] Michel Le Bellac. Thermal Field Theory. Cambridge Monographs on Mathematical Physics. Cambridge University Press, 3 2011.

[98] LG Aslamazov and AI Larkin. Soviet solid state 10, 875 (1968). Phys. Lett. A, 26:238, 1968.

[99] Kazumi Maki. Critical fluctuation of the order parameter in a superconductor. I. Progress of Theoretical Physics, 40(2):193–200, 1968.

[100] Richard S Thompson. Microwave, flux flow, and fluctuation resistance of dirty type-II superconductors. Physical Review B, 1(1):327, 1970.

[101] BI Halperin, TC Lubensky, and Shang-keng Ma. First-order phase transitions in superconductors and smectic-a liquid crystals. Physical Review Letters, 32(6):292, 1974.

[102] Prashanth Jaikumar, Ralf Rapp, and Ismail Zahed. Photon and dilepton emission rates from high density quark matter. Phys. Rev. C, 65:055205, 2002.

[103] Toru Nishimura, Yasushi Nara, and Jan Steinheimer. Enhanced Dilepton production near the color superconducting phase and the QCD critical point. 11 2023.

[104] Tetyana Galatyuk. Future facilities for high μ_B physics. Nucl. Phys. A, 982:163–169, 2019.

[105] R. Rapp, J. Wambach, and H. van Hees. The Chiral Restoration Transition of QCD and Low Mass Dileptons. Landolt-Bornstein, 23:134, 2010.

[106] Eric Braaten, Robert D. Pisarski, and Tzu-Chiang Yuan. Production of Soft Dileptons in the Quark - Gluon Plasma. Phys. Rev. Lett., 64:2242, 1990.

[107] Jacopo Ghiglieri and Guy D. Moore. Low Mass Thermal Dilepton Production at NLO in a Weakly Coupled Quark-Gluon Plasma. JHEP, 12:029, 2014.

[108] Yasushi Nara and Akira Ohnishi. JAM mean-field update: mean-field effects on collective flow in high-energy heavy-ion collisions at $\sqrt{s_{NN}} = 2 - 20$ GeV energies. 9 2021.

[109] J. D. Bjorken. Highly Relativistic Nucleus-Nucleus Collisions: The Central Rapidity Region. Phys. Rev. D, 27:140–151, 1983.

[110] Anton Motornenko, Jan Steinheimer, Volodymyr Vovchenko, Stefan Schramm, and Horst Stoecker. Equation of state for hot QCD and compact stars from a mean field approach. Phys. Rev. C, 101(3):034904, 2020.

[111] Christoph Herold, Apiwit Kittiratpattana, Chinorat Kobdaj, Ayut Limphirat, Yupeng Yan, Marlene Nahrgang, Jan Steinheimer, and Marcus Bleicher. Entropy production and reheating at the chiral phase transition. Phys. Lett. B, 790:557–562, 2019.

[112] Thiranat Bumnedpan, Jan Steinheimer, Marcus Bleicher, Ayut Limphirat, and Christoph Herold. Enhanced pion-to-proton ratio at the onset of the QCD phase transition. Phys. Lett. B, 835:137537, 2022.